Local Structure of Nanocrystalline, Nanoporous, and Heterogeneous Functional Materials: Advancing Tools for Extracting Order From Disorder

Songsheng Tao

Submitted in partial fulfillment of the
requirements for the degree of
Doctor of Philosophy
under the Executive Committee
of the Graduate School of Arts and Sciences

COLUMBIA UNIVERSITY

2023

© 2023

Songsheng Tao

All Rights Reserved

Abstract

Local Structure of Nanocrystalline, Nanoporous, and Heterogeneous Functional Materials: Advancing Tools for Extracting Order From Disorder

Songsheng Tao

Nanocrystalline, nanoporous, and heterogeneous functional materials have a range of unique physical and chemical properties at the nanoscale that make them useful in various fields such as gas storage, sensing, catalysis, and construction. However, these materials have complex and varied internal structures make them difficult to analyze using traditional methods. In this work, advanced tools were presented that combine several existing algorithms and techniques to enable efficient and accurate analysis of the structures of these materials. The tools were tested on well-studied systems (TiO_2 nanoparticles) and novel materials (multiple metal organic frameworks), and the results showed that they produced accurate and reliable results. These results have contributed to important scientific discoveries, some of which are highlighted in this thesis.

First, an automated platform for x-ray scattering experiments and a streaming data pipeline were developed to determine pair distribution functions, which were used to study nanocrystalline, nanoporous, and heterogeneous functional materials. A systematic workflow was then proposed and tested to analyze the phases and morphologies of metal oxide nanoparticles. Using the data pipeline and workflow, the effects of temperature on phases, morphologies, and structure order during the synthesis of titanium oxide (bronze) nanoparticles were demonstrated.

Specific tools were then designed to analyze the structures of nanoporous materials based on the disorder in their complex structures. The turbostratic disorder in zirconium phosphates was analyzed, and the potential to tune disorders using phosphoric acid concentration was demonstrated. In addition, the glass transition in metal-organic frameworks was detected, and a reminiscent correlation between metal sites in the glass state was discovered. Furthermore, evidence of polar solvent-induced lattice arrangement in an aluminum metal-organic framework was found using the analysis of pair distribution functions. Finally, a simple but effective algorithm was proposed to study the grain distribution and mosaicity in heterogeneous crystalline materials, moving beyond the study of homogeneous systems.

Overall, these studies aim to enable faster and more comprehensive analysis of the disordered structures in nanocrystalline, nanoporous, and heterogeneous materials, which could have applications in fields including photocatalysis, optical or gas sensing, radioactive waste storage, and metallurgical industry.

Table of Contents

Acknowledgments viii

Dedication x

Chapter 1: Challenges in solving the local structure 1

1.1 Challenges in solutions of nanostructures 1

1.2 Autonomous experiments and streaming data reduction 1

1.3 Quantitative analysis of the morphology and structure of metallic oxide nanoparticles 2

1.4 Quantitative analysis of the nanoporous materials 7

1.5 High-throughput *in situ* studies of the highly structurally heterogeneous samples . . 10

1.6 Infrastructure for structure analysis 15

Chapter 2: X-ray scattering and pair distribution function 16

2.1 Total x-ray scattering method 16

2.1.1 X-ray powder diffraction experiment 16

2.1.2 Momentum transfer 17

2.2 Scattering intensity of total scattering 18

2.2.1 Scattering of a single atom 18

2.2.2 Scattering of an atom assemble 19

2.2.3 Scattering of atom assemble 20

2.2.4 Scattering of isotropic atom assembles 20

2.3 X-ray scattering of crystals 21

2.3.1 Perfect crystals 21

2.3.2 Imperfect crystals 22

2.3.3 Mosaicity 22

2.4 Pair distribution function (PDF) 23

2.4.1 Introduction 23

2.4.2 Structure function 24

2.4.3 PDF as Fourier transformation 25

2.4.4 PDF as atomic distance histogram 26

2.4.5 Characteristic functions 27

2.4.6 Model PDF 29

2.4.7 Evaluate models 29

Chapter 3: Autonomous experiments and streaming data reduction 30

3.1 Introduction 30

3.2 Method 31

3.3 Result 33

3.4 Conclusion 38

Chapter 4: Quantitative analysis of the morphology and structure of metallic oxide nanoparticles 40

4.1 Introduction 40

4.2 Experiments and methods 41

4.3 Modeling workflow 44

4.4 Results 45

4.4.1 Approach to obtaining a good ACM fit to these nanoparticle samples 45

4.4.2 Refining all samples with the same protocol 58

4.5 Conclusions 63

Chapter 5: Quantitative analysis of the nanoporous materials 64

5.1 Zirconium phosphate: the pathway from turbostratic disorder to crystallinity 64

5.1.1 Introduction 65

5.1.2 Method 66

5.1.3 Result 69

5.1.4 Conclusion 78

5.2 Designing glass and crystalline phases of metal-bis(acetamide) s to promote high optical contrast 79

5.2.1 Introduction 79

5.2.2 Method 80

5.2.3 Result 81

5.2.4 Conclusion 91

5.3 Rapid desolvation-triggered domino lattice rearrangement in a metal-organic framework 91

5.3.1 Introduction 91

5.3.2 Method 93

5.3.3 Result 94

5.3.4 Conclusion 94

Chapter 6: High-throughput *in situ* studies of the highly structurally heterogeneous samples 98

6.1 Introduction 98

6.2 Method and Design 99

6.2.1 Algorithm 99

6.2.2 Python Package 101

6.3 Example: Study Optical Float Zone Furnace Crystal Growth 102

6.3.1 Spatially Resolved Experiment 102

6.3.2 Discovery: Missing Parts of the Grains 105

6.4 Conclusion 110

Conclusion or Epilogue 111

References 113

List of Figures

1.1 Receptor and transducer function of a semiconductor gas sensor 3
1.2 A simplified model demonstrating band bending in a semiconductor with a broad-band gap following the chemisorption of charged species 4
1.3 Intergranular contact regions in determining the conductance over a polycrystalline metal oxide semiconductor 5
1.4 Effect of SnO_2 particle diameter D on sensor response (R gas/R_{air}) 6
1.5 Ideal structures of zirconium phenyl phosphonate and zirconium biphenyl bisphosphonate 8
1.6 Approaches for achieving CP or MOF glasses 9
1.7 Schematic of FZ synthesis 13
1.8 Schematic of a type of OFZF device 14

2.1 An example of total x-ray scattering experiment results 17
2.2 Illustration of elastic x-ray scattering from a randomly oriented, isotropic sample of rutile and anatase TiO_2 nanocrystals 18
2.3 The path from scattering intensity data to pair distribution function for nickel . . . 25
2.4 Different characteristic form and distribution functions for anatase nanoparticles . . 28

3.1 Brief flowchart of the XPDACQ and PDFSTREAM 31
3.2 Temperature series of $Co(C_{12}O_2N_2H_{22})_3[CoCl_4]$ metal-organic framework 35
3.3 Time series of boehmite-nitric-acid mixture 36
3.4 High-throughput PDF measurement 39

4.1 Measured PDFs from the TiO_2 samples synthesized at three different temperatures . 43
4.2 Calculated and measured PDFs of TiO_2 47
4.3 The changes in R_w after adding a second phase to the model 49
4.4 Data PDFs and PDFs from best fit models plotted over the range $35 \leq r \leq 50$ Å . . 51
4.5 PDFs in the high-r region from the best fit models to the T190L measured data and different contributions 59
4.6 PDFs of the best fit models to the measured data for each sample 60
4.7 Best fit parameters for samples synthesized at different temperatures 61

5.1 Schematic of the α-ZrP structure 69
5.2 Experimental PDFs of the S-series samples 70
5.3 Proportion of the crystalline component, P_c versus the concentration of H_3PO_4 . . . 72
5.4 Representative fits of the attenuated α-ZrP model 73

5.5 Representative fits of the single-layer model to ZP14S and ZP1S 74
5.6 Experimental and fitted PDFs of the S-series samples with residual curves 76
5.7 Refined crystallite size as a function of the H_3PO_4 concentration in the synthesis of stirring and reflux methods 77
5.8 Refined crystallite size as a function of the H_3PO_4 concentration at an annealing temperature series 78
5.9 PDF of the room-temperature (RT) glassy state and high-temperature (HT) crystalline state for three systems 82
5.10 Glass transition of $Mn(eba)_3[ZnCl_4]$, $Mn(eba)_3[MnCl_4]$, and 1-Mn/Co(Zn) 83
5.11 PDF comparisons of the high-temperature solid and room-temperature glass phases of $Mn(eba)_3[MnCl_4]$, $Mn(eba)_3[ZnCl_4]$, and 1-Mn/Co(Zn) 84
5.12 Partial PDF analyses for crystalline and glassy $Mn(eba)_3[MnCl_4]$, $Mn(eba)_3[ZnCl_4]$, and 1-Mn/Co(Zn) 86
5.13 Comparison between $I(Q)$ and $G(r)$ of $Mn(eba)_3[MnCl_4]$, $Mn(eba)_3[ZnCl_4]$, 1-Mn/Co(Zn) 87
5.14 Variable-temperature FSDP fitting results of $Mn(eba)_3[MnCl_4]$ 88
5.15 Variable-temperature FSDP fitting results of 1-Mn/Co(Zn) 89
5.16 Crystal structure of $Mn(eba)_3[MnCl_4]$ at 298 K and 100 K 90
5.17 Lattice rearrangement in an Al-MOF 92
5.18 PDFs for AlTz-53-DMF, AlTz-53-DEF, and AlTz-68 95
5.19 Comparison of experimental PDF for AlTz-53-DEF with that simulated using an average AlTz-53 crystal model 96
5.20 Proposed disordered structural model of AlTz-53-DEF 97

6.1 The visualization of the immediate results in the algorithm: (a) the pixel-wise maximum (abbreviated as "maximum image"); (b) the pixel-wise minimum (abbreviated as "minimum image"); (c) The difference between maximum image and minimum image (abbreviated as "subtracted image"). 100
6.2 Schematic of the experimental setup. The sample is moved in x and y directions. It can also be rotated along the axis of the rod (the laboratory y-axis). The stacked diffraction images represent a time series of measurements at different (x, y) positions and/or rotation angles. 103
6.3 The crystal maps of the TiO_2 rod generated by the CRYSTALMAPPING package. Each panel is the visualization of the distribution of the intensity of a Bragg peak from a region in the sample on the XY plane in Figure 6.2. The yellowish color means higher intensity. These maps show how different grains distribute in the rod on the XY plane. 106
6.4 Rocking curves from a point (62 mm, 15 mm) on the large grain shown in peak 38 in Figure 6.3, automatically generated by the `rocking_curve` mode of the `cm.visualize()` method in the CRYSTALMAPPING package. Each panel depicts the intensity of a Bragg peak as a function of the rotation angle, ϕ, about the z-axis (shown schematically in Figure 6.2). 109

List of Tables

4.1 Sample synthesis information 41
4.2 Structure mining results 45
4.3 The first 20 results from STRUCTUREMINING to the residuals from the single phase fitting 48
4.4 Best fit values for parameters from the PDF refinements 53
4.5 Comparison between the models with and without ligands 55

5.1 Summary of the transitions in nanoporous materials 64
5.2 Resume of α-ZrP Samples 67

Acknowledgements

I am deeply grateful to a number of people who have supported and encouraged me throughout my PhD journey.

First and foremost, I would like to express my sincere gratitude to my advisor, Dr. Simon J.L. Billinge, for his unwavering support, guidance, and encouragement. His expertise and insights have been invaluable in shaping my research and helping me grow as a scholar. I am also grateful for his patience and understanding during the times when I struggled, and for his encouragement to keep going. I would not have been able to complete his work without his support and guidance.

I would also like to thank the members of my thesis committee, Dr. Irving P. Herman, Dr. Nanfang Yu, Dr. Yuan Yang, and Dr. Jarad Mason, for their valuable feedback and constructive criticism. Their support and guidance have been invaluable in completing this work, and I am grateful for the time and effort they put into reviewing my research.

I am grateful to my colleagues and friends in the Billinge group at Columbia University and 28-ID beamlines at National Synchrotron Light Source II for their camaraderie and support. In particular, I would like to thank Dr. Soham Banerjee, Chia-hao (Timothy) Liu, Dr. Christopher J. "CJ" Wright, Dr. Long Yang, Dr. Yevgeny Rakita, Dr. Sandra H. Skjaervoe, Dr. Maksim Rakitin, Dr. Thomas Caswell, Dr. Daniel Olds, Dr. Eric Dooryhee, Dr. Milinda Abeykoon, Dr. Sanjit Ghose, Dr. Hui Zhong, Dr. Jianming Bai for their help and assistance with various aspects of my research, as well as for their friendship and support throughout my PhD journey.

I would also like to extend my appreciation to the Columbia University, Brookhaven National Laboratory, and United States Department of Energy for providing me with the resources and support needed to complete this research. I am grateful for the opportunities and support they have provided me, and for their commitment to advancing knowledge and research.

I would also like to thank my family and loved ones for their love and support throughout this journey. Their unwavering belief in me and encouragement have kept me going through the highs and lows of my PhD. I am especially grateful to my parents for their constant support and for always believing in me.

Finally, I would like to thank all of the participants in my research for their time and willingness to share their experiences and insights with me. Their contributions have been invaluable to this work.

Dedication

To my loved ones, whose unwavering support and encouragement have made this journey possible.

Chapter 1: Challenges in solving the local structure

1.1 Challenges in solutions of nanostructures

Since the first discovery of crystal x-ray scattering in 1912 [1], history has witnessed its usage in revealing the structures of numerous materials. With today's synchrotron technique, researchers can obtain data with incredible resolution in a short amount of time [2]. The exponential growth of computational power enables researchers to model increasingly complex models [3]. As the capacity grows, it becomes increasingly important to develop the computational infrastructure for the x-ray scattering experiments and the structure solution beyond the crystallography [4].

In the following Chapters 3, 4, 5, and 6, I will demonstrate my methodology development to solve the nonconventional problems in x-ray scattering. For each one, I will show how I used it to answer important scientific questions, providing insights for understanding the structures at the nano-scale.

1.2 Autonomous experiments and streaming data reduction

In today's synchrotron x-ray scattering experiments, autonomous experiments and streaming data reduction are crucial [5, 6, 7, 8].

Users may have a large batch of samples and limited beamtime to collect data. In this case, they require a method to run an automated workflow to save time operating the devices [9, 10]. In another case, users may want to see the XRD or PDF pattern in an interactive view on-site before deciding on the following measurement step [11]. At NSLS-II, Ophyd and Bluesky construct the framework for these features [12]. However, there is still a significant gap between what it provides

and what users require for powder x-ray diffraction (PXRD) and pair distribution function (PDF) measurements.

Users wish to acquire x-ray scattering data without knowing anything about code, such as python generators, or technical aspects, such as shutter control. Meanwhile, they wish to see XRD and PDF data on the screen and on their hard disk without launching any data processing program [13]. However, considering the bluesky and ophyd, it is a challenging task. As a result, I created the XpdAcq software package, which is based on bluesky and ophyd, to solve the issues in x-ray studies, particularly at beamline 28-ID.

I demonstrated its features and delivered several usage samples in Chapter 3.

1.3 Quantitative analysis of the morphology and structure of metallic oxide nanoparticles

Metallic oxide nanoparticles have many critical technological applications. For example, they are intensively used in electronic devices as gas sensors, solar cells, and antennas [14, 15]. Knowing their crystallography phase and morphology is crucial because they significantly affect the selectivity and the activity of catalysis [15, 16]. An example of SnO_2 sensor is shown in the following paragraphs, described in [15], to demonstrate the importance of knowing the crystallography phase and morphology of metal oxide particles.

Used as gas sensors, the metal oxide nanoparticles have two functionalities: receptor and transductor (Figure 1.1) [14]. As a receptor, they interact with the gas molecules [14]. As a transductor, they convert the information of the molecules into a measurable signal, e. g., electric resistance. In both processes, the nanostructure and morphologies of the particles play a significant role. It is because of the underlying physics behind it [14].

A typical physic used for gas sensing using metal oxides is the shift of the equilibrium state of the oxygen reaction. For instance, reducing gas increases the conductivity for n-type semiconductors and decreases that for p-type semiconductors [17, 17]. Researchers have discussed the causes of the change in detail for the exemplary SnO_2 sensor [17].

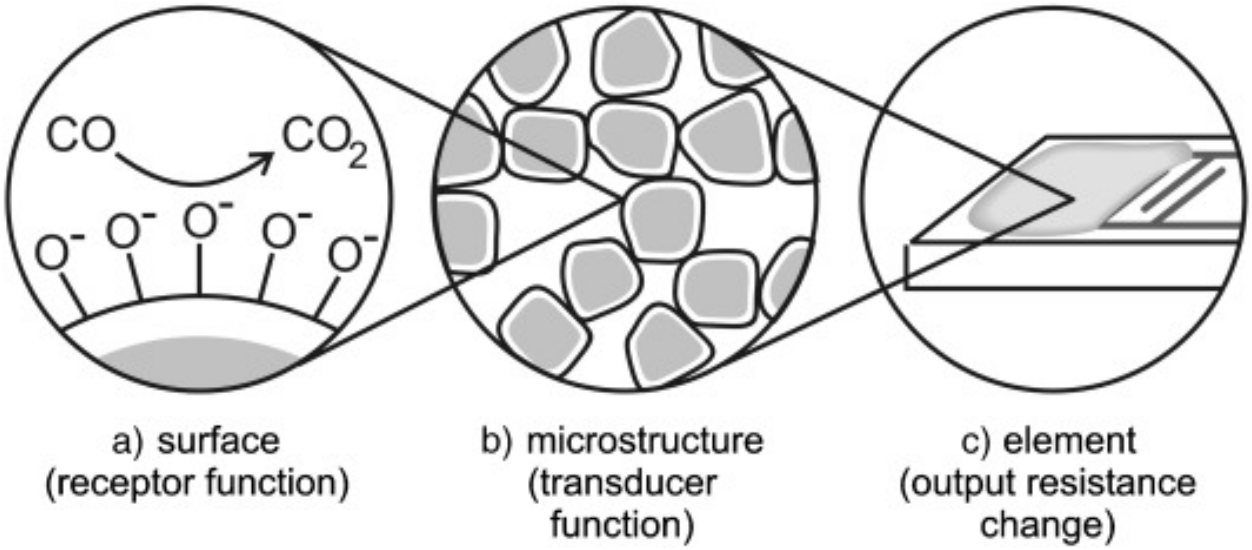

Figure 1.1: Receptor and transducer function of a semiconductor gas sensor. Receptor and transducer function of a semiconductor gas sensor: a) surface, providing the receptor function, b) microstructure of the sensing layer, providing the transducer function, c) element, enabling the detection of the change in output resistance of the sensing layer, here deposited on an interdigital microelectrode. (Reprinted (adapted) with permission from [15]. Copyright 2006 John Wiley & Sons, Inc)

The SnO_2 surfaces absorb the oxygen molecules. These molecules accept an electron from the SnO_2 because of their lower energy level than the Fermi level of SnO_2. The effect's strength depends on the oxygen concentration, while the chemical equilibrium of the absorption determines the concentration. Below 420 K, the oxygen on the surface is mostly O^{2-}, but if the temperature rises to be in the range from 420 K to 670 K, it is dominated by O^{-}. Above 670 K, the O^{2-} ions form in parallel. When it goes above 870 K, oxygen is incorporated into the lattice [15]. Thus, the working range of the sensor is from 420 K to 670 K. In the operating range, the intrinsic oxygen vacancies donate the electrons from the conduction band, which are trapped on the surface [18]. This phenomenon results in an electron-depleted region near the surface. Its maximum coverage can reach from 10^{-3} cm to 10^{-3} cm [19].

The presence of negative surface charges causes the band to bend (Figure 1.2), resulting in a surface barrier to electric current of 0.5 – 1.0 eV. The height (eV surface) and depth (Λ_{air}) of the band-bend depend on the surface charge determined by the amount and type of adsorbed

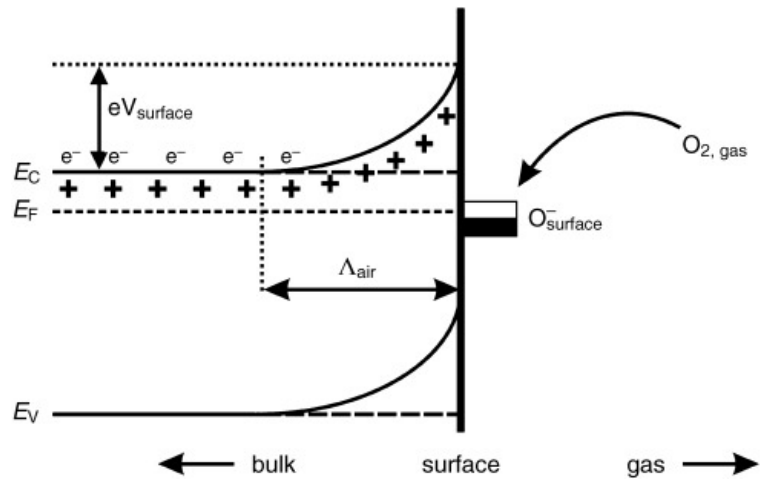

Figure 1.2: A simplified model demonstrating band bending in a semiconductor with a broadband gap following the chemisorption of charged species (in this case, the ion-sorption of oxygen). Conduction band, valence band, and Fermi level energies are denoted by the letters EC, EV, and EF, respectively. Lambda air, on the other hand, refers to the potential barrier's surface and the thickness of the space-charge layer. $e-$ stands for the conducting electrons, while + stands for the donor sites. (Reprinted (adapted) with permission from [15]. Copyright 2006 John Wiley & Sons, Inc)

oxygen [17]. At the same time, Λ_{air} depends on the Debye length (Eq. 1.1), a characteristic of semiconductor materials for a given donor concentration [20],

$$L_{\mathrm{D}} = \sqrt{\frac{\varepsilon_0 \varepsilon k_{\mathrm{B}} T}{e^2 n_{\mathrm{d}}}} \tag{1.1}$$

where k_B is the Boltzmann constant, ϵ is the permittivity, O is the permittivity of free space, T is the operating temperature, e is the electron charge, and n is the carrier concentration corresponding to the donor concentration.

Electronic conductivity occurs via percolation channels in polycrystalline sensing materials via grain-to-grain contacts. As a result, it depends on the eV surface of the nearby grains. The eV surface represents the Schottky barrier. In this instance, the conductance G of the sensing material can be expressed as Eq. 1.2 [21].

$$G \approx \exp\left(\frac{-\mathrm{eV}_{\mathrm{surface}}}{k_{\mathrm{B}} T}\right) \tag{1.2}$$

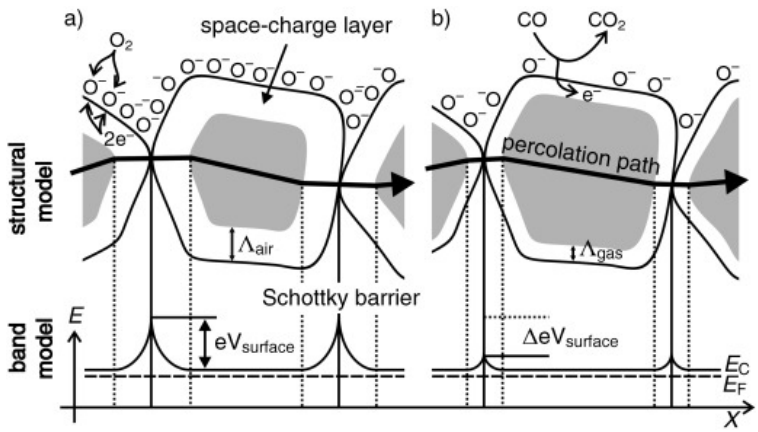

Figure 1.3: Intergranular contact regions play an important role in determining the conductance over a polycrystalline metal oxide semiconductor. It is demonstrated in a structural and band model by showing the effect of CO gas on eV surface and Λ_{air} for large grains. (Reprinted (adapted) with permission from [15]. Copyright 2006 John Wiley & Sons, Inc)

The large surface-to-bulk ratio of nanoparticulate metal oxides is, in theory, expected to result in a higher sensitivity, as well as a quicker response and recovery time, compared to microcrystalline materials, since the gas-sensor response depends on the surface reaction between the metal oxide and the gas molecules in the ambient. If the radius is within the range of the space-charge layer, the model (Figure 1.3) predicts that reducing the particle diameter would result in convergent Schottky barriers. It implies that the depletion zones begin to overlap as the radius gets smaller until it is smaller than Λ_{air}. As a result, surface states dominate in determining electrical characteristics [22, 23].

Much research has been conducted to examine this effect since it is anticipated that the particle size would significantly impact sensor performance. Early in the 1990s, Yamazoe and colleagues presented systematic investigations to address whether nanocrystalline metal oxides increase sensitivity [24, 25, 26]. More specifically, they addressed what happens when D falls to a level comparable to Λ_{air} and proceeded to develop a model that adequately captures this dependence. They discovered a significant relationship between grain diameter D and sensitivity for porous sintered SnO_2 elements (made with pure SnO_2, foreign-oxide-stabilized SnO_2, or impurity-doped SnO_2) in a size range of 5 nm to 32 nm [17]. In particular, for the small D region in the range of Λair, the sensitivity of pure and stabilized elements for H_2, CO, and $i{-}C_4H_{10}$ increases steeply

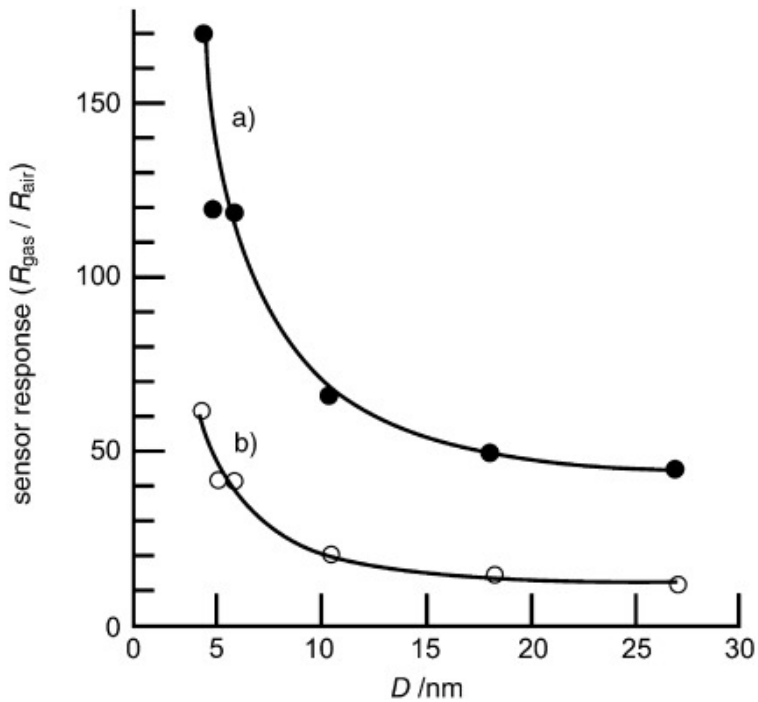

Figure 1.4: Effect of SnO_2 particle diameter D on sensor response (R gas/R_{air}): a) 800 ppm H2; b) 800 ppm CO in the air at 573 K. (Reprinted (adapted) with permission from [15]. Copyright 2006 John Wiley & Sons, Inc)

as D decreases. The sensitivity (measured for 800 ppm CO or 800 ppm H_2 at 573 K) dramatically increased for particle sizes below 10 nm (Figure 1.4).

Thus, researchers have studied the nanostructure and the morphology of metal oxide nanoparticles intensively. One frequently used technique is the x-ray pair distribution function (PDF) [3]. They collect the x-ray diffraction images of the nanoparticles using the synchrotron x-ray scattering and model the PDF starting from a guess of the phase and morphology [27].

The attenuated crystal model (ACM) is one of the standard methods. Although used for multiple structure solutions, there still needs to be a modeling workflow to achieve an optimal solution. Chemists and material scientists still needed help finding the correct initial guess and achieving the optimal model for their data. It is challenging with the metal oxide nanoparticles, which have many possible phases on the phase diagram.

Here, I proposed a universal workflow to explore the structure and morphology of metal

oxide nanoparticles. It is a greedy algorithm to explore the solution space with every step as optimal. I demonstrated its efficiency and effectiveness using TiO_2 nanoparticles as an example in Chapter 4.

1.4 Quantitative analysis of the nanoporous materials

Besides the nanoparticles, nanoporous materials are another essential category where the surface becomes impactful [28, 29]. As discussed in [30], metal-organic frameworks (MOFs) stand out among the classes of very porous materials for their structural diversity, tuneability, and various chemical and physical characteristics. MOFs are extended crystalline structures whereby metal cations or clusters of cations ("nodes") are joined by multitopic organic "strut" or "linker" ions or molecules. Almost unlimited combinations are conceivable because of the range of metal ions, organic linkers, and structural motifs [31]. Additionally, the potential for post-synthetic alteration gives the synthetic variability a new dimension [32]. The idea of routinely predesigning frameworks to provide desired qualities is suggested by the capacity to computationally forecast, with excellent accuracy, affinities of guests for host frameworks in combination with the expanding library of empirically established structures. Due to their significant internal surface areas, vast porosity, and high degree of crystallinity, MOFs are frequently likened to zeolites [33, 34]. Accordingly, zeolites and MOFs have both been used for a variety of similar tasks, such as heterogeneous catalysis [28], gas separation [35], and storage [36, 37].

Although there is some disagreement about the precise definition of a MOF, it is generally accepted that they are crystalline, porous hybrid organic-inorganic compounds. However, there is a different class of porous, hybrid materials that, except for crystallinity, display the general properties of a MOF. These substances fall under UMOFs, or unconventional MOFS, which are weakly crystalline but extremely porous solids comprising organic and inorganic components [38]. Due to the low solubility of phosphonate metal complexes, which causes fast precipitation and ill-ordered structures, especially for tri- and tetravalent metals, many phosphonate-based materials fall into this category.

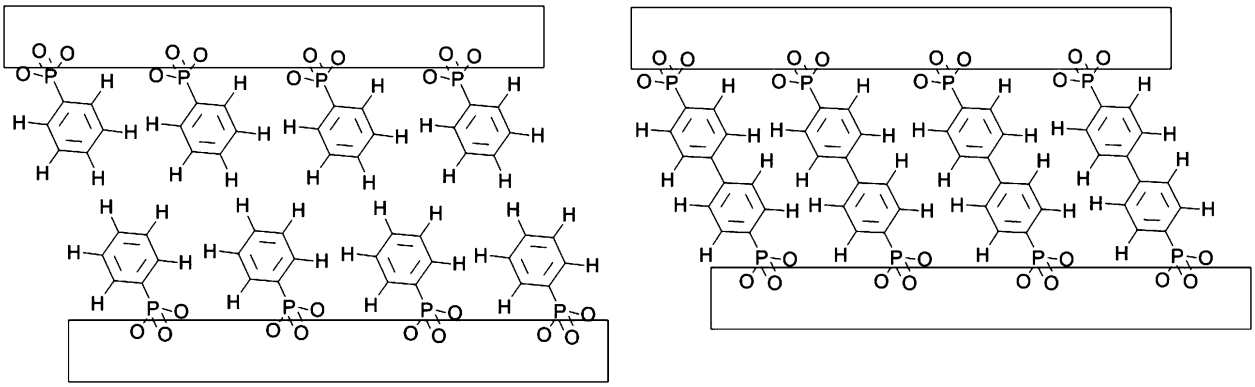

Figure 1.5: Ideal structures of zirconium phenyl phosphonate and zirconium biphenyl bisphosphonate are depicted in an illustration. Reprinted (adapted) with permission from [30]. Copyright 2012 American Chemical Society.

A group of Zr compounds based on biphenylbis(phosphonic acid), and methyl phosphonic acid (Figure 1.5) described by Dines et al [39]. may have been the first instances of UMOFs to be published. He claimed that porosity would result from the methyl groups alternating with the pillar biphenyl group in the gap between the layers. The materials had pores and showed a wide variety of hole sizes. As more methyl phosphonic acid was applied, the porosity increased. However, Clearfield found that even the molecule devoid of methyl phosphonate groups was virtually as porous as the ligand compounds with the most excellent porosity [38].

Phosphonate-based UMOFs have strong thermal stability and excellent air and water resistance. It preserves their porosity while enabling usage or post-synthetic functionalization under circumstances that would degrade other materials. Traditional phosphonate-based MOFs have had their potential uses thoroughly studied, but UMOF applications have yet to, even though they exhibit similar promise and remarkable versatility. More than 90,000 crystalline CPs/MOFs with a variety of structural motifs and uses have been described [40]. The evolution of the crystalline state has dominated the chemistry of CPs/MOFs thus far [41, 42]. Because they are difficult to describe and have unrealized usefulness, the ensuing x-ray-amorphous compounds, whether from synthesis or external stimuli, are frequently disregarded.

Recently, a new class of thoroughly described CPs and MOFs has emerged that combines

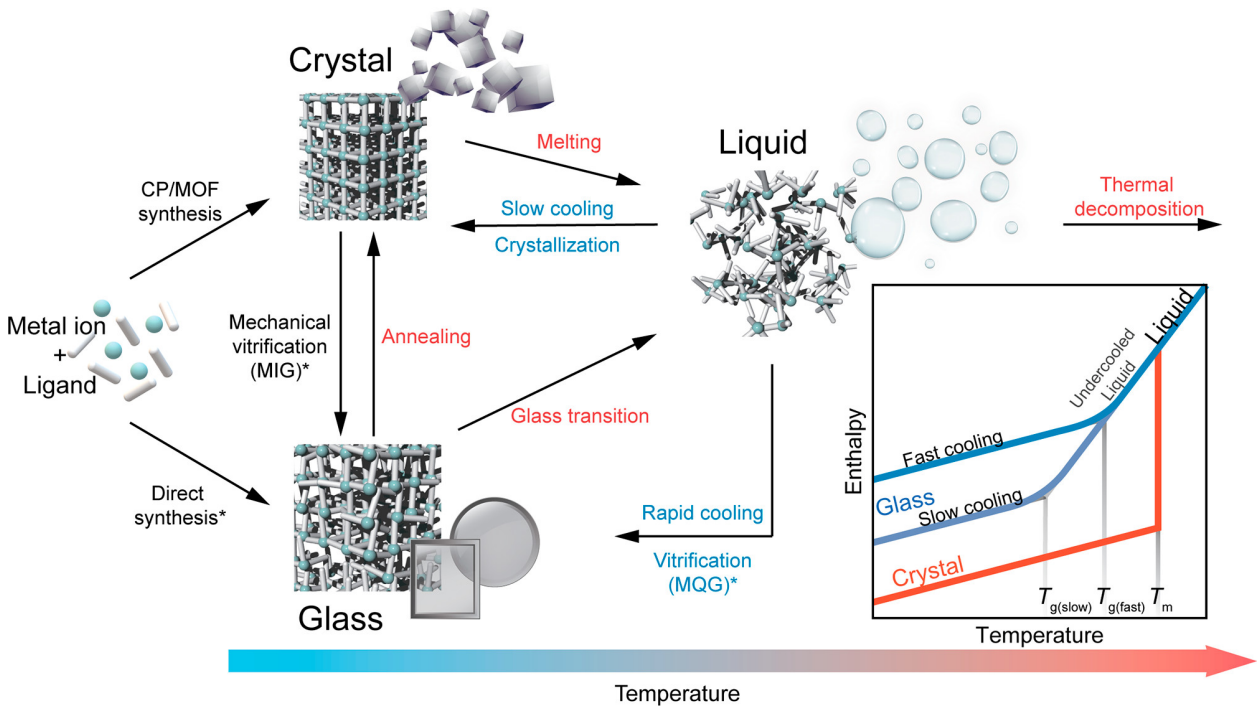

Figure 1.6: Approaches for achieving CP or MOF glasses. Three common routes, including melt-quenching (MQG), mechanical vitrification (MIG), and direct synthesis, for achieving CP/MOF glasses are highlighted with an asterisk. The inset shows enthalpy as a function of temperature for a liquid at various cooling rates at constant pressure. Cooling a liquid at a higher rate provides a continuous glass transition. Enthalpy and Tg are dependent on the cooling rate. A discontinuous first-order crystallization process occurs at lower cooling rates. Tg and Tm represent glass transition and melting temperature, respectively. (Reprinted (adapted) with permission from [40]. Copyright 2022 American Chemical Society.)

characteristics of the liquid and solid phases (Figure 1.6) [43, 44]. The structural variety and characteristics of CPs/MOFs can be extended in a way that is impossible with traditional inorganic, organic, and metallic glasses, thanks to the concepts of reticular design and coordination chemistry [41]. Opportunities have been found for the characteristic behavior of very dense and processable glass phases, despite the crystal's porous structure scarification during the phase transition.

The creation of composite hybrids, perfect solid-electrolytes [45, 46, 47], materials with distinct optical properties [48, 49, 50], and homogenous membranes for gas separation is made possible by the moldability and grain-boundary-free character of these materials. [51, 52, 53] However, only a few CPs/MOFs have demonstrated a glass transition or a stable liquid state upon amor-

phization. Additionally, we can classify the class as network-forming liquids since melts contain metal-ligand coordination. Their strongly directed intermolecular attraction, which corresponds to the coordination bonds between molecules, sets them apart from normal molecular fluids [54]. The behavior resembles the directionally organized network of hydrogen bonds in water or the Si−O and Zn−Cl interactions between the structural elements of SiO_2 and $ZnCl_2$ [55]. As a result, the chemical variety of CPs and MOFs provides chances to modify characteristics by altering network topologies and longer-range ordering in liquid states [56].

However, it is hard to solve their structure because of the disorder [57]. Specific methods need to be used to solve the specific problems. I demonstrate how I solved some impactful problems for nanoporous materials in Chapter 5 using the PDF. They include:

- The pathway from turbostratic disorder to crystallinity in zirconium phosphates;
- Designing glass and crystalline phases of metal-bis(acetamide) s to promote high optical contrast;
- Rapid desolvation-triggered domino lattice rearrangement in a metal-organic framework.

These questions have a shared feature. The order's persistence and loss are crucial for their properties and applications. Thus, PDF analysis of their order is crucial to understanding their properties.

1.5 High-throughput *in situ* studies of the highly structurally heterogeneous samples

Many components in today's electronics are structurally heterogeneous. They are either different orientated grains, chemical compositions, phases, or various levels in order [58, 59, 60]. The spatial distribution of these properties is crucial for their functionalities.

One example is the single crystal superalloy. Nickel-based single-crystal superalloys (Ni-SXs) are widely used in contemporary aero-engines and commercial gas turbines because of their excellent creep behavior. Ni-SX derives the creep strength from an inherent two-phase microstruc-

ture (γ phase and γ' phase), which is favorable to the creep strength but disadvantageous to the extension of creep fractures. The compositions of alloys control the main microstructural characteristics, such as the volume percentage of the γ' phase and the lattice misfit, as well as the formation and dispersion of the precipitated phase. These microstructural characteristics and the precipitated phase significantly impact the creep qualities [61].

Thus, it is essential to know the domain distribution in crystal growth. How to reveal it may depend on the growth method. Among various methods developed for single crystal growth, I will briefly describe the representative ones, including Verneuil, Czochralski, Flux, Bridgman, and Float Zone.

The Verneuil process, created to create synthetic rubies and sapphires from a powdered Al2O3 feed, is the earliest technique for creating single crystals. In this technique, pure oxygen blows the feed material through a tube. Another tube filled with pure hydrogen is located outside of this one. These tubes' openings ignite the two gases, melting the Al_2O_3 into minute droplets. As the droplets hit a rod, they crystallize. The rod descends to let fresh droplets fall on the crystal and increase its mass as other droplets fall, forming a larger crystal as they do. The gemstone is then obtained by breaking off the rod or boule [62].

The Czochralski (CZ) process, one of the most used ones, is used to create the Si boules later sliced into wafers for computer chips. This process involves melting raw material in a crucible, lowering a tiny seed crystal into the melt, pulling it out, and growing a crystal behind it. The crucible, which is frequently constructed of a suitable oxide like SiO_2 or an inert metal like Pt or Ir, might cause side reactions and impurities. Therefore caution should be exercised while using this method. Boules created with this method may reach 190 mm in diameter for $Gd_3Ga_5O_{12}$ [63].

The precursors are dissolved in a suitable solvent termed the "flux" during flux growth. Once the material has been dissolved, the temperature is reduced, or the flux evaporates, resulting in a supersaturated solution that nucleates crystals. This process is comparable to how rock candy is formed from sugar-saturated water. Because the temperature utilized to create the crystals is

lower than if the flux was not employed, this procedure may result in lower defect density crystals. However, this approach frequently results in tiny crystals [63, 64].

Bridgman growth is a method where the precursors are put into a crucible, which involves melting the precursors in a high-temperature furnace. The system crystallizes due to further lowering the crucible into a cooler area after it has melted. The temperature differences between the two furnaces and the decreasing pace can affect the crystallization gradient. This approach benefits from a sealed system, which eliminates mass transfer out of the system, such as precursor evaporation. Like flux growth, the crucible in this method might react with the melt, resulting in crystal imperfections. The single crystal alloys for jet turbines are created using a technique akin to the Bridgman [65].

In 1952, the FZ process (Figure 1.7) was used as a purification method on silicon for use in the semiconductor industry [66, 67, 68]. Impurities preferentially flow into the melt during the FZ process, leaving behind purer material. It is comparable to the freezing out of pure ice during the freeze-distillation process used to make ice wine, where the sugars in the grapes behave as impurities in silicon and are preferentially left in the liquid. Contrary to ice wine, the desirable substance in the case of silicon is silicon, which has been purified. As fewer oxygen impurities were present in the crystal, this procedure produced crystals of superior quality than the CZ process, which was previously in use. High-performance solar panels employ silicon crystals with outstanding carrier lifetimes as a result. [69] With the synthesis of ferrite crystals, FZ began producing oxide materials in 1969 [70]. Since then, FZ synthesis of oxide materials has expanded to be used for various materials. As of 2015, over 100 were mentioned in [71] with applications to superconductors [72, 73, 74, 75] , magnetic frustration [76, 77] , optical electronics [66, 78, 79] , and superalloys [71].

In Float Zone (FZ) growth, a molten floating zone is created by joining two rods (a seed and a feed rod) that have been melted at the tip (Figure 1.8). A crystal is formed on top of the seed rod by moving this zone up the feed rod. Since no crucible is necessary, FZ growth is the method of choice for complicated oxide crystals with centimeter-long axes and millimeter-diameter

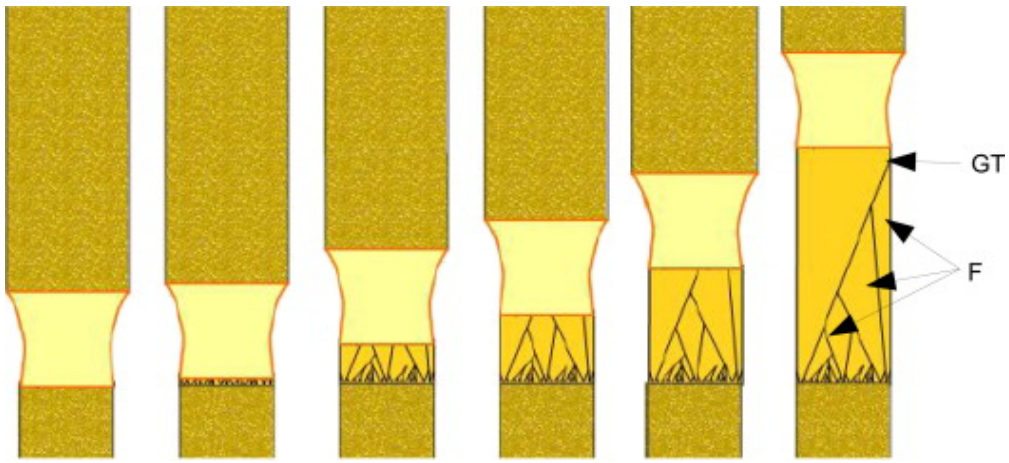

Figure 1.7: Schematic of FZ synthesis. As the melt, or float zone, moves into the feed rod, it leaves crystals in its wake (F). The crystals compete with one crystal, eventually winning. It is signified by a grain termination (GT). (Reprinted (adapted) with permission from [71]. Copyright 2015 Elsevier B.V.)

diameters, particularly for precursors that react with crucible materials. Controlling the atmosphere also enables the creation of intricate gas habitats. Surface tension-restricted diameters, difficult-to-control parameters, and poor performance with high vapor pressure or high viscosity materials are all factors that limit FZ development [66].

The difficulty in controlling parameters is especially an obstacle because each material grows differently and requires a different level of tedious parameter adjustment. Some materials may need extensive care from experimenters to be grown. Key process factors, such as the melting and rods' temperature distribution, are not well known even when parameters are tuned. Given that certain chemicals absorb more light than others, the temperature may even vary depending on the makeup of the powders. The adoption of this approach more widely is hampered by adjusting factors, including the heater power, internal temperature, atmospheric composition, pressure, pull rate, and rotation rate [69].

While some efforts have been made to comprehend the dynamics of the molten oxide zone, a comprehensive explanation is still elusive. *In situ* experiments are currently limited to optical imaging, pyrometer temperature sensing [80], and neutron imaging [81]. Techniques like x-ray diffraction, atomic pair distribution function analysis, and their associated tomography techniques,

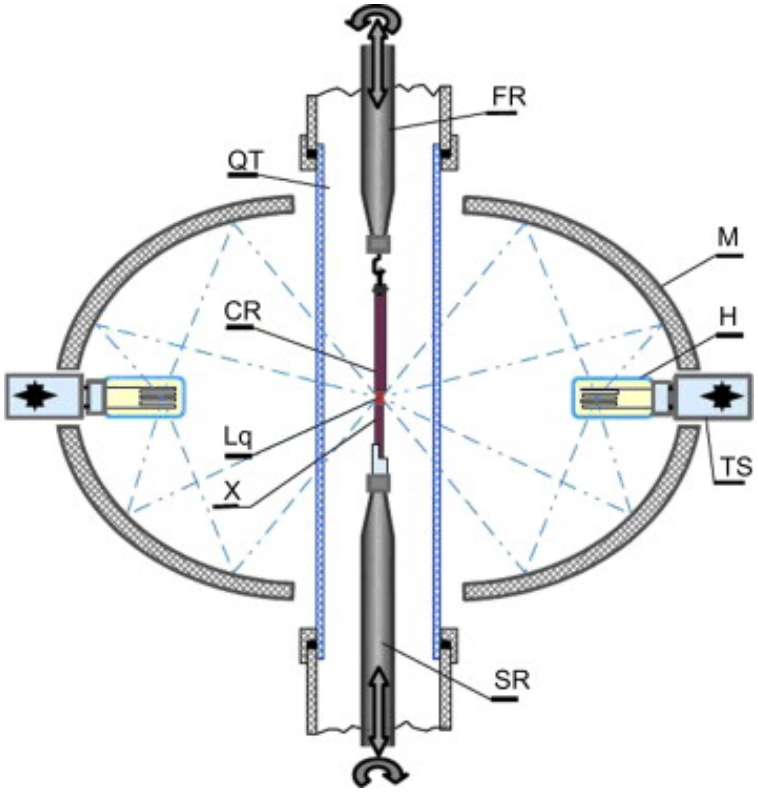

Figure 1.8: Schematic of a type of OFZF device. (Reprinted (adapted) with permission from [71]. Copyright 2015 Elsevier B.V.)

which are sensitive to the atomic structure of the materials, the orientation of the crystals, and their microstructure, could offer more insight into how FZ crystal growth occurs and offer a method for determining the effects of processing parameters on the crystal quality and properties.

Researchers carried out multiple methods mapping out distribution including pair distribution function computed tomography (ctPDF) [82], scanning nanostructure x-ray microscopy (SNXM) [83], scanning nanostructure electron microscopy (SNEM) [84], diffraction contrast tomography (DCT) [85], and three-dimensional x-ray scattering microscopy (3DXRD) [86, 87, 88].

However, it is still a significant challenge to realize fast, automated characterization, a prerequisite for in-situ measurement. Recently, an automated and rapid method was reported for the nondestructive mapping of crystal grains in a rod-shaped sample [89]. I proposed an even simpler and faster new algorithm to address the challenge based on its idea. I introduced it and an example of how to apply it on a TiO_2 crystal rod and its potential usage in the optical floating zone furnace (OFZF) in Chapter 6.

1.6 Infrastructure for structure analysis

The infrastructure I developed solved the scientific questions in the earlier sections and can be applied to other research fields. I made them into open-source python packages to benefit most of the science community.

Chapter 2: X-ray scattering and pair distribution function

2.1 Total x-ray scattering method

As a non-destructive analytical method, x-ray scattering techniques may gather details on the chemical makeup, physical characteristics, and crystal structure of materials and thin films. These methods are based on observing the scattered intensity of an X-ray beam striking a sample as a function of incident and scattered angle, polarization, and wavelength or energy.

I will briefly introduce the total x-ray scattering experiment to understand the physics behind this technique. Then, I will discuss the scattering caused by a solitary electron before moving on to the scattering caused by a solitary atom with Z electrons. When considering electrons as classical particles, the electron density may be expressed as $\rho(\mathbf{r})$. The field from one atom is a coherent superposition of all contributions from various volume elements within the charge distribution.

2.1.1 X-ray powder diffraction experiment

Unlike the typical Bragg scattering, the total x-ray scattering tends to include the scattering intensity from the whole Q range instead of the discrete values equal to reciprocal space vectors. To achieve it, experimenters collect diffraction images of samples on large two-dimensional detectors. An example of diffraction of fcc nickel is shown in the Figure 2.1(a). It is an average of the 3000 frames, and each one is collected in 0.1 s. They are the results of subtracting the light frames from the dark frames. The light frame is the image collected during exposure, while the dark frame is the image collected without an x-ray. Their subtraction is the number of the photons hit on every pixel on the detector in 0.1 s, disregarding the dark current in the detector.

Aside from the diffraction image, experimenters also need to know the detector's geometry,

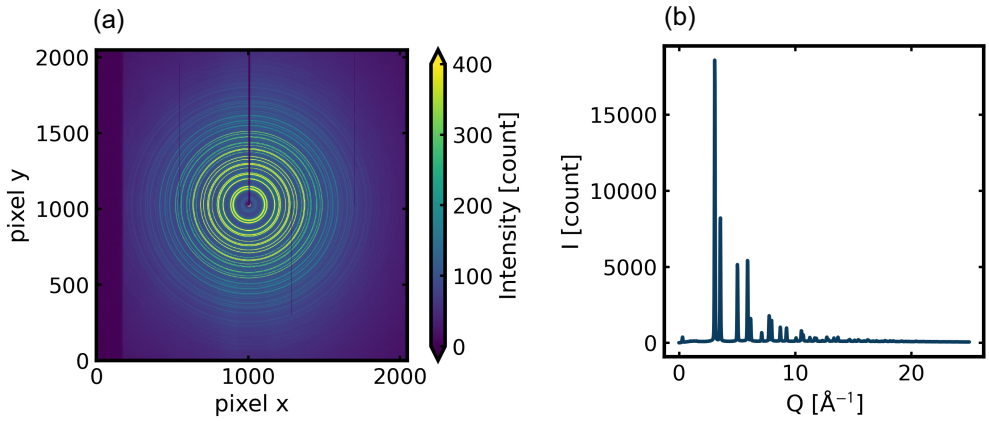

Figure 2.1: An example of total x-ray scattering experiment results. (a) A representative diffraction image of fcc nickel powder on a Perkin Elmer detector. (b) The integration result of an image in (a).

including the distance from the sample, the orientation, the size of pixels, and the number of pixels on each axis. They calibrate these parameters by fitting the positions of the Debye-Scherrer rings of standard materials, e.g. fcc nickel. Once they know the parameters, they bin the pixels along the arcs centering the beam spot on the detectors and calculate the average for the bins. They then map these average intensities to the norm of the momentum transfer of the arcs and finally obtain the intensity spectrum ($I(Q)$), plotted in Figure 2.1(b).

2.1.2 Momentum transfer

In the Section 2.1.1, I introduced that each arc on the diffraction image corresponds to a norm of the momentum transfer. In this section, I will explain what momentum transfer is. I showed an x-ray total scattering experiment in the Figure 2.2. The $\mathbf{k}_i$ is the wave vector of the incident beam, assuming that the beam is a plane wave. Elastic scattering happens between the inner electron in the atoms in the samples and the incident wave. As a representative, I picked on scattering vector $\mathbf{k}_f$. Scattering angle 2θ is the angle between the $\mathbf{k}_f$ and $\mathbf{k}_i$. Momentum transfer is the difference between the diffraction vector and the incident vector (Eq. 2.1).

$$\mathbf{Q} = \mathbf{k}_f - \mathbf{k}_i \tag{2.1}$$

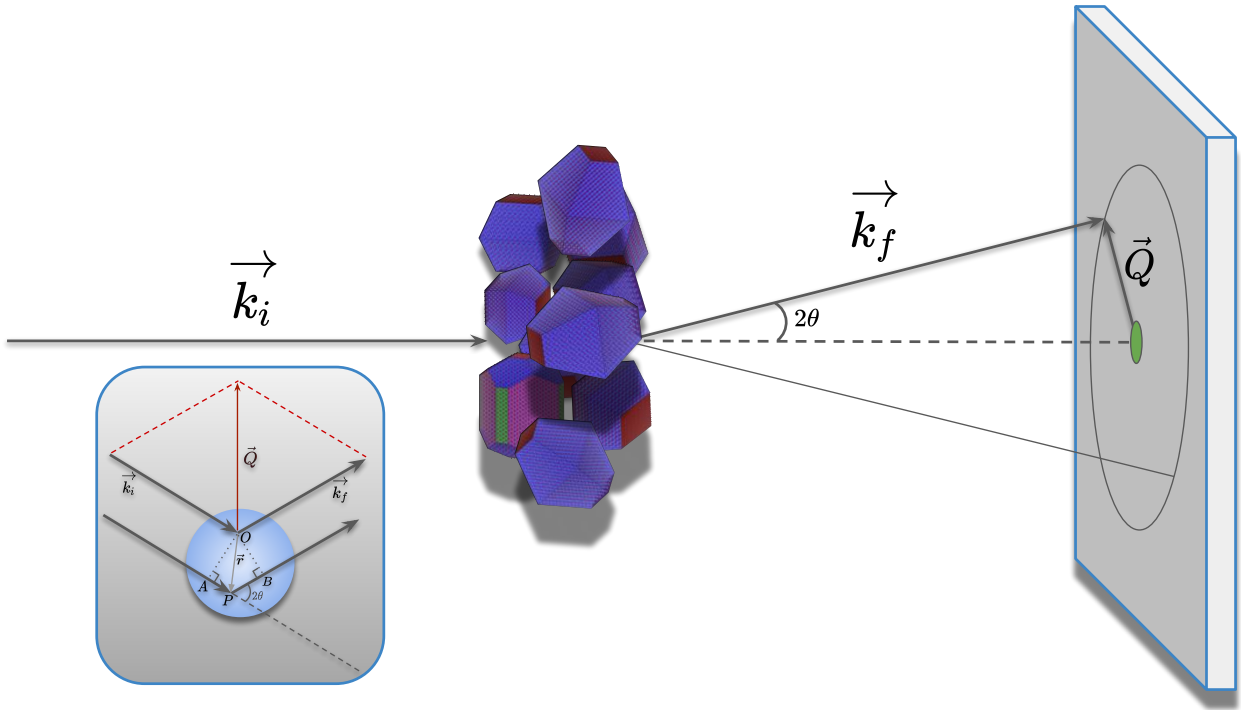

Figure 2.2: Illustration of elastic x-ray scattering from a randomly oriented, isotropic sample of rutile and anatase TiO_2 nanocrystals. (Reprinted (adapted) with permission from [90]. Copyright 2020 Columbia University)

Because of energy conservation, the $\mathbf{k}_f$ should have the same norm as the $\mathbf{k}_i$. It is the $2\pi/\lambda$, where λ is the wavelength of the incident beam. I use the geometry to calculate the norm Q as a function of θ and λ in Eq. 2.2.

$$Q = \frac{4\pi}{\lambda} \sin\theta \tag{2.2}$$

All pixels on a ring on the detector centering around the beam spot have the same θ because of the geometry. Therefore, experimenters can map one Q to the average intensity I on one ring in Section 2.1.1.

2.2 Scattering intensity of total scattering

2.2.1 Scattering of a single atom

I demonstrated how I could obtain the $I(Q)$ data in total x-ray scattering experiments. Now, I will show how this data relates to the atomic structure. As a beginning, I will discuss the x-ray

scattering from a single atom. I show the geometry of it in the inset of Figure 2.2. To calculate the changes in the scattering field of an atom, I will calculate the phase shift and amplitude change in the scattering from one electron. Because of the nature of elastic scattering, there is no change in the amplitude. I only need to calculate the phase shift. The phase shift is defined as the difference of the phase between the incident and diffraction plane waves, as calculated in Eq. 2.3.

$$\begin{aligned}\Delta\phi(\mathbf{r}) &= \mathbf{k_f}\cdot\mathbf{r} - \mathbf{k_i}\cdot\mathbf{r} \\ &= (\mathbf{k_f} - \mathbf{k_i})\cdot\mathbf{r} \\ &= \mathbf{Q}\cdot\mathbf{r}\end{aligned} \tag{2.3}$$

Each inner electron in the atom scatters the incident plane and generates a plane wave with the same phase shift in Eq. 2.3. I sum scattering intensities up with the weight atom density $\rho(\mathbf{r})$, and obtain Eq. 2.4.

$$f_0(\mathbf{Q}) = \int_0^\infty \rho(\mathbf{r}) e^{-\imath\mathbf{Q}\cdot\mathbf{r}} \mathrm{d}^3\mathbf{r} \tag{2.4}$$

The scattering field $f_0(\mathbf{Q})$ has name form factor. Shown in Eq. 2.4, it is a Fourier transformation of the electron density in an atom.

2.2.2 Scattering of an atom assemble

I described the scattering of one atom. I will use it to calculate the scattering field of an atom assembled. I assume that the assembly has countable atoms. I define the vector $\mathbf{r}_i$ describing the position of the i-th atom. Because of the assumption of coherent scattering, I can add up the scattering from each atom (Eq. 2.4) in the assemble and obtain the total scattering field in Eq. 2.5.

$$\begin{aligned}\Psi(\mathbf{Q}) &= \sum_i f_i(Q) e^{-\imath\mathbf{Q}\cdot\mathbf{r}_i} \\ \Psi^*(\mathbf{Q}) &= \sum_i f_i^*(Q) e^{\imath\mathbf{Q}\cdot\mathbf{r}_i}\end{aligned} \tag{2.5}$$

It shows that the scattering field is a linear combination of plane waves $e^{-\imath \mathbf{Q}\cdot\mathbf{r}_i}$ whose coefficients are $f_i(Q)$.

2.2.3 Scattering of atom assemble

Finally, I will deduce the scattering intensity $I(Q)$ using the scattering field equation (Eq. 2.5). By its definition, I calculate the two norms of the scattering field in Eq. 2.6 and obtain the scattering intensity.

$$\begin{aligned} I_{coh}(\mathbf{Q}) &= |\Psi(\mathbf{Q})|^2 = \Psi(\mathbf{Q})\Psi^*(\mathbf{Q}) \\ &= \sum_i \sum_j f_j^* f_i e^{-\imath \mathbf{Q}\cdot(\mathbf{r}_i - \mathbf{r}_j)} \\ &= \sum_{i,j} f_j^* f_i e^{-\imath \mathbf{Q}\cdot\mathbf{r}_{ij}} \\ &= N\langle f^2 \rangle + \sum_{i \neq j} f_j^* f_i e^{-\imath \mathbf{Q}\cdot\mathbf{r}_{ij}} \end{aligned} \tag{2.6}$$

I pull the contribution of $i = j$ pairs out of the contribution and conclude that the pair distances r_{ij} determine the coherent scattering intensity of an atom assemble.

2.2.4 Scattering of isotropic atom assembles

Here, I defined the isotropic atom assembles as a volume filled by finite identical atom assembles, where the probability of finding one assembly at any orientation is equal. Powder of crystals can be viewed as an isotropic sample when it is ground fine enough, but an isotropic sample doesn't have to be crystals. A homogeneous liquid is also an isotropic sample. I derived the scattering intensity of the isotropic sample here. After defining the angle between $\mathbf{Q}$ and $\mathbf{r}_{ij}$ as θ, I wrote the coherent scattering intensity as Eq. 2.7.

$$I_{coh}(\mathbf{Q}) = \sum_{i,j} f_j^* f_i e^{-\imath Q r_{ij} cos\theta} \tag{2.7}$$

The probability of finding interatomic distance vectors r_{ij} concerning $\mathbf{Q}$ is equal in all directions, so the vector $\mathbf{Q}$ reduces to a magnitude. I obtained the intensity of coherent scattering in Eq. 2.8

by taking the spherical integral of the exponential term in Eq. 2.7.

$$I_{coh}(Q) = \sum_{i,j} f_j^* f_i \frac{\sin\left(Qr_{ij}\right)}{Qr_{ij}} \tag{2.8}$$

It is the Debye equation [91]. It shows that the coherent scattering intensity of isotropic system is a weighted summation of *sinc* function of Qr_{ij}, where r_{ij} is the distances between the i-th atom and j-th atom. It tells that the $I(Q)$ data described in Section 2.1.1 encode the information of atomic pair distances. Since they are solely determined by the atomic structure, analysis on the $I(Q)$ or functions deduced from $I(Q)$ can decode the information about the atomic structure.

2.3 X-ray scattering of crystals

In Section 2.1, I demonstrated the method of x-ray total scattering experiments and why it can reveal the atomic structure of the isotropic system. In this section, I will present the x-ray scattering intensity of crystals, which are used in the experiments described in the following chapters.

2.3.1 Perfect crystals

The perfect crystals are the atoms on lattices with translational symmetry in the atom positions. Because of the symmetry, I can describe the position of one atom using three coordinates in the lattice frame in Eq. 2.9.

$$\mathbf{r}_j = x_j\mathbf{a} + y_j\mathbf{b} + z_j\mathbf{c} \tag{2.9}$$

According to the derivation in [92], only the Q following the Eq. 2.10 will have non-zero diffraction for the perfect crystal.

$$\mathbf{Q}_{hkl} = h\mathbf{a}^* + k\mathbf{b}^* + l\mathbf{c}^* \tag{2.10}$$

The (hkl) are Miller indices. They must be integers for the scattering vector to have non-zero intensity. By plugging the equation of atom positions (Eq. 2.9) and momentum transfer (Eq. 2.10)

into the equation of scattering amplitude (Eq. 2.5), I obtain the scattering amplitude of a crystal in Eq. 2.11.

$$F_{hkl} = \sum_{j=1}^{N} f_j \mathrm{e}^{-2\pi\imath\left(hx_j+ky_j+lz_j\right)} \tag{2.11}$$

It describes a one-to-one mapping between a scattering intensity peak and a (hkl). The peak height is a sum of the atom position-related terms. For noncrystalline materials like liquids, molecules, atomic clusters, and small nanoparticles, where the structural coherence between atomic ensembles is minimal, it is frequently preferable to calculate the scattering intensity with a continuous function of Q, which we describe in the following section. The statement is true even though methods for structural analysis based on calculating Bragg intensities from crystallographic unit cells and symmetry relationships often work well.

2.3.2 Imperfect crystals

The crystal is never an infinite large volume with perfectly aligned symmetric atoms. The atoms may deviate from their positions in multiple ways. One common phenomenon is thermal vibration. The atoms randomly oscillate around their equilibrium positions due to the thermal motion, and it introduces uncertainties in the positions of the atoms. Thus, the Q_{hkl}, the scattering intensity is damped by the Gaussian function in Eq. 2.11, which is the Debye-Waller factor.

Besides the thermal vibration, the atoms may deviate from the original lattice point even without thermal motion. Factors like substituted, missing, added atoms in the lattice, or misaligned atomic layers can cause deviation. Because of deviation, the scattering intensity will also be damped but may not be the same as the thermal vibration.

2.3.3 Mosaicity

The mosaicity, also known as mosaic, mosaic spread, or rocking angle, describes a crystal's quality by describing the degree of accuracy of its lattice translations. A macromolecular crystal might have several packing flaws and content heterogeneities. However, the conventional explana-

tion of mosaicity simplifies the matter by supposing that the crystal is made up of mosaic blocks. The diffraction from each block will be continuous with that from all other blocks if all the blocks are correctly aligned, and the mosaicity will be zero. The resultant diffraction is dispersed when the mosaic blocks become disorganized, for example, in the flash-cooling process. Viewed as expanding the rotation angle necessary to acquire the intensity of a particular reflection in the rotation approach for collecting diffraction data, the mosaicity is thus specified in the unit of angle.

The term "rocking angle" is occasionally used to describe mosaicity. The measurement, which calls for specific tools, pertains to the angle that a diffractometer must be swung through to capture a reflection. According to data reduction software, mosaicity often includes the instrument's and crystal quality contributions. Beam divergence and x-ray spectrum quality are two supporting factors.

2.4 Pair distribution function (PDF)

I introduced the concepts of total x-ray scattering in the previous sections. Starting from this section, I will describe a vital technique based on the total x-ray scattering experiments, the pair distribution function (PDF).

2.4.1 Introduction

The pair distribution function (PDF) is a statistical measure used in the analysis of the structural properties of materials. It provides information about the spatial arrangement of atoms within a material, including the distances between atoms and the preferred orientations of the atoms.

The concept of the PDF can be traced back to the early 20th century when researchers began using X-ray diffraction techniques to study the structures of crystalline materials [93]. In the 1950s, researchers started using neutron diffraction to study the structures of materials, and the PDF became an essential tool for analyzing the results of these experiments [93].

The PDF has since been widely used in studying various materials, including metals, ce-

ramics, polymers, and biomaterials [94]. It has also been applied to the study of liquids, glasses, and amorphous materials and to the analysis of materials under extreme conditions, such as high pressure and high-temperature [95, 96].

The PDF is typically obtained by measuring the intensity of diffracted X-rays or neutrons as a function of the scattering angle and the scattering wavevector and then using mathematical techniques to convert this data into a PDF. The PDF can be used to identify the presence of specific types of atoms within a material, determine the distances between atoms, and study the local atomic structure of a material. It can also be used to study the long-range ordering of atoms in a material and to identify the presence of defects or disordered regions.

In the following sections, I will go into the details about how to obtain PDFs from the total x-ray scattering and how to model it using the attenuated crystal model (ACM).

2.4.2 Structure function

To show how to obtain the PDF from the total x-ray scattering data, I will first introduce the idea of the structure function $S(Q)$. According to the Debye Equation (Eq. 2.8), the coherent scattering intensity is related to both the scattering of individual actions ($f_i f_j$) and the arrangement of the atoms (r_{ij}). By normalizing the scattering intensity in Eq. 2.12, I will obtain a function $S(Q)$ representing the arrangement of atoms.

$$S(Q) - 1 = \frac{I_{coh}(Q) - \sum c_i \left|f_i(Q)^2\right|}{\sum c_i \left|f_i(Q)^2\right|} \tag{2.12}$$

It is the structure function. By plugging in the Debye Equation (Eq. 2.8), I get the explicit expression about how the r_{ij} determine the $S(Q)$ (Eq. 2.13).

$$S(Q) - 1 = \frac{1}{N\langle f\rangle^2} \sum_{i \neq j} f_j^* f_i \frac{\sin\left(Qr_{ij}\right)}{Qr_{ij}} \tag{2.13}$$

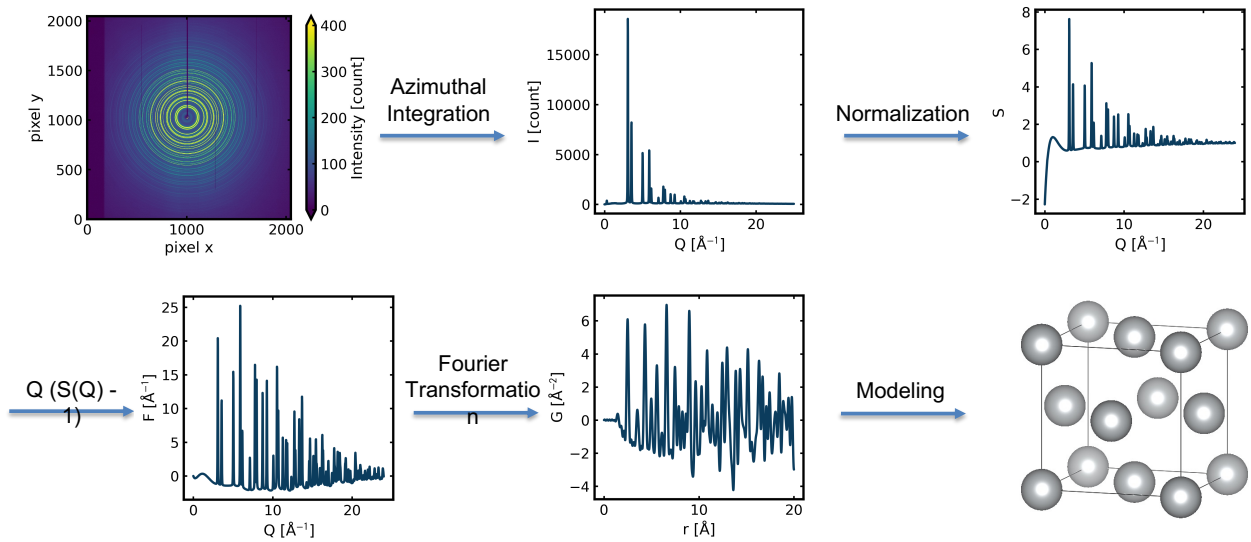

Figure 2.3: The path from scattering intensity data to pair distribution function for a nickel sample. I is scattering intensity. S is structure function. F is reduced structure function. G is pair distribution function. Q is the momentum transfer. r is the atomic pair distance.

Because of the thermal vibration and other effects, the atoms may deviate from the equilibrium positions $\mathbf{r}_i$. The deviation will appear as the damping term in the $S(Q)$ shown in Eq. 2.14.

$$S(Q) - 1 = \frac{1}{N\langle f\rangle^2} \sum_{i\neq j} f_j^* f_i \left(e^{-\frac{1}{2}\sigma_{ij}^2 Q^2}\right) \frac{\sin\left(Qr_{ij}\right)}{Qr_{ij}} \tag{2.14}$$

The σ_{ij} presents the system's standard deviation of the atom positions.

In Figure 2.3(a-b), I visualize the scattering intensity and the structure function of standard fcc nickel. There is a change in the intensity of peaks in the data from (a) to (b), showing the effect of the normalization in the $I(Q)$ to $S(Q)$ transformation Eq. 2.12.

2.4.3 PDF as Fourier transformation

To obtain the PDF, I multiply the $S(Q)$ by Q and obtain the $F(Q)$, which is the reduced structure function. By using the Fourier transformation on $F(Q)$, I will finally have a function of r. It is the x-ray pair distribution function $G(r)$. Because $F(q)$ is an odd function, only the sin

terms give non-zero values. I rewrite the Fourier transformation as Eq. 2.15.

$$G(r) = \frac{2}{\pi} \int_{Q_{\min}}^{Q_{\max}} Q\,[S(Q) - 1] \sin(Qr)\,\mathrm{d}Q \tag{2.15}$$

Because of the limitation of experiments, the transformation is usually done on a finite range of Q. There is a lower limit $Q_{\min}$ because the beam spot will block the beam at a low θ angle, and the $I(Q)$ at the low Q range is close to zero. The largest θ is also limited by the geometry and the wavelength, and thus there is an upper limit $Q_{\max}$. The Eq. 2.15 tells one way to calculate the PDF. It is to calculate the $S(Q)$ using the atom positions $\mathbf{r}_i$ and then transform it to the PDF.

In Figure 2.3(c-d), I depict the example of the $F(Q)$ and $G(r)$ for fcc nickel. They show the effect of the Fourier transformation on the data.

2.4.4 PDF as atomic distance histogram

The PDF obtained by Fourier transformation of reduced structure function (Eq. 2.15) encodes the information of the atomic pair distances. I showed it by plugging the Debye equation of the structure function Eq. 2.8 in the Fourier transform of it Eq. 2.15. The result is the Eq. 2.16.

$$\begin{aligned} G(r) &= 4\pi r \rho(r) - 4\pi r \rho_0 \gamma_0(r) \\ \rho(r) &= \frac{1}{4\pi r^2 N} \sum_i \sum_{j \neq i} \frac{b_i b_j}{\langle b \rangle^2} \delta\left(r - r_{ij}\right) \end{aligned} \tag{2.16}$$

The $\rho(r)$ is the atomic pair density, which depicts the number density of atomic pairs in the distance r. The ρ_0 is the average number density of atoms. The $\rho(r)$ encodes the information of atomic pairs r_{ij}. It is related to a weighted average of the δ functions at the r_{ij}. It tells how to calculate PDFs based on the atom positions in real space.

In reality, the atoms may deviate from their average lattice points ($r_i j$), and the δ in the

calculation of $rho(r)$ Eq. 2.16 becomes the summation of Gaussian functions in Eq. 2.17.

$$\rho\left(r\right) = \frac{1}{4\pi r^2 N} \sum_{i}^{N} \sum_{j \neq i}^{N} \frac{b_i b_j}{\langle b \rangle^2} \exp\left[-\frac{1}{2}\left(\frac{r - r_{ij}}{\sigma_{ij}}\right)^2\right] \tag{2.17}$$

The σ_{ij} represents the deviation of atom positions from $r_i j$. The deviation may come from thermal vibrations, static disorders, correlated motion, and instrumental broadening. I summarized their contribution in the mathematical formula in Eq. 2.18.

$$\sigma_{ij} = \sigma'_{ij}\sqrt{1 - \frac{\delta_1}{r_{ij}} - \frac{\delta_2}{r_{ij}^2} - Q_{broad}^2 r_{ij}^2} \tag{2.18}$$

The σ'_{ij} is the deviation from the thermal vibration. The terms with δ_1 and δ_2 are the linear and quadratic corrections for the correlated motion effects [27]. The term with Q_{broad} is a *ad hoc* correction for instrumental broadening.

2.4.5 Characteristic functions

In the sections below, I assume that the atoms distribute in an infinite large volume. This assumption may hold for most of the cases where the crystallites are large enough. However, for nanocrystals or nanoparticles, the finite-size effects will show up in the measured PDF. In these cases, I need to introduce a correction for the equation of $\rho(r)$ Eq. 2.17. The correction is an attenuation function forming an envelope of the PDF, called the characteristic function (CF). The analytical form of attenuation depends on the shape and size of the volume of atoms. Here, I demonstrated some example CFs from [90] using the data of anatase TiO_2 in Figure 2.4. In the example, the effects using different CFs with similar parameters are hard to observe visually, whether the CF is a lognormal distribution of spheres, a prolate or ellipsoidal sphere, or a simple sphere. More information from the statistics needs to be included to evaluate the results, but it is hard to select the correction solution deterministically.

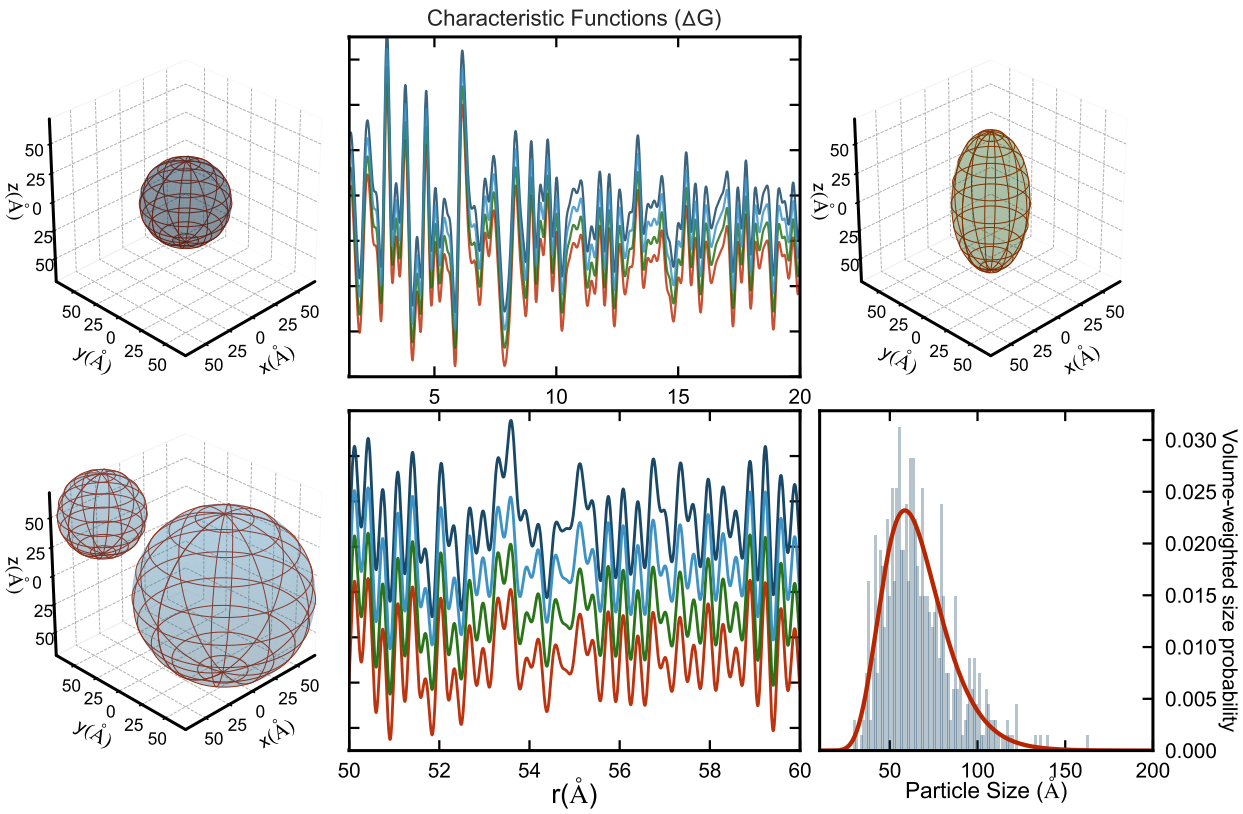

Figure 2.4: Different characteristic form and distribution functions for anatase nanoparticles. Refined dimensions and parameters and impact on fit residuals ΔG. The 3D plots show the shape that CF presents. The middle top panel shows the PDF attenuated by different CFs. The middle bottom panel shows the residuals from fits. The bottom right panel shows TEM statistics of the particle size of the samples. (Reprinted (adapted) with permission from [90]. Copyright 2020 Columbia University)

2.4.6 Model PDF

In the previous sections, I deduced the PDF as Fourier transformation of reduced structure function (Eq. 2.15) and the atomic pair distance histogram (Eq. 2.16). They show the two ways to calculate PDF using the atom positions ($\mathbf{r}_i$). I call them real space and reciprocal space calculations because of their starting points. Based on the two ways to calculate PDF, the software can refine a structure model to make its PDF match the measured one. The refinement is usually done by minimizing the χ^2 (Eq. 2.19).

$$\chi^2(p_1, p_2, \ldots) = \sum \left(G_{exp}(r_n) - G_{calc}(r_n)\right)^2 \tag{2.19}$$

The parameters p_i describing a model are changed through least-squares refinement until the difference between G_{calc} and G_{exp} is minimized. The minimization can be done by any quadratic optimization method. Researchers usually use the reverse Monte Carlo for the big box model and the least square regression for the small box model [3]. They have developed software to conduct the refinement [97, 98, 99, 100]. I used the DIFFPY-CMI [100] in developing the software infrastructure and data analysis.

2.4.7 Evaluate models

The goodness-of-fit is introduced in Eq. 2.20, describing how well a fit is.

$$R_w(p_1, p_2, \ldots) = \sqrt{\frac{\sum_n [G_{exp}(r_n) - G_{calc}(r_n))]^2}{\sum_n G_{exp}^2(r_n)}} \tag{2.20}$$

Compared with χ^2, which may vary considerably depending on the measured data, the R_w is usually between 0 and 1. It is easier for people to have a sense of goodness using the index R_w. However, a low R_w doesn't necessarily mean a good model. Multiple factors should be considered, including the number of parameters, the range of values, knowledge of chemistry, and results from another measurement.

Chapter 3: Autonomous experiments and streaming data reduction

3.1 Introduction

Automated workflow and streaming data reduction are essential in today's synchrotron x-ray scattering experiments [6, 89]. Users may have a large batch of samples and limited beamtime to collect [10]. Or they need to see the data in a preliminary experiment and then quickly decide the next step on-site [101]. In the former case, they needed a system to run an automated workflow to save the time of operating the devices with a simple interface. In the latter case, they may want to see the x-ray diffraction (XRD) or pair distribution function (PDF) pattern on-site with an interactive view to decide on the following measurement step.

OPHYD and BLUESKY [12] at NSLS-II build up the framework for these features, but there is still a large gap between what it provides and users' specific needs at the 28-ID beamline. Users want to collect x-ray scattering data without knowledge of technical details about instruments. They would like to experiment without understanding the python generators or remembering to move shutters to the correct position. Meanwhile, They want to see XRD and PDF data directly on the screen and their hard disk without opening any software for data processing.

However, it is far from a simple tasking given the BLUESKY and OPHYD. Thus, I designed the XPDACQ software bundle based on the BLUESKY and OPHYD to address the difficulties in the x-ray experiments, especially at the beamline 28-ID.

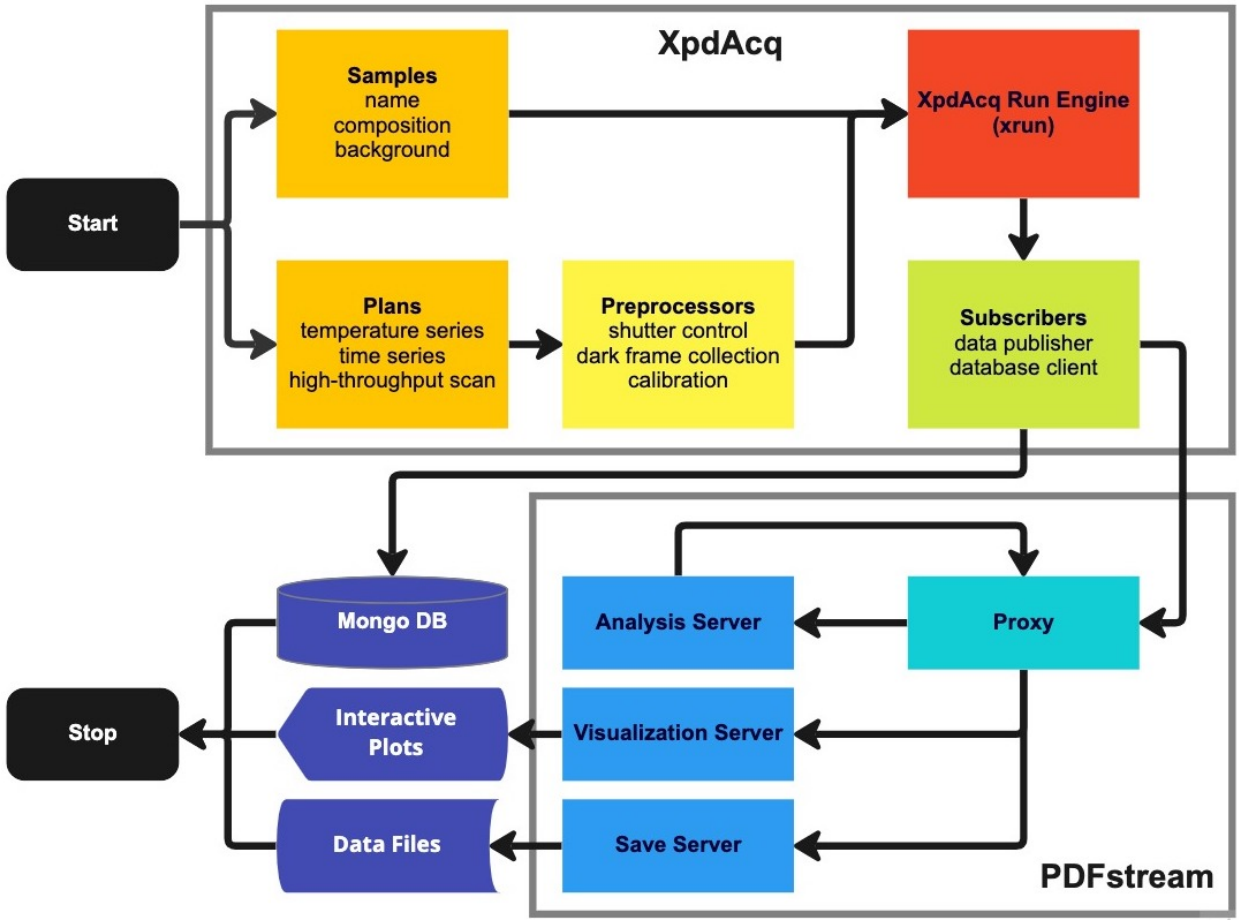

Figure 3.1: Brief flowchart of the XPDACQ and PDFSTREAM. The start is the user command, and the end is the end of the experiments and data processing. The rectangles are the components to process the data or command. The other shapes are the destination of the data flow.

3.2 Method

I developed the XPDACQ package for the automated workflow and the PDFSTREAM package for the streaming data reduction. I demonstrate a flower chart of data flow (Figure 3.1).

I listed the brief descriptions of the components here.

- **Start**: Users start the experiment by typing ‘xrun(1, 2)‘.
- **Samples**: XPDACQ retrieves information of the 1st sample.
- **Plans**: XPDACQ retrieves the commands of the 2nd plan.

- **Preprocessors**: They look at the plan and amend it on the fly.
- **XpdAcq Run Engine**: It executes the plan and gathers the data. It talks to the OPHYD control layer, omitted in the flowchart because it is the main topic.
- **Subscribers**: They do postprocessing for the data, including sending the data into the network and dumping data into the database.
- **Proxy**: It sends and receives the data from the servers.
- **Analysis Server**: It makes the data reduction to generate XRD and PDF data.
- **Visualization Server**: It visualizes the data.
- **Save Server**: It saves data files on the hard disk.
- **Stop**: It represents the end of the data processing.

The XPDACQ helps users manage the samples and experiments during beamtime and takes care of the challenging parts of the measurement, including shutter control, dark frame collection, and calibration.

One challenge during the beamtime is remembering what sample to measure and how to do the measurement. The XPDACQ addressed this issue by recording the sample information and experiment plans in the memory. Uses only need to register the samples and plans; they can use them at any time by calling their number.

For example, if users want to run plan 0 on sample 0, they will type ‘xrun(0, 0)‘, and then the collection will start. The information is cached in memory and saved on the disk. The XPDACQ reloads them if the software restarts so that users no longer need to repeatedly enter the same information if they accidentally shut down the software. Users avoid wasting their minds on manually operating the devices so that they can focus more on the collected data.

Besides beamtime management, it is also a considerable burden for users to remember to open and close the fast shutter in a collection, collect a dark frame for subtraction, and calibrate

the sample detector distances. XPDACQ released these burdens by using the preprocessors. The preprocessors read the users' experiment plan step by step on the fly. When they find a step that deserves their attention, they will check if they need to mutate the plan to fulfill users' needs and mutate the plan accordingly.

For example, when the shutter control preprocessor finds out that users want to collect a detector image, it will check if they want a dark or light frame. If it is a dark frame, it will keep the shutter closed. In the other case, it opens the shutter to expose the detector and closes the shutter after the collection. The preprocessors enable users with little knowledge about the beamline to start their experiments immediately without worrying about missing crucial steps in their experiment plans.

While the XPDACQ frees the users from manually conducting and recording experiments, the PDFSTREAM automatically conducts the data processing, visualization, and saving for users, so that they can pay most of their attention to the scientific results.

For example, after a diffraction image is collected, users do not need to run any commands, and the dark subtracted masked images, XRD patterns, and PDF curves will directly show on the screen. These data are also dumped into the hard drive at the same time. With the convenience, users can decide what to do for the next step by analyzing data. They can visually investigate them by using the interactive window of the plots or run their analysis code on the output file. Advanced users can build servers to receive the data stream from PDFSTREAM servers and conduct further streaming data processing.

3.3 Result

I will show three typical experiments to demonstrate using the XPDACQ and PDFSTREAM software. They are a temperature series, a time series, and a high throughput experiment.

Temperature series is one of the most frequent in situ experiments. Here, I show an example of the phase transition of a metal-organic framework. Users used the one-line XPDACQ code

to register this experiment. The ‘Tramp‘ means a temperature ramping experiment, where the temperature will be ramped to a series of setpoints, and a diffraction image will be measured at each setpoint. The number 60 is the exposure time in seconds, and the numbers 30, 250 and 10 mean the start, the end, and the temperature step with the unit °C.

```
# Measure from 30 C to 250 C with 10 C step and 60 s exposure
Scanplan(Tramp, 60.0, 30.0, 250.0, 10.0)
# Run plan 5 (registered above) on sample 1
xrun(1, 5)
```

Users found the transition point by looking at the XRD and PDF waterfall plots (Figure 3.2). The XRD and PDF curves appeared on the fly whenever a diffraction image was taken. Thanks to this feature, they quickly found that the sample crystallized at 120 °C and melted at 180 °C. After 210 °C, the signal suddenly dropped to a low value. They later realized that the sample vaporated at the heating point. Therefore, they stopped collecting invalid data and started cooling. The software helps them probe the samples’ state and make decisions about the measurement with little effort in coding.

Another example of in situ experiment is the time series measurement. Here, I demonstrate an example of the gelation process. Users synthesized the sample using the boehmite and nitric acid on-site and started the measurement immediately using the easy XPDACQ code. The code means to collect a 50 s exposure diffraction image every 60 s for 10 times. Here, the 60 s is the interval between two beginnings of the consecutive exposures. In other words, the interval that the system stay quiet between the collections is 60 s - 50 s = 10 s.

```
# Measure every 60 s with 50 s exposure for 10 times
Scanplan(tseries, 50.0, 60.0, 10)
# Run the plan 6 (registered above) on sample 2
xrun(2, 6)
```

They saw how the XRD and PDF evolved with time in the waterfall plots (Figure 3.3). Every 60 s, an XRD and a PDF showed up in the plots. They overlapped the curves, shifted the offsets,

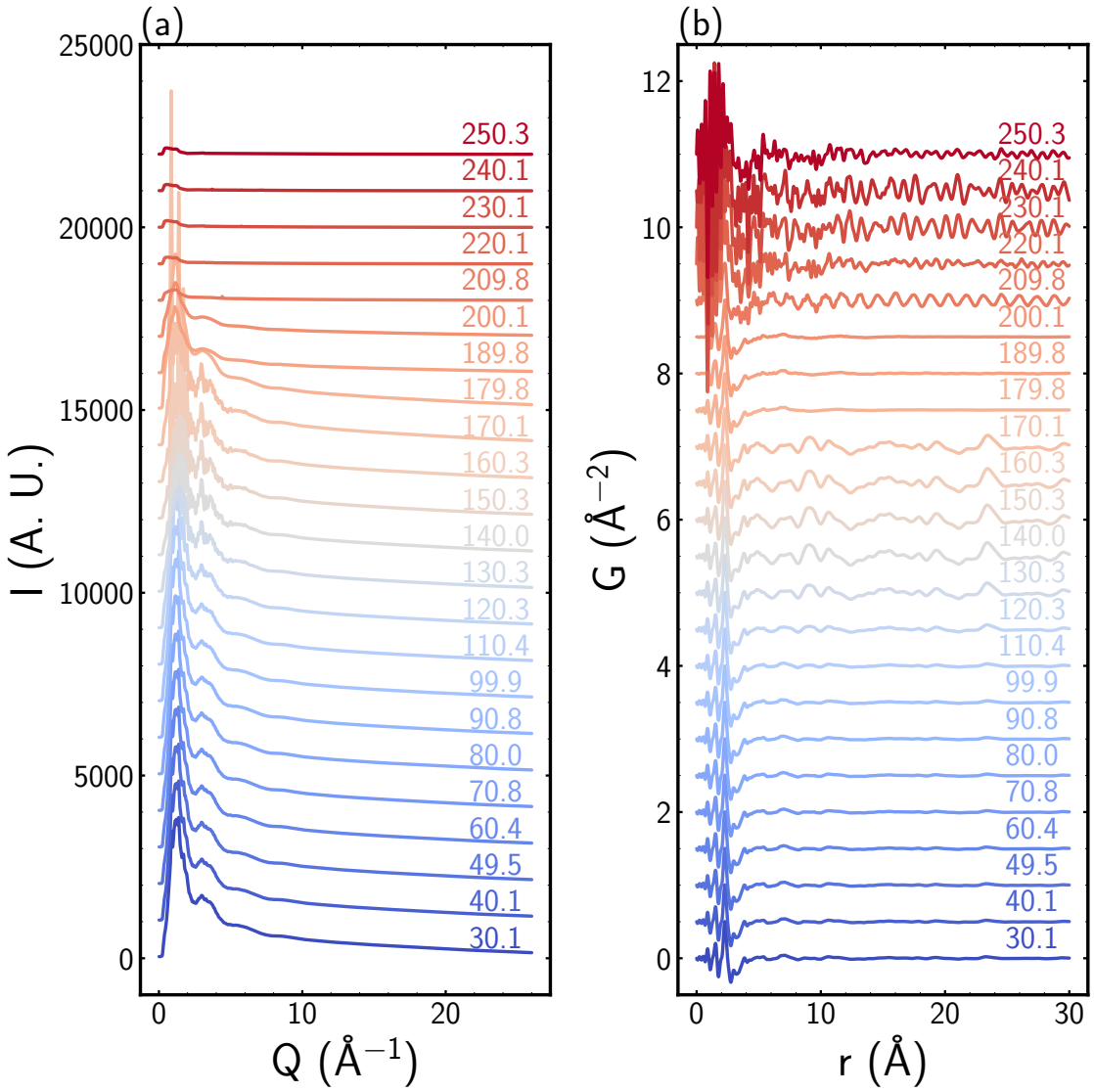

Figure 3.2: Temperature series of $Co(C_{12}O_2N_2H_{22})_3[CoCl_4]$ metal-organic framework: (a) powder x-ray diffraction (PXRD) data (b) x-ray atomic pair distribution function (PDF) data. The temperature in °C is annotated at the side of the data curves. The interactive plots at the 28-ID-beamline are similar to the figures here, except that the art style is different, and the temperature is printed in a table on the screen instead of annotated on the figure.

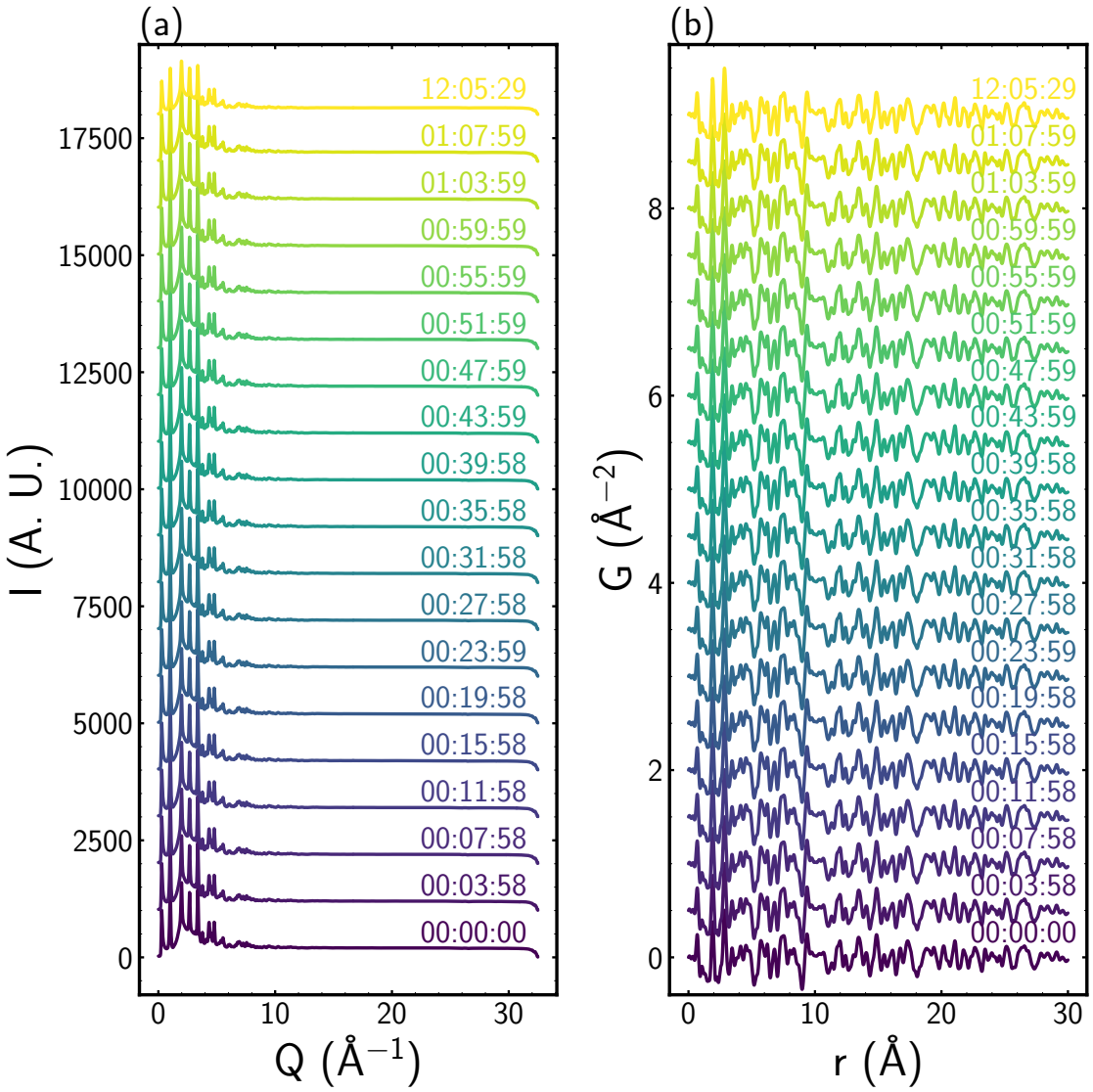

Figure 3.3: Time series of boehmite-nitric-acid mixture: (a) powder x-ray diffraction (PXRD) data (b) x-ray atomic pair distribution function (PDF) data. The time in "hour:minute:second" is annotated at the side of the data curves. The interactive plots at the 28-ID-beamline are similar to the figures here, except that the art style is different, and the time is printed in a table on the screen instead of annotated on the figure.

zoomed in using the interactive window, and found minor differences. They thought the gelation process could have been more versatile but only saw minor PDF evolution. It was a significant discovery to tune their synthesis conditions for the subsequent measurement. With the help of the XPDACQ and PDFSTREAM, they knew it on-site immediately during the measurement, which was crucial to determine how they would continue collecting the data and analyze them after beamtime.

Users can also conduct high-through experiments with the XPDACQ and PDFSTREAM software. In this case, I present an example of a PDF measurement for combinatorial chemistry. The sample is a flat glass substrate (Figure 3.4(a)) with nanoparticle mixtures made by microfluid methods. The task is to measure the PDF for all of them and process the data on the fly. Although there was no predefined experiment in XPDACQ, users used the underlying BLUESKY package to make the plan and give it to the XPDACQ. It defined a scan (Figure 3.4(b)) in a two-dimensional grid, where five PDFs were measured in a cross at each grid point.

Thanks to the streaming data processing, they immediately obtained all XRD and PDF data at the end of the scan. They further did the modeling on the PDF using our code to get the composition of each phase quickly for all the samples. The time to obtain all PDF data from the start of the experiment is as fast as 6 h40 min with exposure of 50 s. With the high-throughput experiment enabled by XPDACQ and PDFSTREAM software, it is possible to measure a large batch of samples without wasting time manually changing samples or moving the stages.

The examples above demonstrate how simple but powerful the XPDACQ and PDFSTREAM software are. Besides these typical experiments, I also offer users the flexibility to write more sophisticated plans and change the options, including the output file name patterns, the data processing parameters, and the path to save the data. They are stated in the documents, and advanced users at the beamline have used them for more technical experiments.

3.4 Conclusion

The XPDACQ and PDFSTREAM created a simple, flexible, and robust system for automated experiments and streaming data analysis for x-ray scattering experiments. It successfully addressed the difficulties in x-ray scattering experiments and considerably increased their efficiency.

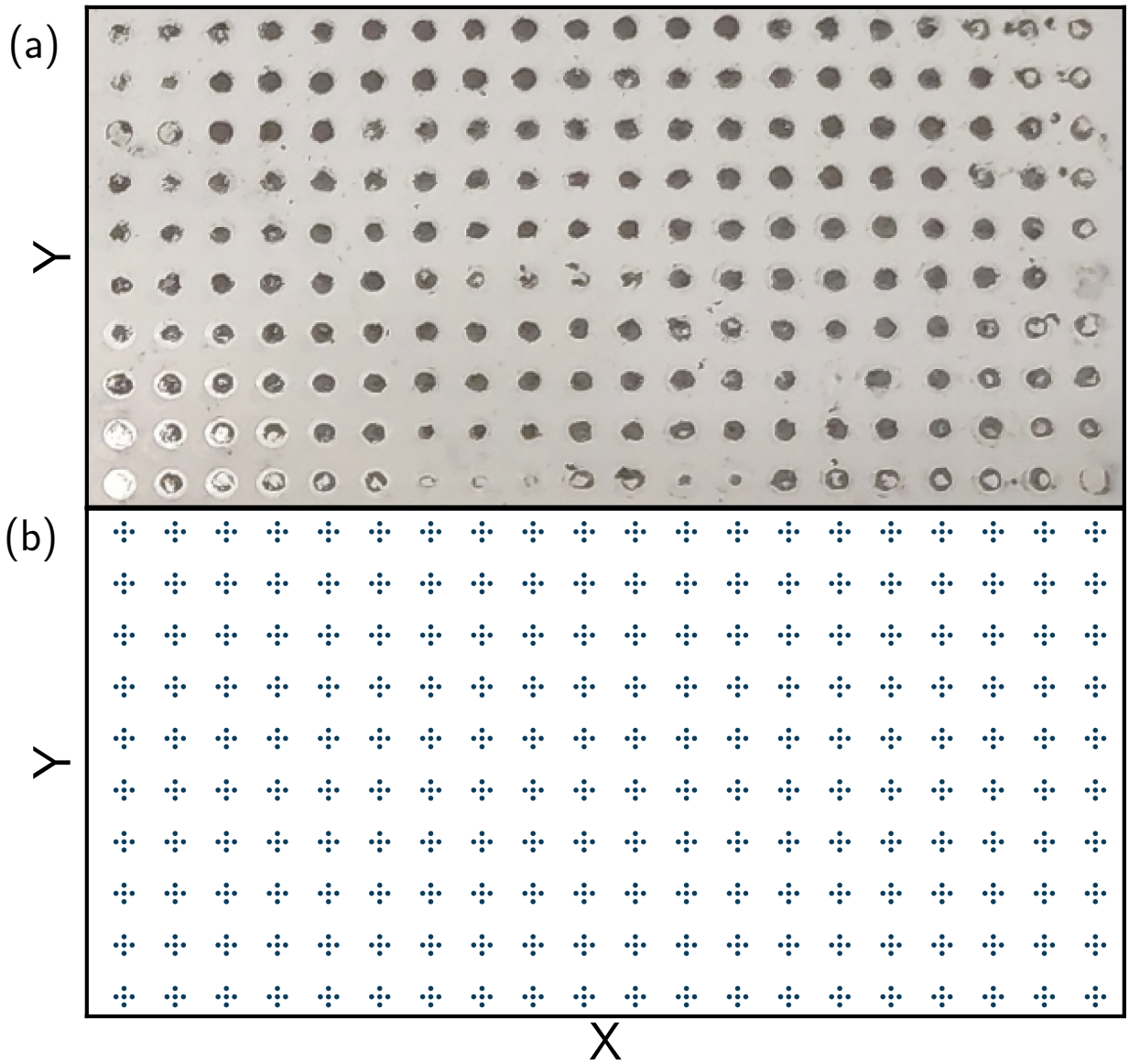

Figure 3.4: High-throughput PDF measurement. (a) Substrate with nanoparticle samples. (b) Schematic of beam spot positions on the sample in the scan.

Chapter 4: Quantitative analysis of the morphology and structure of metallic oxide nanoparticles

4.1 Introduction

Metal oxide nanoparticles have a number of important technological applications, for example, they are especially used in electronic devices, inlcuding gas sensors, solar cells, antennas [14]. In particular, TiO_2 has potential applications in lithium-ion batteries [102]. A particular synthesis challenge with TiO_2 is that it has multiple possible structural phases [103, 104, 105]. Differentiating between the various phases is particularly challenging when they are nanoparticles [106, 107] and it is crucial to be able to identify the structural phases of synthesized nanoparticles TiO_2. Beyond knowing the phase distribution in the sample, it is also important to study crystallite sizes and shapes [108], as well as the presence of common defects, since these factors have an important impact on the functionalities [109].

X-ray atomic pair distribution function (PDF) analysis is an important and powerful tool to use for this purpose because it reveals the local structure on nanometer length-scales, revealing quantitative information about the structural phase, particle morphology and defects in nanoparticulate materials, which is beyond the capability of traditional x-ray diffraction methods when the nanoparticles are small ($<$ 10 nm in diameter) [3]. One of the common methods for studying nanoparticles using PDF analysis is to use modeling to test structural models and extract quantitative information about the structure [27]. In general, there are two main categories of modeling methods, big box modeling, and small box modeling [106, 107], depending on the scale of the model and the optimization algorithm. In each category, there are also various ways to build the structural model. It is common to start with the most simple kind of modeling, for example, at-

Table 4.1: Sample synthesis information. T and t are the reaction temperature and time, respectively.

label	Ti (mmol)	glycolic acid (g)	sulfuric acid (ml)	water (ml)	T (C)	t (min)	ligand
T130	5	0.38	0.79	20	130	5	False
T160	5	0.57	0.622	20	160	30	False
T190	5	0.57	0.622	20	190	5	False
T190L	5	0.57	0.622	20	190	5	True

tenuated crystal modeling (ACM) [106, 107]. In this approach, the PDF of one structural phase is calculated based on a lattice with periodic boundary conditions. The PDF is then attenuated by a slowly varying in-r analytic function to simulate the effect of finite crystallite size [106, 107]. Whilst this sounds straightforward, in practice, it involves subtleties that are not obvious to a new practitioner. Given the growing importance of the PDF approach in nano-materials science and chemistry, we feel that it is helpful to the community to discuss the approach in a pedagogical way.

Here we address a gap in the literature and present a detailed workflow for applying ACM in a robust and accurate way, using TiO_2(Bronze) as an example. Using this approach, we find that the samples contain the TiO_2(Bronze) as the major phase and the TiO_2(Anatase) as the minor phase, obtain the structural parameters of both phases and that the particle sizes of the major phase are probably following a lognormal distribution.

4.2 Experiments and methods

Five samples were synthesized using the approach of Billet *et al.* [110]. The sample labels and the control variables used in their synthesis are shown in Table. 4.1. The most significant controlled variable was the reaction temperature, and we expected that it affected the structures of the nanoparticles. We also added ligands to two samples to simulate the environment of the real-world application.

PDF experiments were carried out at the XPD beamline at Nation Synchrotron Light Source II (NSLS-II) using the rapid acquisition PDF method (RAPDF) [111]. A 2D Perkin Elmer amor-

phous silicon detector was placed 214 mm behind the samples, which were loaded in 1.0 mm ID Kapton capillaries. The incident wavelength of the x-rays was 0.1885 Å. Calibration of the experimental setup was done using fcc nickel powder as a calibrant. Datasets were collected at room temperature (~25 °C). Each diffraction image contains 600 frames, and each frame is exposed for 0.1 second.

The data were processed according to standard methods [112]. Image frames were averaged, a mask applied to remove the beamstop and hot and dead pixels. The averaged frames were then integrated along arcs of constant Q, where the Q value of each pixel was determined from the calibration after applying a polarization correction. This was done using the program PYFAI [113]. The data were normalized and corrected to obtain the total scattering structure function, $F(Q)$, which was Fourier transformed to obtain the PDF. This was done using PDFGETX3 [114] within XPDFSUITE [115]. The maximum range of data used in the Fourier transform was $Q_{\max}$ = 22.0 Å^{-1}. The structural modeling is carried out using DIFFPY-CMI [100].

Measured PDFs of the samples synthesized at different temperatures are shown in Figure 4.1. The curves are all very similar to each other, suggesting the samples formed in the same structural phase. However, the peak amplitudes are damped out more quickly in r for the samples synthesized at lower temperatures. The sample synthesized at 130 °C has a much smaller crystallite or particle size than those made at a higher temperature. This is also evident in the TEM images. Note that the TEM images reflect the physical size of the grains, whereas the extent of the PDF signal is a measure of the range of coherence of the nanoparticle structure, so in principle, they measure different quantities. However, we see a progression in both particle size and coherence with increasing synthesis temperature. Because the size of the nanoparticles (of order 10 nm) is somewhat larger than the range of the PDF (~ 0.6 - 0.7 Å), it is necessary to do model fitting to get a more quantitative measure of the exact crystallite size from the PDF. This will be discussed below, where we introduce our modeling workflow to test these qualitative hypotheses and obtain a quantitative understanding of the structure.

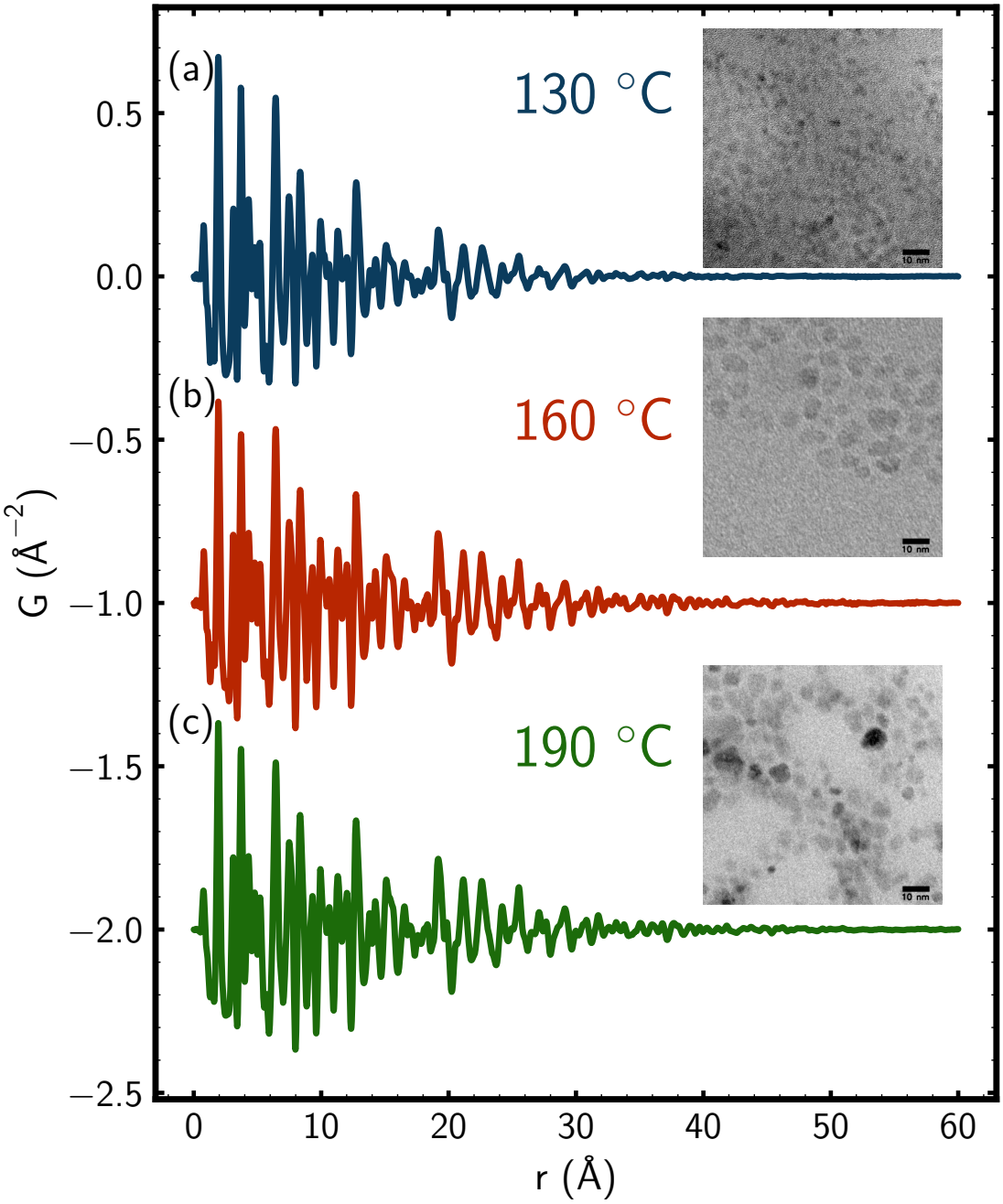

Figure 4.1: Measured PDFs from the TiO_2 samples synthesized at three different temperatures, (a) 130 °C, (b) 160 °C, (c) 190 °C, with TEM images of the respective samples shown in the insets. The PDFs have been normalized so that the difference between the maximum and minimum values is 1 Å^{-2}, plotted offset from each other for clarity.

4.3 Modeling workflow

We confined our models to the attenuated crystal model and our refinement algorithm to be the least square regression of the residuals. We present an overview of the workflow, which is described in more detail in the Results section.

1. **Search candidate phases** We search the structure database to find the most likely structural candidates for the major phase in each pattern using the PDFitc.org [116] website.

2. **Search major phases** We use the found structure to build an ACM. This could be done using PDFGUI [98], but in our case, we used the DIFFPY-CMI [100] to fit the PDF data and analyze the residuals for further optimization.

3. **Correct shape function** We replace the characteristic function with the one that can yield more accurate attenuation of the PDF. It gives us information on the shape and size of the nanoparticles.

4. **Search impurity phase** We add the additional phases in the model and search the most likely structures for the secondary phases. Although details of the structure of the second phase may not be our main interest, it is often necessary to include the secondary phase in the model to decrease the errors of the fitting parameters in the major phase.

5. **Add ligand PDF** We add the ligand phase in the model using an analytic function as its PDF. The reason to add it is similar to that of adding the impurity phase. At this step, we can achieve satisfying fitting results.

This workflow is universally applicable to all crystalline nanoparticles dominated by one phase but with other factors affecting the fit.

Table 4.2: Structure mining results. The "R_w" is the goodness of the fits. The "space group" is the space group of the structure. The "db" is the database code. The "db ID" is the ID of the structure in the database.

	R_w	space group	db	db ID
1	0.362457	C2/m	MPD	mp-554278[103]
2	0.797578	C2/m	COD	1528778[120]
3	0.845662	P1	MPD	mp-1245308[104]
4	0.872968	$I4_1$/amd	COD	7206075[121]
5	0.874363	$I4_1$/amd	COD	1526931[122]

4.4 Results

4.4.1 Approach to obtaining a good ACM fit to these nanoparticle samples

To illustrate the workflow, we take one representative dataset, T190L, and run it through the entire workflow to optimize the hyper-parameters in the modeling. We can then use what we have learned to analyze the other samples with similar PDFs.

To find a starting candidate structure for the PDF, we used the STRUCTUREMINING [117] app at the PDFitc website [116]. Given a PDF, it searches structures in databases such as the Crystallography Open Database [118] and Material Project Database [119] for matches to find the best-fitting candidate structures. It then returns a rank-ordered list of the best-fitting structures. It will also return the cif files themselves. In this case, the top five results returned by STRUCTUREMINING are listed in Table. 4.2.

The best candidate is the bronze phase of TiO_2 (space group C2/m) from the materials project database, a density functional theory energy minimized structure based on that in the inorganic crystal structure database [123]. In the second place, STRUCTUREMINING returns the same bronze structure from an entry in the COD. Surprisingly, despite being nominally the same structure, it is the second best in agreement, but the agreement R_w is much poorer than that returned from the Materials Project database. We looked into why this might be the case. We found that the returned structure had a significantly different b lattice parameter and slightly different fractional

coordinates despite being geometrically a very similar structure. We are not sure why this is the case. It may come from an error in the COD database for this entry. Interestingly, the known triclinic (space group P1) and the anatase (space group I4_1/amd) phases of TiO_2 also appear in this list, albeit with much worse R_ws. It may indicate one of these structures in the sample as an impurity phase. We return to this point later.

We used the best candidate structure from STRUCTUREMINING to refine the nanoparticle model to the data using DIFFPY-CMI [100]. The parameters refined were the scale factor, the lattice constants of the bronze phase, the atomic displacement parameters (ADPs), the symmetry-constrained positions of atoms, and the quadratic correlated motion correction parameter, δ_2. As a first approximation, we modeled the nanoparticle shape as spherical and refined the diameter of the spherical particles. The result is shown in Figure 4.2(a).

The model gave a good fit, showing that the model of TiO_2(bronze) spherical nanoparticles with a diameter of 45 Å is a reasonable approximation of the actual sample. However, the residual in Figure 4.2(a) is still significantly higher than that from a good fit to crystalline samples (circa 10%), suggesting that there may be something beyond our current model that we can learn from the data. It was also hinted at by the less highly performing STRUCTUREMINING analysis described earlier. We, therefore, sought improvements to the model to address this while avoiding over-fitting at the same time.

To find the nature of any impurity candidate phases, we took the difference curve and treated it as a signal, submitting it to the STRUCTUREMINING app. We present the result of this STRUCTUREMINING run in Table 4.3.

As expected, none of the phases in the list gives very good R_w values, since the signal was from a minority phase and distorted by more significant amounts of statistical noise than we are generally used to, and possibly an imperfect subtraction of the primary phase. However, the first ten candidate structures returned were all anatase. This gives us confidence that an anatase signal is present in the noise that STRUCTUREMINING was able to detect. Of course, we also know from

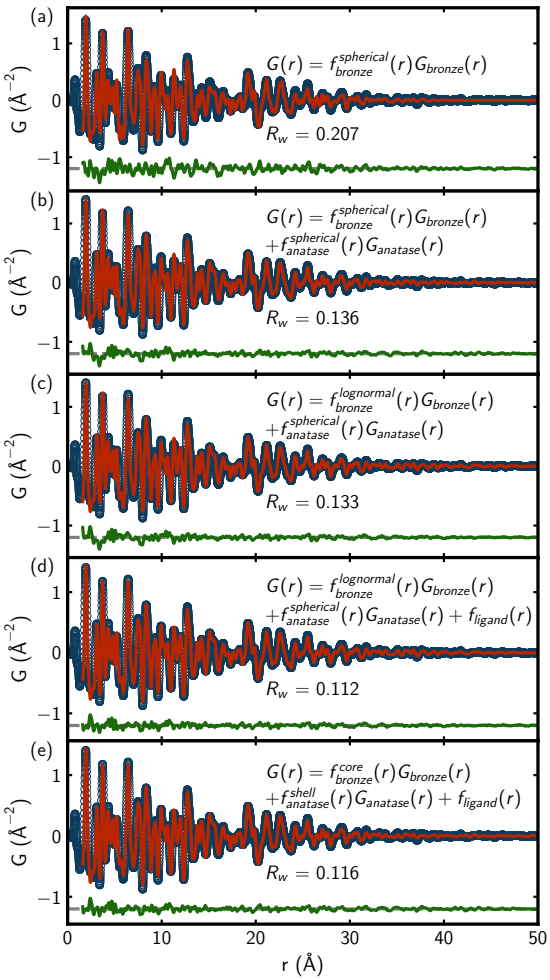

Figure 4.2: Calculated and measured PDFs of TiO_2. In each panel, the blue symbols are the measured PDF, and the red line is the PDF from the best-fit of each distinct model for the structure that is indicated by the label: (a) single bronze phase with a spherical shape, (b) single bronze phase in spherical shapes with a lognormal distribution of diameters, (c) segregated bronze and anatase phases, (d) segregated bronze and anatase phases with a sinusoidal signal accounting for the ligand signal, (e) bronze in the core of particles and anatase in the shell of the particles. The green lines offset below show the differences between the data and the model PDFs.

Table 4.3: The first 20 results from STRUCTUREMINING to the residuals from the single phase fitting, looking for a suggestion for the second phase.

	R_w	space group	db	db id
1	0.836536	$I4_1$/amd	COD	7206075[121]
2	0.836586	$I4_1$/amd	COD	1526931[122]
3	0.836725	$I4_1$/amd	COD	9008213[124]
4	0.836733	$I4_1$/amd	COD	9015929[125]
5	0.836767	$I4_1$/amd	COD	9008214[124]
6	0.836788	$I4_1$/amd	COD	9008215[124]
7	0.836831	$I4_1$/amd	COD	9008216[124]
8	0.837126	$I4_1$/amd	COD	9009086[126]
9	0.843697	$I4_1$/amd	MPD	mp-390[127]
10	0.844079	$I4_1$/amd	COD	1010942[128]
11	0.896091	C2/c	MPD	mp-34688[129]
12	0.911245	$I4_1$/amd	COD	1530151[130]
13	0.927118	Pbca	MPD	mp-1840[131]
14	0.930556	Pbca	COD	9004140[105]
15	0.942630	Pbca	COD	9004139[105]
16	0.952446	Pbca	COD	9004138[105]
17	0.953231	Pbca	COD	8104269[131]
18	0.956344	Pbca	COD	9009087[126]
19	0.959294	Pbca	COD	9004137[132]
20	0.965757	$P4_2$/mnm	COD	1532819[133]

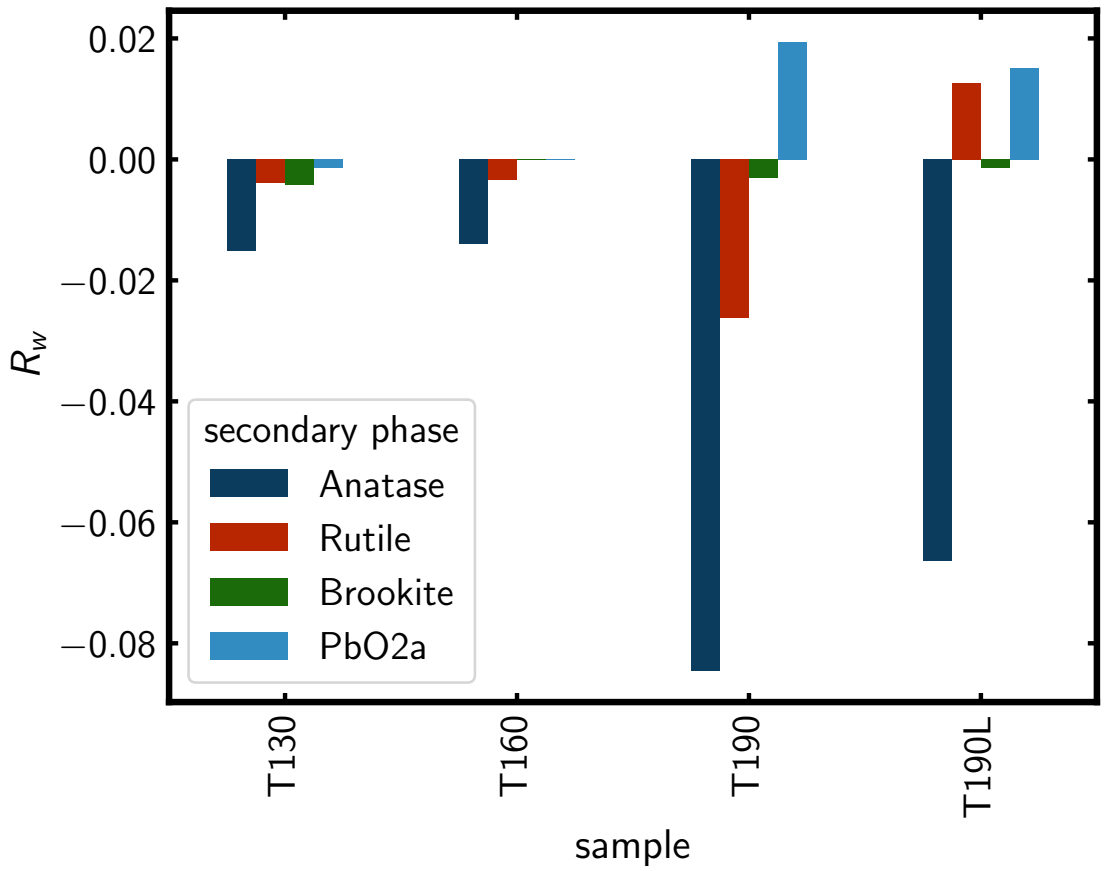

Figure 4.3: The changes in R_w after adding a second phase to the model. The secondary phase is listed in the legend, annotated with different colors. The bar shows the change of R_w compared with the single bronze phase fitting. The bars above zero mean an increase in R_w, and those below zero mean a decrease in R_w. The four groups of bars mean four samples in the test. Each sample is tested by four secondary phases. Thus, there are four bars.

chemical intuition and prior knowledge that anatase is a likely candidate for a second phase. Using the files provided by STRUCTUREMINING, we carried out a two-phase fit of the bronze phase and anatase. As an initial guess, we use the simplest model which is to assume that each phase exists in spherical nanoparticles. It does give a significant improvement in fit as evident in Figure 4.2(b). We also checked other possible secondary phases from the anatase, brookite, rutile, and the α-PbO_2 structure type for completeness. The anatase performed substantially better (Figure 4.3).

The fits are considerably better, but if we expand the plots of best-fit PDFs in the high-r region, we find that the ACM models of identical spherical particles do not handle the attenuation correctly. As shown in Figure 4.4(a), the pure spherical bronze phase model cannot fit the low-r

and high-r data well, and thus it damps too fast. Depicted in Figure 4.4(b), the two-phase model allows the signal to propagate out further, but some of the peaks lie in the wrong places.

Alternative models contain two or more size parameters, such as spheroidal particle shapes (different major and minor axis) or a distribution of particle sizes where we can model the mean radius but also allow for the distribution of diameters around the mean with some width. A commonly used distribution model for this is a lognormal distribution of particle sizes where the diameter distribution, X, is given by

$$X = e^{\mu+\sigma Z}, \tag{4.1}$$

where

$$\mu = \ln\left(\frac{\mu_X^2}{\sqrt{\mu_X^2 + \sigma_X^2}}\right), \tag{4.2}$$

$$\sigma^2 = \ln\left(1 + \frac{\sigma_X^2}{\mu_X^2}\right). \tag{4.3}$$

μ_X is the mean and σ_X^2 is the variance of X, respectively. Z follows the standard normal distribution. The refinable parameters in the model are μ_X and σ_X.

The fit resulted in an improved agreement in the high-r region, and a lower R_w, as evident by Figure 4.4(c) and (d). The lognormal distributed bronze phase model extends further into the high-r region, and adding the anatase phase further improves the fit. We also obtained a similar agreement with a spheroidal shape function, where the refinable parameters are the major and minor axes of the spheroid. Both of these characteristic functions are available in the DIFFPY-CMI [100] program.

Our current data could not differentiate between these two models, and we did not seek a more complicated model. A TEM image (Figure 4.1) of the sample shows that the particles are not uniform in size or shape, suggesting that both models are operating.

The model fit to the PDF signal gives a highly quantitative measure of the sample-average morphology of the coherent structural domains, complementing the TEM image, which is a direct

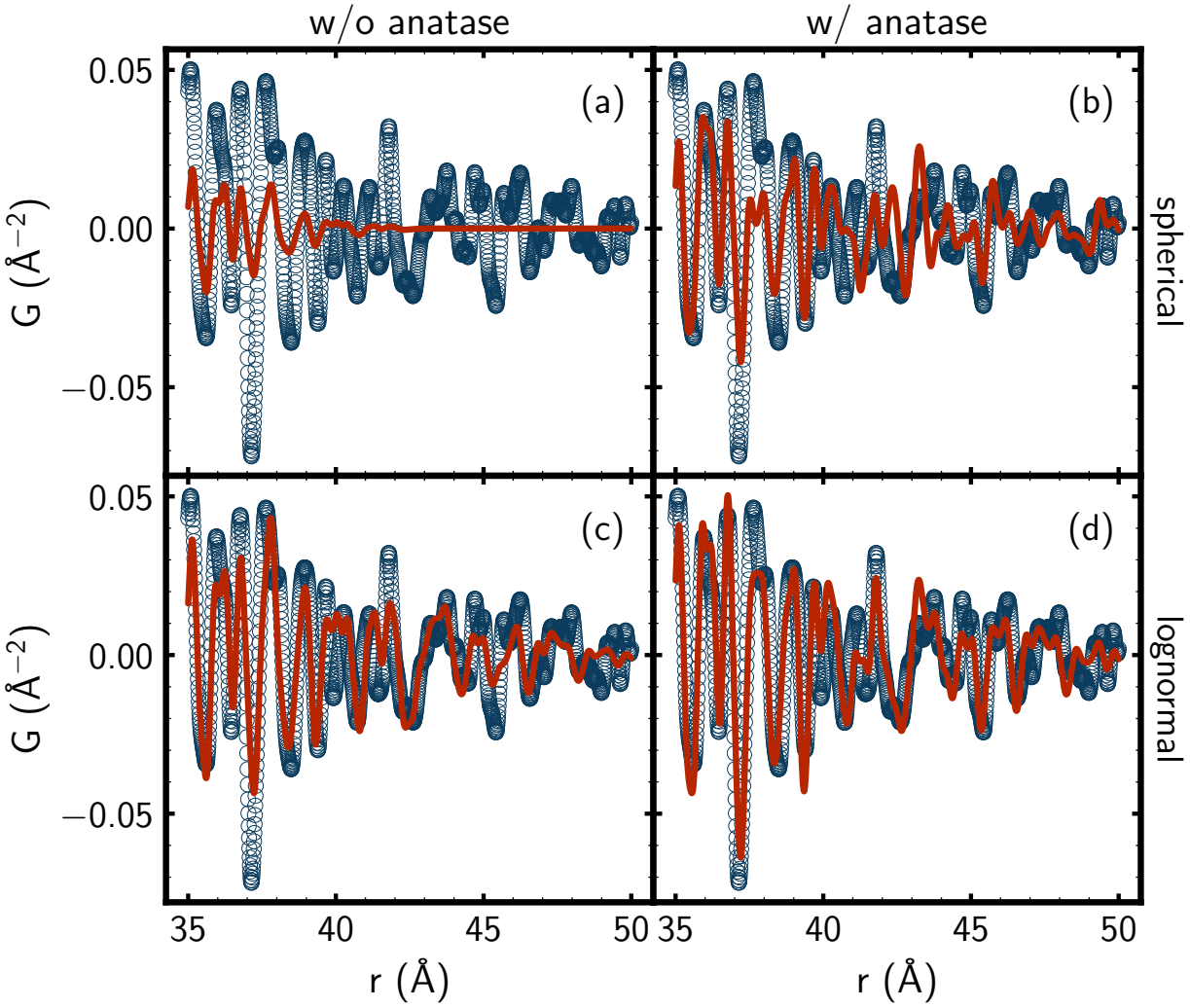

Figure 4.4: Data PDFs and PDFs from best fit models plotted over the range $35 \leq r \leq 50$ Å, which gives important information about the signal damping in models due to the particle shape and distribution. The blue circles are the measured PDFs from the T190L sample. The solid lines are the PDFs of (a) spherical bronze phase particles, (b) spherical bronze phase particles + spherical anatase particles, (c) lognormal distributed bronze phase particles, and (d) lognormal distributed bronze phase particles + spherical anatase particles.

image of a small part of the sample. It also measures a different quantity, the range of structural coherence (sometimes called crystallite size) of domains within the particles, where TEM is more sensitive to the physical size of the particles. As shown in Table 4.4, particle diameters obtained from PDF fitting tend to be smaller than those obtained from images of the particles in the TEM, which reflects the presence of multiple domains or the presence of structural disorder in the particles, possibly at the surface.

We used IMAGEJ [134] to paste oval/circular dots over the particles. The program calculates the surface area, from which we estimate the diameter as if all structures are circles. The residual (see the green curve in Figure 4.2(c)) is now sufficiently clear that we can look for finer-scale detailed information that may allow us to learn more about the sample. Careful inspection of the difference curve suggests that there may be a somewhat slowly varying damped sinusoidal variation in the signal, most evident in the low-r region, with a wavelength of around 5 Å. In the current context, this may originate from a highly disordered organic ligand in the sample that is not present in the model [135]. Since we are not so interested in the structure of the ligand in this study, we would like to account for this signal to improve the agreement of the calculated and measured PDF.

In practice, our experience is that it is unlikely that such a sinusoidal signal will affect the values of refined structural parameters, and this step may be skipped if it does not affect the scientific insights. However, to be sure, and by way of illustration, we show how it is done in DIFFPY-CMI [100] and also validate whether the assertion that it doesn't affect refined parameters is true. We use a simplified proxy model for the diffuse-in-r signal of a cosine function damped by a Gaussian given by Eq. 4.4,

$$G_{ligand}(r) = s \exp\left(-\frac{r^2}{2\sigma^2}\right) \cos\left(\frac{2\pi r}{\lambda} + \phi\right), \tag{4.4}$$

where s, σ, λ and ϕ are refinable parameters.

Using DIFFPY-CMI [100], we incorporated the equation into the model. The DIFFPY-CMI [100]

scripts are available at https://github.com/Billingegroup/19st_tio2b_notebooks. Adding the damped sine-wave proxy model results in a significantly improved fit, as shown in Figure 4.2(d), with $R_w = 0.112$. The values of the refined parameters are presented in Table 4.4. There is still some unaccounted-for residual, but the fit is now approaching the quality we expect from a well-ordered sample rather than the lower R_w values that have historically been considered acceptable from nanoparticle samples [136].

The refinement returned that there was 10% (mole-fraction) of the anatase phase and 90% of the bronze phase in the sample. Their contributions to the PDF are depicted in Figure 4.5(d). The refined values of the parameters for the best performing model shown in Figure 4.2(d) and Figure 4.5(c) are reproduced in Table 4.4 in the column labeled 190 °C L.

Table 4.4: Best fit values for parameters from the PDF refinements. We obtained the data in the "TEM-diameter (mean)" row using The columns for the synthesis temperature, and "L" indicates that the last sample has organic ligands while the others don't.

parameter	130°C	160°C	190°C	190°C L
	Bronze			
mole-fraction (%)	96.064	96.065	90.870	90.175
diameter mean (TEM) (Å)	17.215	26.202	28.142	28.784
diameter mean (PDF) (Å)	30	55	75	75
diameter std (PDF) (Å)	8.234	9.948	11.811	11.698
a (Å)	12.189	12.182	12.186	12.181
b (Å)	3.747	3.746	3.747	3.750
c (Å)	6.493	6.495	6.502	6.497
β (deg)	1.867	1.867	1.868	1.868
Biso(Ti0) (Å^2)	0.534	0.530	0.487	0.559
B$_{iso}$(Ti1) (Å^2)	0.610	0.488	0.468	0.444
B$_{iso}$(O2) (Å^2)	1.035	1.027	1.073	1.223

B_{iso}(O3) (Å^2)	2.499	2.178	1.899	1.991
B_{iso}(O4) (Å^2)	1.024	0.959	1.090	1.012
B_{iso}(O5) (Å^2)	2.195	1.755	1.770	1.622
x(Ti0)	0.100	0.101	0.101	0.101
x(Ti1)	0.197	0.196	0.196	0.196
x(O2)	0.060	0.060	0.059	0.060
x(O3)	0.136	0.138	0.135	0.134
x(O4)	0.133	0.135	0.134	0.135
x(O5)	0.231	0.236	0.236	0.237
z(Ti0)	0.706	0.706	0.707	0.707
z(Ti1)	0.288	0.286	0.286	0.286
z(O2)	0.366	0.363	0.363	0.365
z(O3)	0.020	0.016	0.012	0.014
z(O4)	0.711	0.714	0.711	0.712
z(O5)	0.341	0.348	0.350	0.354
δ_2 (Å^2)	1.902	2.139	1.604	2.546
	Anatase			
mole-fraction (%)	3.936	3.935	9.130	9.825
diameter (PDF) (Å)	53.741	53.856	61.074	59.074
a (Å)	3.784	3.786	3.785	3.785
c (Å)	9.525	9.497	9.501	9.499
B_{iso}(Ti) (Å^2)	0.725	0.502	0.494	0.595
B_{iso}(O) (Å^2)	1.653	1.290	1.302	1.502
z(O)	0.213	0.237	0.213	0.212
δ_2 (Å^2)	3.414	2.216	3.479	6.189

As discussed above, we do not expect that adding the ligand signal will significantly change the refined structural parameters. To test this in Table 4.5 we compare the values of best-fit parameters with and without the ligand signal removed.

Table 4.5: Comparison between the models with and without ligands. The first and second columns are refined parameters in the model without and with ligands, respectively. The last column is the difference between the second and first columns. To make the coordinates changes easy to comprehend, we multiply the fractional coordinates by lattice constants.

parameter	w/o ligand	w/ ligand	w - w/o
Bronze			
fraction (%)	91.621	90.175	-1.446
diameter mean (Å)	31.403	28.784	-2.619
diameter std (Å)	11.855	11.698	-0.157
a (Å)	12.186	12.181	-0.005
b (Å)	3.750	3.750	-0.001
c (Å)	6.490	6.497	0.007
β (deg)	1.868	1.868	-0.000
B_{iso}(Ti0) (Å^2)	0.522	0.559	0.037
B_{iso}(Ti1) (Å^2)	0.471	0.444	-0.027
B_{iso}(O2) (Å^2)	1.292	1.223	-0.069
B_{iso}(O3) (Å^2)	1.825	1.991	0.166
B_{iso}(O4) (Å^2)	1.133	1.012	-0.120
B_{iso}(O5) (Å^2)	1.417	1.622	0.205
x(Ti0) (Å)	1.234	1.231	-0.002
x(Ti1) (Å)	2.391	2.387	-0.003
x(O2) (Å)	0.759	0.737	-0.022
x(O3) (Å)	1.617	1.635	0.018
x(O4) (Å)	1.627	1.649	0.022

x(O5) (Å)	2.959	2.891	-0.069
z(Ti0) (Å)	4.587	4.592	0.005
z(Ti1) (Å)	1.860	1.861	0.001
z(O2) (Å)	2.358	2.373	0.015
z(O3) (Å)	0.072	0.091	0.019
z(O4) (Å)	4.610	4.627	0.017
z(O5) (Å)	2.320	2.297	-0.023
δ_2 (Å^2)	2.983	2.546	-0.437
Anatase			
fraction (%)	8.379	9.825	1.446
diameter mean (Å)	64.592	59.074	-5.518
a (Å)	3.786	3.785	-0.001
c (Å)	9.497	9.499	0.001
B$_{iso}$(O) (Å^2)	1.169	1.502	0.333
B$_{iso}$(Ti) (Å^2)	0.489	0.595	0.106
z(O) (Å)	2.019	2.011	-0.008
δ_2 (Å^2)	5.349	6.189	0.840
Ligand			
s	N/A	0.092	N/A
σ (Å)	N/A	7.020	N/A
λ (Å)	N/A	4.051	N/A
ϕ (rad)	N/A	-2.552	N/A

If the difference between the two sets of refined parameters is much less than the uncertainty on those refined parameters, we can say that removing the ligand signal doesn't affect our estimates of the refined parameters significantly. Unfortunately, there is currently no reliable way to estimate

the uncertainty of the parameters because of the unknown measurement errors (the experimental setup does not allow us to estimate random counting statistics reliably) and model imperfections (errors in the fit that come from things lacking in the model). The refinement code does report uncertainties on each parameter, but these cannot be trusted because of these reasons. We thus leave it up to the reader to assess if they consider the variability in the refined values with and without the ligand to be a concern.

The variability in refined lattice parameters and of the positions of the Ti ions in the unit cell are at the level of thousandths of an angstrom. They are at the level of hundredths of an angstrom for the oxygen positions. They can be as high as 10% for the B_{iso} values and the particle sizes. Actually, this variability probably reflects the level of uncertainty we have on those refined parameters, with less reliable parameters (B_{iso}s, diameters) having a higher variability than parameters we expect to be more reliable (lattice parameters and Ti positions).

The presence of the anatase impurity phase raises questions about how it is distributed in the sample. The result could be that a subset of nearly spherical nanoparticles is in the anatase phase. However, it could also be that all the nanoparticles consist of some regions in the bronze phase and others in the anatase phase, such as in a core-shell arrangement. The PDFs from these two scenarios will look similar as the PDF is most sensitive to the local structure (i.e., whether a region is locally bronze phase or locally anatase) rather than how those are arranged in space. Imaging techniques, such as TEM, might help here, but we can also do more with the PDF data by modeling the morphology of the nanoparticles using DIFFPY-CMI [100]. Here, we propose three hypotheses about the distribution of the anatase phase that could be tested:

1. There are separated bronze and anatase particles. They are close to identical spheres.
2. The bronze and anatase are in the same particles. Bronze is the core, and anatase is the shell.
3. There are separated bronze and anatase particles, but the sizes are not the same.

We used the corresponding characteristic functions for each of these cases. The fits are

shown in the Figure 4.5(a-c).

Compared with hypotheses (a) and (b), hypothesis (c) gave a better fit with the model capturing well the high-r region of the PDF. We cannot rule out anatase being at the surface of the bronze particles. For example, we didn't try a model of a log-normally distributed set of core-shell nanoparticles. We can say with certainty that anatase is present in the sample and that the anatase signal extends over similar ranges to the bronze signal.

The fits to the 190L sample are now satisfactory, and we can apply the same approach to studying the other samples.

4.4.2 Refining all samples with the same protocol

We used the same approach to study all the samples listed in Table 4.1. This resulted in good fits in all cases, as shown in Figure 4.6. The refined parameters are shown in Table 4.4.

We first consider the effect of synthesis temperature, T_{synth}, on the product. This varied between $130 < T_{\text{synth}} < 190\,°\text{C}$. Our modeling indicated aspects of the product such as phase composition (bronze vs. anatase), size and shape of the nanoparticles, and other structural parameters such as lattice parameters and ADPs. We will therefore consider these aspects for samples synthesized at different temperatures. All refined parameters can be seen in Table 4.4, and selected parameters are plotted in Figure 4.7. The synthesis temperature may influence the proportion of the nanoparticle's anatase and bronze phases. The amount of anatase in the sample is low (4%) for all samples synthesized up to 160 °C, but jumps to 9% for the 190 °C sample. This result is reproduced for the second 190 °C sample, which contains ligands (Figure 4.7(a)). It suggests an increased tendency for anatase formation with increasing temperature above 160 °C. The bronze phase is not the thermodynamically stable phase and is presumably kinetically trapped during the low-temperature synthesis [137]. Carrying out the synthesis at a higher temperature means there will be a stronger thermal driving force to get from the local kinetically trapped bronze into the anatase, which could explain this. A systematic study of how the transformation to anatase occurs

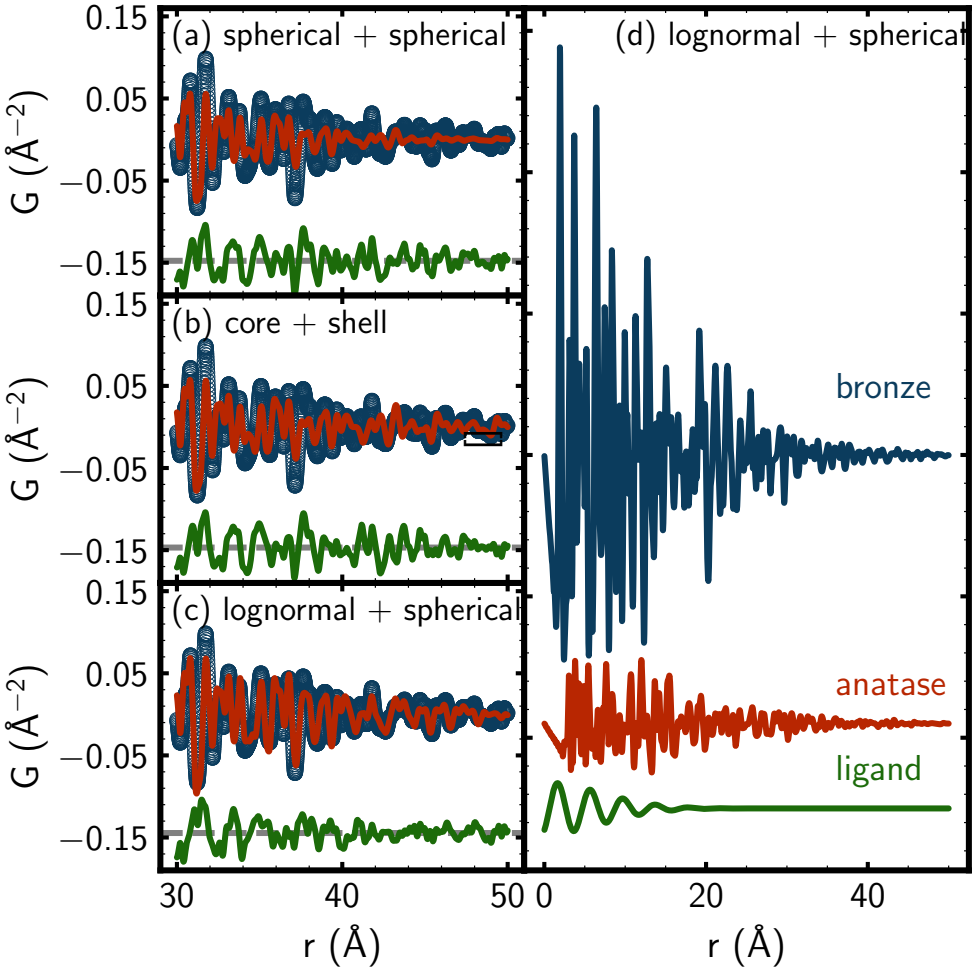

Figure 4.5: PDFs in the high-*r* region from the best fit models to the T190L measured data and different contributions. (a)-(c) PDFs in the high-*r* region from the best fit models to the T190L measured data. Open blue circles are the data, and the solid red lines are the model PDFs. The difference curve is shown offset below. The three fits are (a) spherical bronze phase nanoparticles and spherical anatase phase nanoparticles, (b) spherical core-shell nanoparticles with bronze structured cores and anatase on the surface, (c) a mixture of spherical bronze phase particles whose size is log-normally distributed and spherical anatase impurity phase particles. Different from Figure 4.4, these all include ligands in the model. (d) The different contributions to the fit shown in (c) are plotted separately.

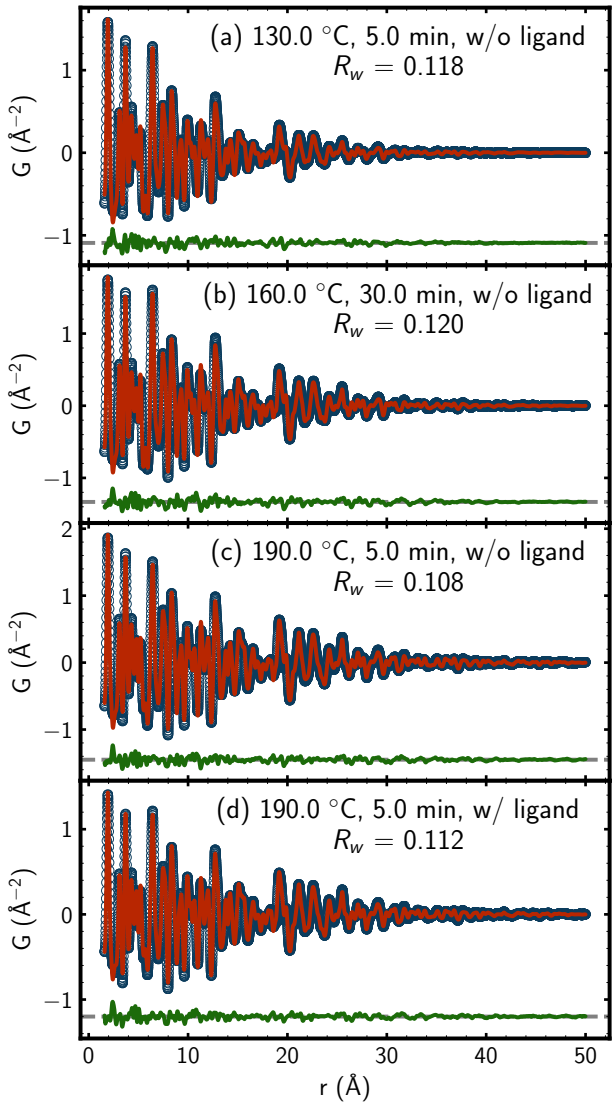

Figure 4.6: PDFs of the best fit models to the measured data for each sample. The blue circles are the measured PDFs, the red lines are the calculated PDFs from the best fits, and the green lines are the residuals. The samples are identified by synthesis temperature and reaction time in the figure panels. We also report the goodness of fit R_w.

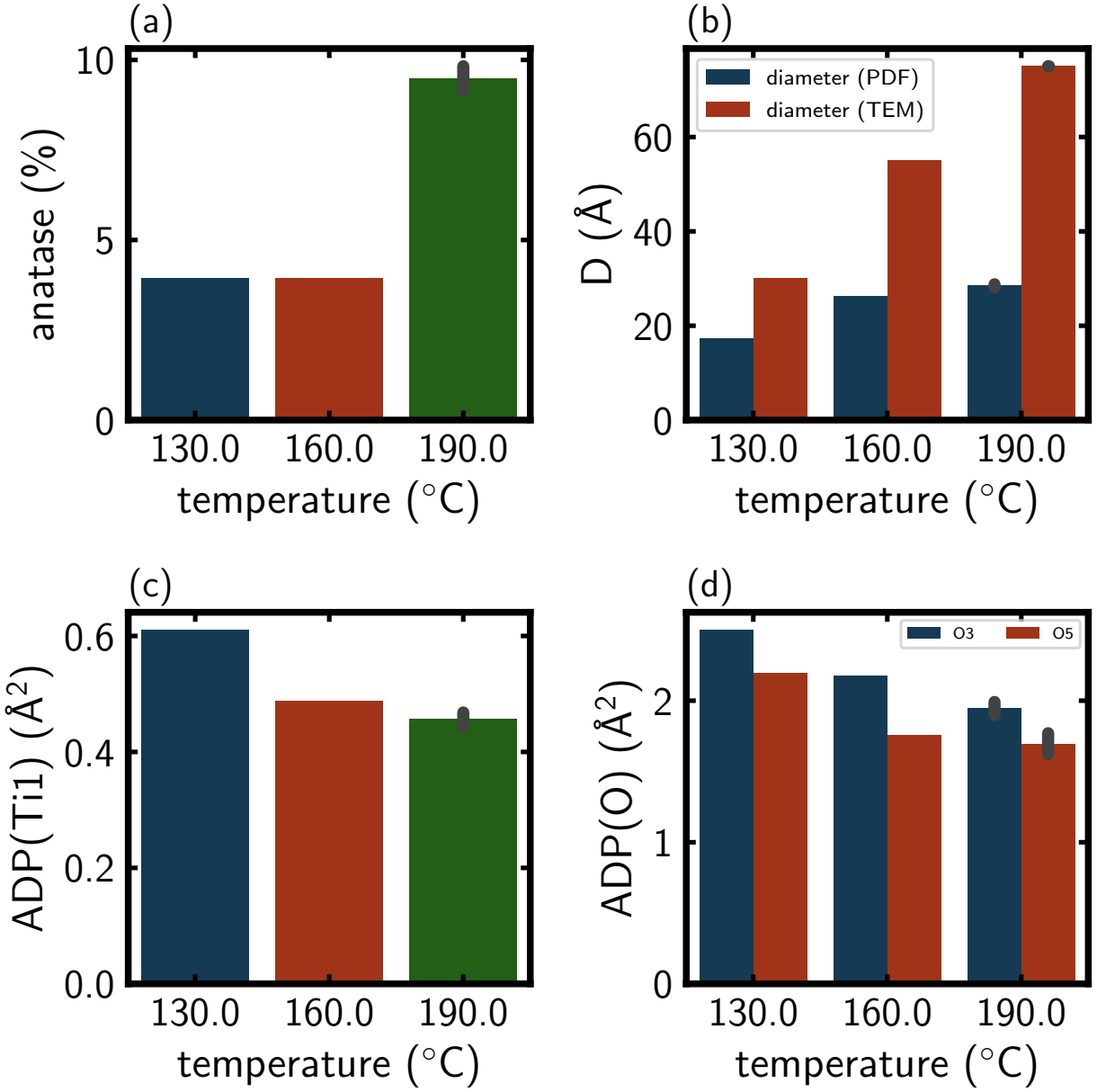

Figure 4.7: Best fit parameters for samples synthesized at different temperatures. (a) mole-fraction of anatase phase, (b) average diameter of bronze nanoparticles, (c) ADPs of Ti atom at position 1, (d) ADPs of O atoms at positions 3 and 5. The error bars for 190 ∘C show the deviations between the w/ ligand and w/o ligand samples.

as a function of temperature and synthesis time was not conducted, but this preliminary result suggests a temperature range where this process is beginning to occur on reasonable laboratory time scales.

We expect that the synthesis temperature also affects the size of the particles. Using the mean and the standard deviation of the lognormal distribution of the characteristic function from the PDF measurements and the particle size estimates from TEM, we see a steady increase in the size of the bronze-phase nanoparticle samples (Figure 4.7(b)), and an increase in the polydispersity, with increasing synthesis temperature. We also note a divergence between the nanoparticle size obtained from TEM and that obtained from the PDF, which suggests that for the higher synthesis temperatures, the nanoparticles are developing an internal domain structure. In general, we expect nanoparticle coarsening with increased temperature [138] due to the increased mobility of atoms at higher temperatures. There is a small increase in the diameters of the anatase particles also with temperature. We note that, at all temperatures, the minority anatase phase is more structurally coherent (the signal extends higher in r) than the bronze particles. The increase in this diameter with synthesis temperature is rather modest compared to that seen for the bronze phase. The findings about temperature-dependent morphology are essential for the application of TiO_2 nanoparticles in multiple applications, including phototoxicity [139], photoelectrode [140], and photocatalysis [141].

Oxygen vacancies have been reported in the anatase [142] and bronze [143] phases, and the synthesis temperature may affect the concentration of such vacancies in nanoparticles [144, 145, 146, 147]. In this case, we should find hints in the trends of lattice constants and ADPs with synthesis temperature because the oxygen vacancies will make the size of the lattice deviate from that of the perfect crystal and increase the uncertainty in the statistics of atom positions. Although we do not find any trends in the lattice parameters (Table 4.4), there is some indication that the O3 and O5 ADPs (and the Ti1 ADP) decrease with increasing synthesis temperature (Figure 4.7(c) and (d). This suggests an increase in atomic scale order and, therefore, possibly fewer point defects with

increasing synthesis temperature. In equilibrium, entropic arguments would suggest an increase in point defects at higher temperatures [146]. Our observation, therefore, suggests that synthesis at lower temperatures results in a metastable bronze phase that has an elevated number of defects. Synthesis at higher temperatures results in more thermal energy to heal the excess defects during the growth [146, 147].

4.5 Conclusions

The workflow works well for all TiO_2(Bronze). It reveals all synthesis conditions in the Table. 4.1 yield the nanoparticles in a major bronze phase and a minor anatase phase. The synthesis temperature may have an influence on the proportion of impurity phase in the nanoparticles and the size of the nanoparticles, but the structures all have similar lattice constant bronze phases synthesized. This fast and robust workflow is universally applicable for most metal oxide nanoparticles as long as there are hypothesized ACM models to use.

Chapter 5: Quantitative analysis of the nanoporous materials

I will demonstrate how I used the infrastructure to study the transitions in nanoporous materials. I selected some of my impactful discoveries and summarized them in the Table 5.1. In the following sections, I will introduce them individually.

5.1 Zirconium phosphate: the pathway from turbostratic disorder to crystallinity

The text, figures, and tables in this section are adapted from the thesis author's article [148]. Copyright 2019 ACS

I show how the structural order of nanocrystalline zirconium phosphates (ZrP) is tuned by synthetic methods and conditions through the use of synchrotron x-ray atomic pair distribution function analysis. With the different synthetic routes and different phosphoric acid concentrations in the synthesis, the product zirconium phosphates vary from turbostratically disordered nanoscale structures to fully ordered ones. I show that a change in the structural order leads to different ion-exchange properties.

Table 5.1: Summary of the transitions in nanoporous materials. "system" is the material system studied. "state 1" and "state 2" are the begin and end states in transitions. They are mutable because all transitions listed here are reversible. "Trigger"

system	state 1	state 2	trigger
zirconium phosphate	turbostratic	crystalline	*ex situ* temperature
Mn metal organic framework	glass	crystal	*in situ* temperature
Al metal organic framework	sql network	kgm network	polar solvent

5.1.1 Introduction

Tetravalent metal phosphates, zirconium phosphates, in particular, have been extensively studied because of their outstanding physical and chemical properties in both their amorphous and crystalline phases [149, 150, 151]. The first published studies of zirconium phosphates appeared in the mid-1950s, wherein they were investigated for their use as ion-exchange materials [152, 153]. They were typically studied as so-called amorphous materials until 1964, when Clearfield and Stynes made the first report of crystalline zirconium phosphates, α-ZrP, with the formula $Zr(HPO_4)_2{\cdot}H_2O$. Later, in 1978, the Alberti group reported the development of a related material, α-zirconium phosphonates [154], with the general formula $Zr(O_3PR)_2$, where R is an organic group.

After these first publications, efforts were then focused on the development of novel and unusual methods of synthesizing these materials. These studies have resulted in a variety of materials with wide degrees of crystallinity, crystallite size, and other material characteristics that extended the versatility of applications for zirconium phosphates and phosphonates [155, 156, 157].

Additional research efforts have mainly been focused on the study of different processes and methods to modify the physicochemical properties of the material surface after exfoliation. Some specific methods include adding suitable functional groups, covalently or electrostatically, to the surface [158, 159, 160, 161, 162], Recent research has mainly focused on developing methods of using these materials in applications such as ion exchange [163], catalysis [164, 165], polymer composites [166, 167, 168], drug delivery [169], nuclear waste remediation [170, 171], fire retardancy [172] lubrication [173, 174], proton conductivity [175, 176], and fuel cells [177] among other applications [178, 179].

Nevertheless, the structural difference between the amorphous and crystalline states of the metal IV phosphates and phosphonates and how they are related to the synthetic conditions are not well-known. Herein, I investigated the differences in structure due to different synthesis methods using pair distribution function (PDF) analysis of synchrotron powder x-ray diffraction data.

5.1.2 Method

Zirconyl chloride octahydrate ($\geq$ 90 %) was purchased from Advanced Materials. Phosphoric acid (wt 85 % H_3PO_4 in H_2O) was purchased from VWR. The 0.1 N sodium hydroxide NaOH standard solution was purchased from Acros, and sodium chloride from Aldrich. All chemicals were used without further purification. All material syntheses were performed in a fume hood using standard laboratory safety procedures and personal protective equipment.

An aqueous zirconyl chloride octahydrate solution (15 mL, 2.5 M) was added dropwise to 120 mL of a H_3PO_4 solution (1 mol, 2 mol, 4 mol, 5 mol, 6 mol, 7 mol, 8 mol and 14.7 mol) under vigorous stirring. For the sample dubbed ZP1S, the P/Zr molar ratio in the reaction mixture was 3.2:1; the theoretical ratio required for the synthesis was 2:1, and as such, the phosphate was present in excess. The resulting gel was then stirred for 5 min, and then the gel, alongside the remaining acid, was divided into five samples, each of which followed one of three different treatments or methods of synthesis: dubbed rotary stirring (S), hydrothermal (H), and reflux (R).

In the rotary stirring method, the formed gel and acid were poured into a 50 mL centrifuge tube and placed in a tube rotator at room temperature *sim*25 °C for 48 h. For the hydrothermal method, the formed gel and acid were poured into a Teflon pressure vessel and heated at temperatures of 90 °C, 145 °C and 200 °C for 48 h. For the reflux method, the gel and acid were poured into a flask that was kept in an oil bath at 90 °C, where it was refluxed for 48 h.

The products that were obtained by these processes were washed with deionized water several times until the wash solutions reached pH $\sim$ 3. The samples were then dried at 60 °C for 48 h. The samples are identified by ZP, referring to α-zirconium phosphate, followed by a number representing the molar concentration of the H_3PO_4 solution used, from 1 to 14, and then a letter that refers to the synthesis method, with S for rotary stirring, H for hydrothermal, and R for reflux. In the hydrothermal method, a number indicating the temperature is provided after the sample code, and the names of the samples are given in Table 5.2.

Table 5.2: Resume of α-ZrP Samples

sample name	H_3PO_4(mol)	method	temp (°C)	molar ratio P/Zr
ZP1S	1	S	25	3.2
ZP2S	2	S	25	6.4
ZP4S	4	S	25	12.8
ZP5S	5	S	25	16.0
ZP6S	6	S	25	19.2
ZP8S	8	S	25	25.6
ZP14S	14	S	25	44.8
ZP2H90	2	H	90	6.4
ZP2H145	2	H	145	6.4
ZP2H200	2	H	200	6.4
ZP8H90	8	H	90	25.6
ZP8H145	8	H	145	25.6
ZP8H200	8	H	200	25.6
ZP14H90	14	H	90	44.8
ZP14H145	14	H	145	44.8
ZP14H200	14	H	200	44.8
ZP2R	2	R	90	6.4
ZP8R	8	R	90	25.6
ZP14R	14	R	90	44.8

Synchrotron powder x-ray diffraction experiments were carried out at the XPD beamline (28-ID-2) at the NSLS-II synchrotron at Brookhaven National Laboratory using the rapid acquisition PDF method [111] during three beam times each for three sets of samples. The first set contained samples 2, 7, 8, and from 9 to 19, the second set contained samples 1, 3, and 4, and the third set contained sample 5. A 2D PerkinElmer amorphous silicon detector was placed 204 mm, 206 mm and 203 mm behind the samples, respectively. The samples were loaded into 1-mm-i.d. Kapton capillaries. The incident wavelengths of the Xrays were 0.1848 Å, 0.1875 Å and 0.1877 Å, respectively. Calibration of the experimental setup was done using nickel as a calibrant.

Data sets were collected at room temperature. The detector exposure time was 30 s. Raw data were summed and corrected for polarization effects before being integrated along arcs of constant scattering angle to produce 1D powder diffraction patterns using the program PYFAI [180]. Corrections were then made to the data and normalizations carried out to obtain the total scattering structure function, $F(Q)$, which was Fourier-transformed to obtain the PDF using PDFGETX3 [114] within XPDFSUITE [115]. The maximum range of data used in the Fourier transform was Q_{max} = 22.0 AA^{-1}.

I describe here the models that I used for the structural modeling. They were based on the α - ZrP crystal model [181] (Figure 5.1). It is a monoclinic crystal with atoms sitting in general positions in the lattice. The crystal is formed by stacking atomic layers. Each layer consists of zirconium atoms and phosphate anions. Water molecules are encapsulated between the layers.

Structure modeling was carried out using the program DIFFPY-CMI [100] and Q_{broad}. The parameters for the instrument resolution were obtained by fitting a nickel PDF for each experimental setup. For samples 1, 7 and 8 and 9 to 19, Q_{damp} = 0.0396 $\mathrm{Å}^{-1}$ and Q_{broad} = 0.0189 $\mathrm{Å}^{-1}$. For samples 2, 3 and 4, Q_{damp} = 0.0373 $\mathrm{Å}^{-1}$ and Q_{broad} = 0.0126 $\mathrm{Å}^{-1}$. For samples 5 and 6, Q_{damp} = 0.0409 $\mathrm{Å}^{-1}$ and Q_{broad} = 0.0176 $\mathrm{Å}^{-1}$.

The PDFs were first fitted by an attenuated-crystal (AC) model, where the model is constructed as a crystal using periodic boundary conditions, and the PDF is computed from this model

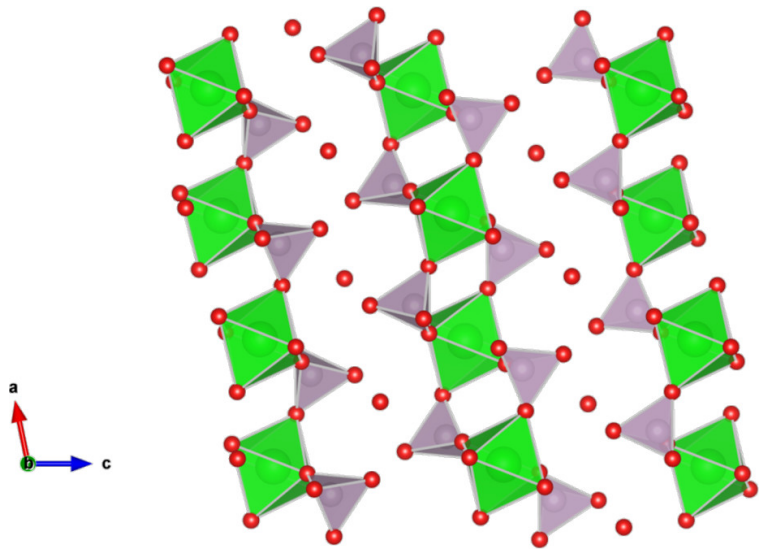

Figure 5.1: Schematic of the α-ZrP structure. Green spheres and octahedra represent zirconium, gray spheres and tetrahedra are phosphorus, and red spheres are oxygen. The disconnected oxygen atoms in α-ZrP are the intercalated water molecules.

but attenuated by a characteristic function to simulate the effect of the nanoscale crystallites. The misfit between the calculated and measured PDFs shows the possibility of the existence of deviations from the crystal structure, which I show is principally a turbostratic disorder in certain samples. Following Terban *et al*, for the disordered samples, a discrete slab model is used to simulate the completely turbostratically disordered structure [135]. The model is a single-finite-size covalently bonded slab extracted from the α-ZrP structure. Finally, a two-phase model is used in the program DIFFPY-CMI [100] to fit PDFs from all samples. One phase is the AC model, and the other phase is the discrete layer model. The initial values of the refinement parameters are set as the fitting results from individual models. This is a low-computational cost approximate model for simulating the coexistence of regions of material with more crystalline stacking of layers and more turbostratically disordered regions.

5.1.3 Result

To reveal the structures of the samples and investigate their dependency on the synthesis conditions, I analyzed PDF data from the synchrotron powder x-ray diffraction experiment. Figure 5.2 shows the measured PDFs of the S-series plotted offset from each other. In Figure 5.2(a), where the

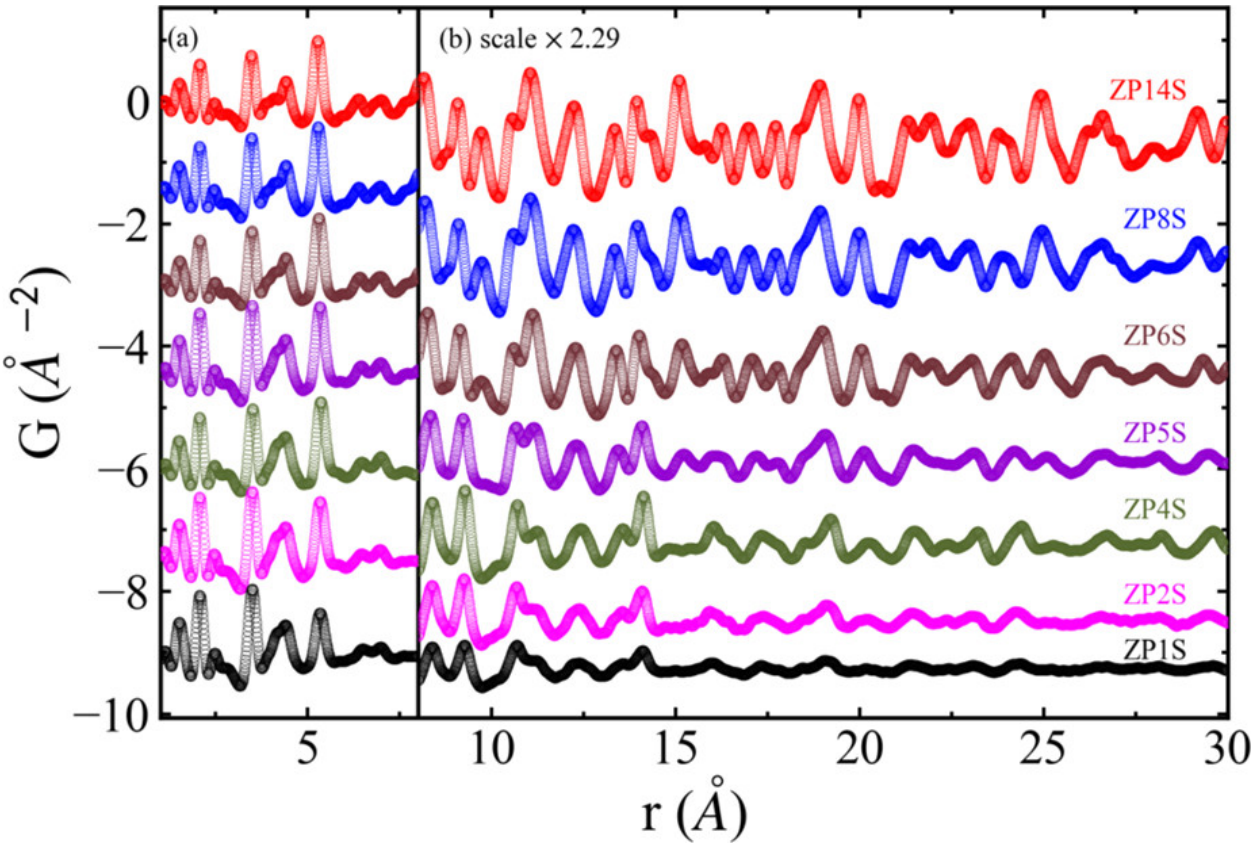

Figure 5.2: Experimental PDFs of the S-series samples: (a) low- *r* region of PDFs and (b) high-r region of PDFs, the scales of which are multiplied by 2.29.

low- r region of PDF is shown, all curves are similar, indicating that the local structures of all of the samples are the same. There are differences in the high- r region, as is evident in Figure 5.2(b). The intensity of PDF peaks in the high-r region is lower in the low-acid-concentration samples, suggesting a more disordered structure. They cross over to being more crystalline after the sample ZP4S, indicating that the structure of the product α-ZrP changes from a disordered state to a more ordered one when the acid concentration is between 5 mol and 6 mol.

This may be investigated in more detail by careful inspection of the PDFs of ZP1S-ZP5S versus ZP6S-ZP14S, which also show differences in the relative peak intensities, indicating that the structures are actually not the same between the disordered and ordered samples. For example, the PDF peak doublet at around 8 Å is higher on the right in ZP1S-ZP5S and higher on the left in ZP6S-ZP14S, and conversely, the doublet at around 11 A goes from being higher on the left in ZP1S-ZP4S to being higher on the right in ZP6S-ZP14S. The sample ZP5S appears to have intermediate behavior between these two cases, indicating that it may be between the ordered and disordered structures.

To investigate this further, I took linear combinations of the two end-member PDFs, from ZP1S and ZP14S, respectively, and fit them to the samples of intermediate acidity, varying the fraction of each PDF curve to get the best agreement with the measured PDF. The results are shown in Figure 5.3, which shows the proportion of crystalline component, Pc vs. molarity (M) of H_3PO_4 for the S-series samples.

The linear combination fits all of the PDFs between ZP1S and ZP14S, with the largest R_w of the fitting being less than 0.15. As the phosphorous acid concentration increases, the crystallinity gradually increases, with the intermediate PDFs being made up of a mixture of PDFs from well-ordered and disordered structures until a sharp crossover in the crystallinity occurs. This sharp crossover does suggest that there is a critical acid concentration necessary to achieve high crystallinity. However, it should still be noted that before, during, and after the inflection point, I still observe that the samples are well-described as a linear combination of the PDFs from end-point

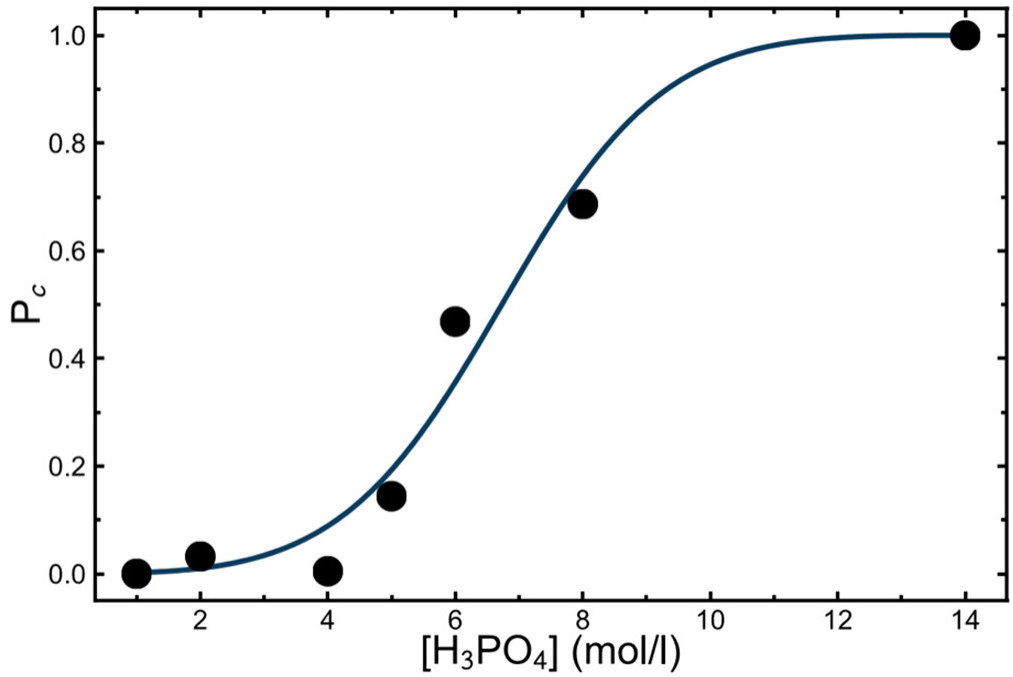

Figure 5.3: Proportion of the crystalline component, P_c versus the concentration of H_3PO_4 during synthesis. The line is added to show the general trend.

samples.

Having established that the measured PDFs from the S-series cross over between the end members of the series, I turned to the model to learn more about the actual structures. I first considered the attenuated crystal model based on the defect-free α-ZrP structure [181], as described in the Experimental Section. A representative fit is shown in Figure 5.4. It is clear that this model gives a reasonably good fit for the well-ordered samples made at higher phosphonic acid concentrations. This confirms that the well-crystallized samples are $\alpha-$ZrP. This observation has been made for all of the different synthetic methods, which allows us to conclude that the well-crystallized samples in the other two methods are α-zirconium phosphates. In contrast, the structure model does not fit the poorly crystalline material, except in the low-r region, where the crystalline and less crystalline samples have the same signals. To model these patterns, I opted to turn to a model that simulates turbostratically disordered layers. A discrete square slab of a single layer of the ZrP structure was generated.

The PDF was then fitted with a series of single-layer models of a series of sizes to obtain the

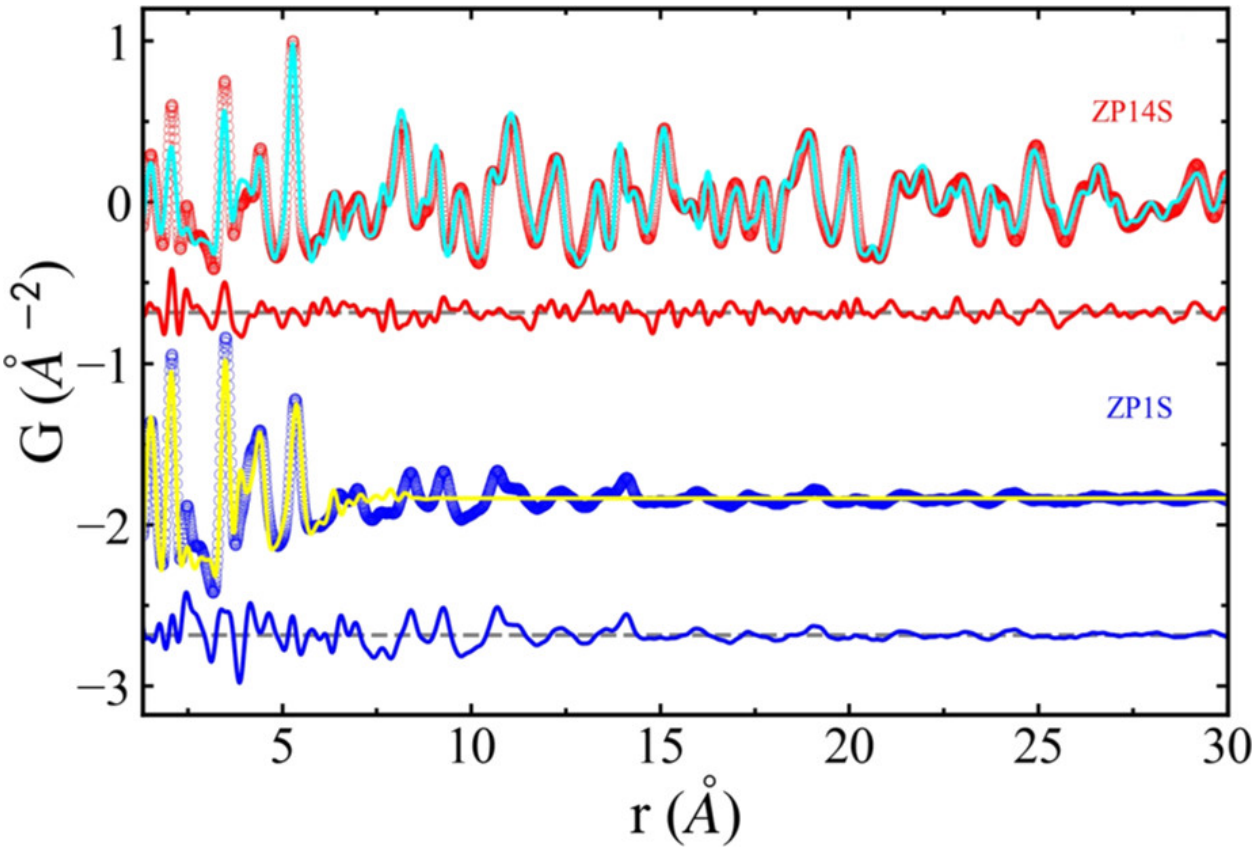

Figure 5.4: Representative fits of the attenuated α-ZrP model. The red and blue dots are experimental PDFs of ZP14S and ZP1S, the cyan and yellow lines are the calculated PDFs from the best fits, and the red and blue lines are differences between the experimental and calculated PDFs.

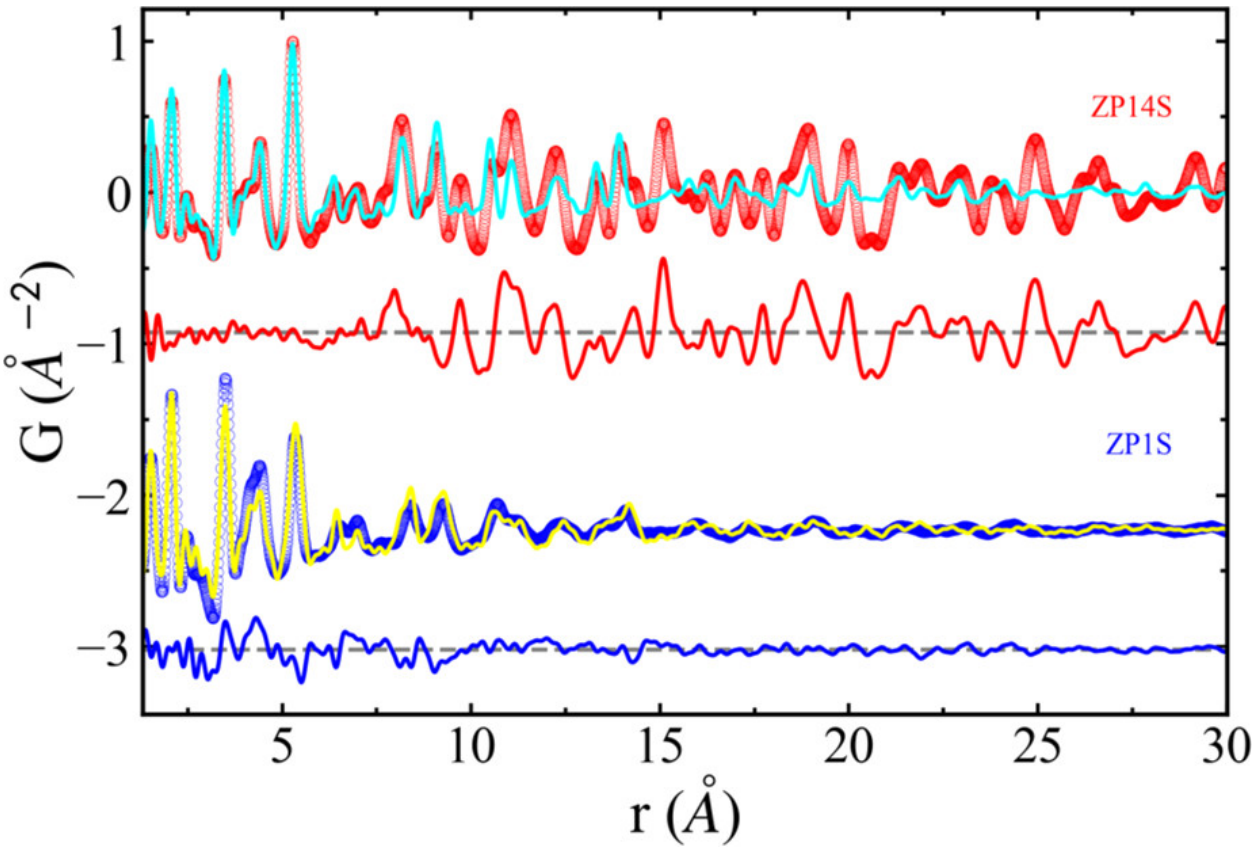

Figure 5.5: Representative fits of the single-layer model to (top) ZP14S and (bottom) ZP1S. The red and blue dots are experimental PDFs of ZP14S and ZP1S, the cyan and yellow lines are the calculated PDFs from the best model fitting to the data, and the red and blue lines plotted offset below the main curves show the difference between the experimental and calculated PDFs.

correct layer size. Representative fits are shown in Figure 5.5. In this model, the peaks in the high-r region of the model PDF line up with those in the measured PDF from the disordered sample, but this model yields a poor fit for the well-crystallized samples. I, therefore, concluded that the disordered samples consisted of turbostratically disordered layers of ZrP. Besides the endpoints, the samples are in a state between the totally turbostratically disordered structure and the well-ordered one. This state can be simulated by an equivalent model, which is a linear combination of PDFs from two phases. One phase is an attenuated bulk crystal, simulating crystallites with well-ordered layers, and the other phase is a discrete slab model, simulating a stack of turbostratically disordered phosphate layers.

The PDFs of the S-series are fitted to this two-phase model, with the fitting parameters being

the relative proportion of the two PDFs, lattice constants of the bulk model, length, width, and thickness of the single-layer model, atomic displacement parameters in both models, crystallite size in the bulk model, and δ (a parameter for correlated atomic motion) in the single layer model. As shown in Figure 5.6, all fitted PDFs are close to the experimental PDFs, and the residual differences do not show obvious patterns, indicating that this two-phase model describes the structures of nanocrystalline zirconium phosphates.

According to previous work reported by the Clearfield group for the amorphous, or turbostratic, $\alpha - ZrP$, during ion exchange, the cations are organized uniformly throughout its structure, forming a complete solid solution. There are no inflection points, and the pH rises continuously as $H^+$is replaced by Na^+. The solution composition varies along with the composition of the solid, with the pH of the solution being determined by the composition of the solid. [45,50] They attributed the lower capacity of the less crystalline α - ZrP to steric factors. [45] The data gathered here corroborate earlier pH titration data and show that the turbostratic samples do exhibit solid-solution-type behavior with a near-linear increase in the pH during titration. The PDF structural data show us that this behavior is likely due to the offset nature of the α-ZrP layers, which results in a disordered arrangement of the cations within the materials. This shift in the layer structure is also likely the cause of the lower ion capacity of the material because the offset α-ZrP layers should indeed produce a steric impediment to the ion layer through the offset phosphate groups (Scheme 2). With the turbostratically disordered α - ZrP, it appears that cation exchange takes place continuously along the pH range. It is likely that the first protons exchanged are not only on the surface but also in the larger cavities generated by the disordered layers. This explains the higher affinity of larger ions such as Cs^+in the turbostratically disordered α-ZrP than in the crystalline one. [49,51] This exchange further opens the layers and gives the sodium ions continuous access to the bulk of the material. This process of opening layers takes place at different pH or potential values because of their different orientations.

Figure 5.7 shows the refined crystallite size in the bulk model. In Figure 5.7, for the S-series,

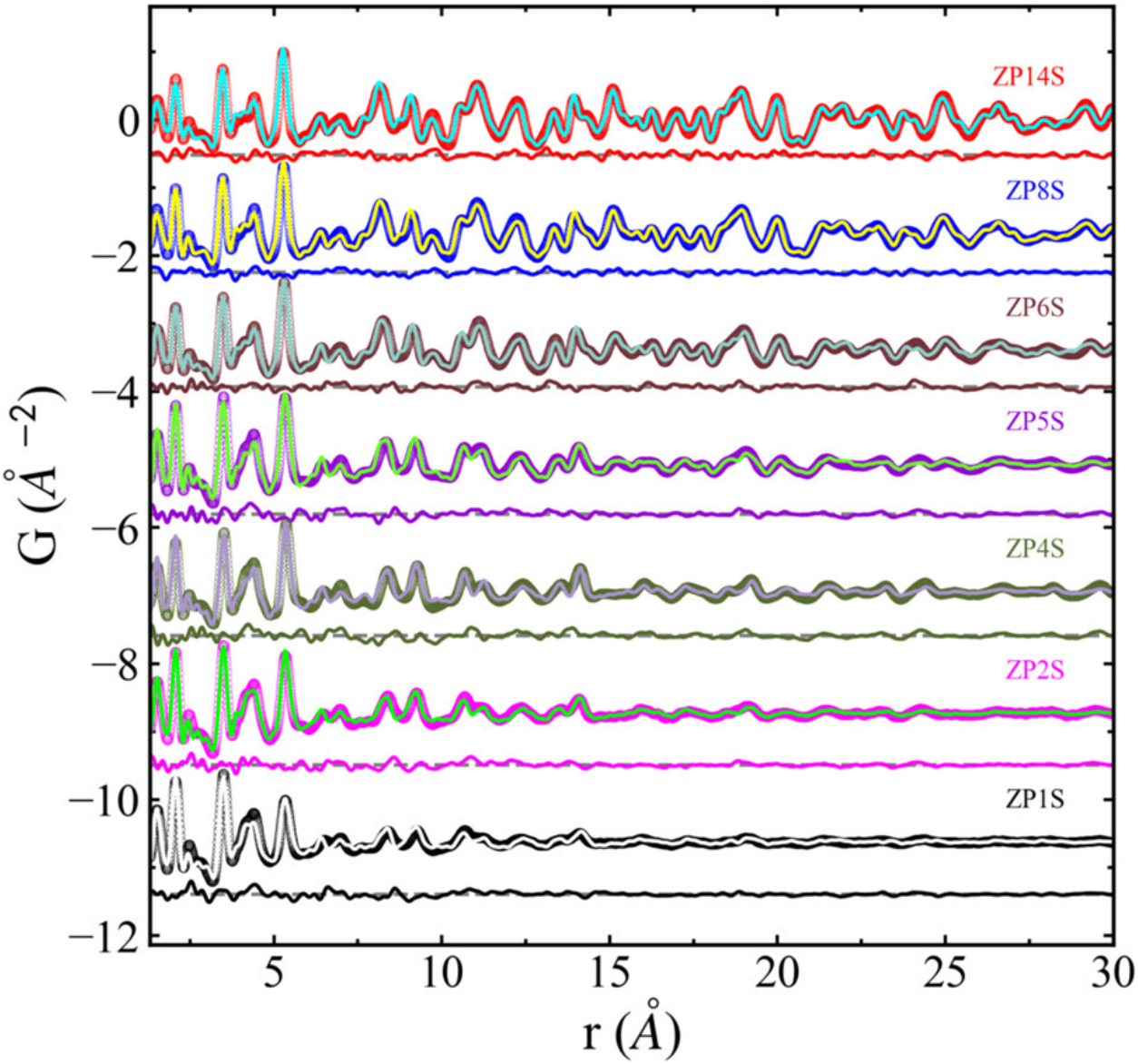

Figure 5.6: Experimental (dots) and fitted (lines) PDFs of the S-series samples with residual curves below.

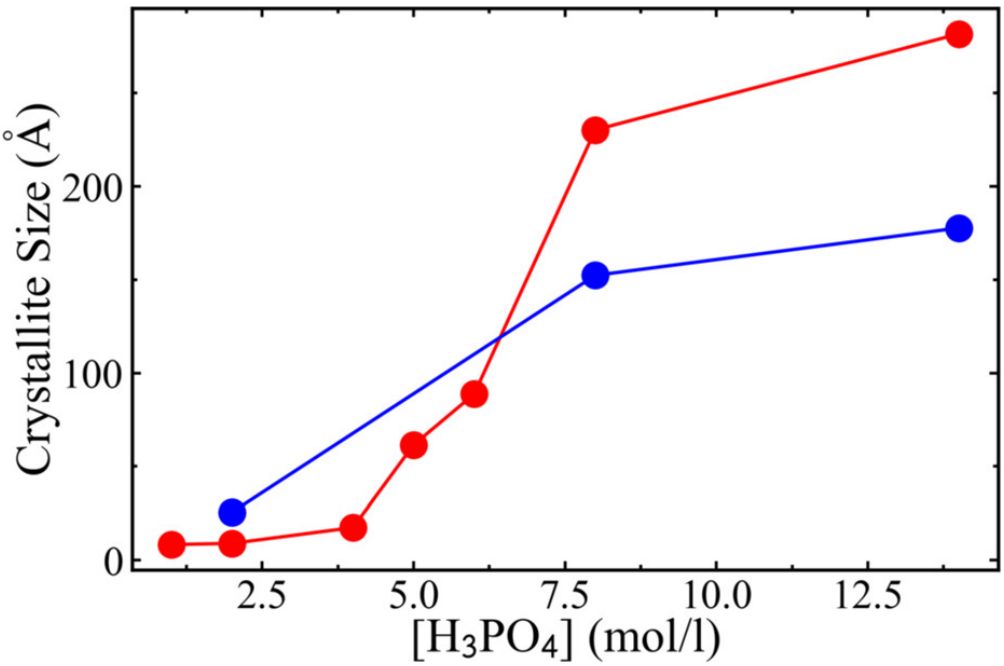

Figure 5.7: Refined crystallite size as a function of the H_3PO_4 concentration in the synthesis of stirring (red) and reflux (blue) methods.

the crystallite size increases with increasing H_3PO_4 concentration during the synthesis, quantitively indicating that higher H_3PO_4 concentration yields more crystalline samples. The R-series is fit with the two-phase model while the H-series is fitted by a single phase model because of the overall high degree of crystallinity. The fitted crystallite size of the R-series is shown in Figure 5.7. The sample is turbostratically disordered when synthesized at 2 MH_3PO_4 and crystalline when the H_3PO_4 concentration is larger than 8M.

On the other hand, the H_3PO_4 concentration dependence of the crystallite size in the H-series does not follow a monotonically increasing trend. As shown in Figure 5.8, at the same annealing temperature, the largest crystallite size is at H_3PO_4 = 8 M instead of 14M. Also, the variation of the crystallite size with increasing H_3PO_4 concentration is smaller than those in the S and R-series. The most crystalline sample in the H-series is produced under an acid concentration of 8M and an annealing temperature of 145°C, and the least crystalline sample is made at $2MH_3PO_4$ and an annealing temperature of 90°C.

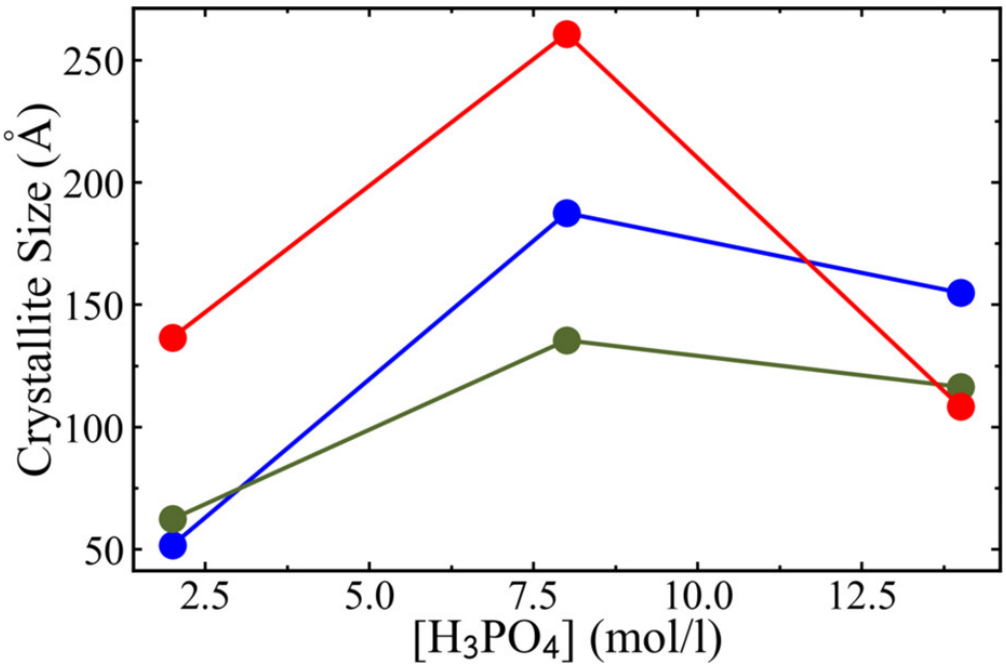

Figure 5.8: Refined crystallite size as a function of the H_3PO_4 concentration at an annealing temperature of 90 °C, 145 °C and 200 °C (blue, green, red) as a part of the hydrothermal method.

5.1.4 Conclusion

All of the products from synthesis are ZrP. However, PDF analysis has allowed us to resolve the structural differences of $\alpha - ZrP$ synthesized by stirring, hydrothermal, and reflux methods under a variety of different synthesis conditions. These results show that the products all consist of $\alpha - ZrP$ layers, where the layer order varies from completely turbostratically disordered to the presence of a 3D-ordered crystalline material. It quantitively confirms that as the concentration of H_3PO_4 used in the stirring and reflux syntheses increases, so too does the 3 d stacking order of the product α - ZrP. On the basis of these results, the main influencer of the structural order in $\alpha - ZrP$ is the acid concentration. The hydrothermal method shows that increasing H_3PO_4 concentration at the same annealing temperature results in small and nonmonotonic variation in the crystallinity. The fact that the α-ZrP samples consist of turbostratically disordered layers explains their hydration behavior; because of steric factors, some water molecules are trapped within the structure, requiring more thermal energy to leave the structure. The same steric factors explain the slope behavior of the sodium ion exchange in the less ordered $\alpha - ZrP$. The more disordered solid

solution behavior of the materials allows the cations to flow out more easily, with steric effects making the exchange more energetically favorable. This causes a steady increase in the pH during cation exchange because there is no additional enthalpic barrier preventing exchange like there is in the well-ordered α – ZrP samples.

5.2 Designing glass and crystalline phases of metal-bis(acetamide) s to promote high optical contrast

The text, figures, and tables in this section are adapted from the thesis author's article [182]. Copyright 2022 ACS

5.2.1 Introduction

Owing to their high tunability and predictable structures, metal-organic materials offer a powerful platform for studying glass formation and crystallization processes and to design glasses with unique properties. [183, 184, 185] Here, we report a novel series of glass-forming metal-ethylenebis(acetamide) networks that undergo reversible glass and crystallization transitions below 200 °C. The glass-transition temperatures, crystallization kinetics, and glass stability of these materials are readily tunable, either by synthetic modification or by liquid-phase blending, to form binary glasses. Pair distribution function (PDF) analysis reveals extended structural correlations in both single and binary metal-bis(acetamide) glasses and highlights the important role of metal-metal correlations during structural evolution across glass-crystal transitions. Notably, the glass and crystalline phases of a Co-ethylenebis(acetamide) binary network feature a large reflectivity contrast ratio of 4.8 that results from changes in the local coordination environment around Co centers. These results provide new insights into glass-crystal transitions in metal-organic materials and have exciting implications for optical switching, rewritable data storage, and functional glass ceramics.

5.2.2 Method

Total scattering experiments were carried out on single and binary $Mn(eba)_3[ZnCl_4]$ glasses at the 28-ID-2 line at NSLS-II at Brookhaven National Laboratory using the rapid acquisition PDF method (RAPDF) during the beamtime on May 16th - 18th, 2021 ($Mn(eba)_3[ZnCl_4]$) and October 1st - 2nd, 2021 ($Mn(eba)_3[MnCl_4]$ and 1-Mn/Co(Zn)). A 2D Perkin Elmer amorphous silicon detector was placed 225 mm behind the samples, which were loaded in 1.5 mm borosilicate capillaries. The incident wavelength of the x-rays was λ = 0.1892 Å. Calibration of the experimental setup was done using nickel as a calibrant. To prepare samples for total scattering experiments, $M(eba)_3[M'Cl_4]$ crystals were ground finely with a mortar and pestle under a N_2 atmosphere and then loaded into borosilicate glass capillaries (Charles Supper #15-BG; OD = 1.5 mm). Glassy samples were then obtained by heating the sample in a sand bath under a N_2 atmosphere to above the melting temperature of each compound and quickly transferred to a freezer (−35°C) to allow glass formation upon rapid quenching. For 1-Mn/Co(Zn) samples, $Mn(eba)_3[ZnCl_4]$ and $Co(eba)_3[ZnCl_4]$ were ground together, loaded into capillaries, and melt quenched into glassy samples as described above. Total scattering data of the crystalline state was collected for glassy samples that had been recrystallized by heating *in situ*. All capillaries were flame-sealed under a vacuum to avoid air exposure. Total scattering data of an empty 1.5 mm borosilicate capillary was collected to determine the background intensity, which was subtracted from the sample intensity during data processing. All samples remained glassy over the 5-7 days between preparation and measurement, as confirmed by the broad diffuse scattering peaks in the raw intensity data.

During the variable temperature experiments, the glassy samples were heated using a flowing nitrogen cryostream. $Mn(eba)_3[MnCl_4]$ and 1-Mn/Co(Zn) were heated from 25 °C to 190 °C and 205 °C of the cryostream set point, respectively, to ensure complete melting. The temperature ramp rate between measurements was 8 °C min^{-1}. To capture the structural evolution across the glasscrystal transition, x-ray scattering patterns were collected every 10°C in a time series after an

additional minute of isothermal holding to ensure temperature stabilization prior to each collection. $Mn(eba)_3[ZnCl_4]$ was heated from 25 °C to 117 °C, and x-ray scattering patterns were taken at each temperature. The exposure time was 60 s for each collection. Due to the small size of the cryostream, only a small portion of the capillary is in direct contact with the heat source, which is expected to lead to a temperature gradient within the sample and a sample temperature that is about 15 °C to 30 °C lower than the temperature setpoint of the cryostream depending on the exact temperature.

Raw data were summed and corrected for polarization effects before being integrated along arcs of constant angle to produce 1D powder diffraction patterns ($I(Q)$) using the PYFAI program [180]. Corrections for air and Compton scattering were then made to the data, and normalizations were carried out to obtain the total scattering reduced structure function, $F(Q)$, which was Fourier transformed to obtain the PDF (Figure 5.9) using PDFGETX3 [114] within XPDFSUITE [115]. The maximum range of data used in the Fourier transform ($Q_{\max}$), where $Q = 4\pi \sin\theta/\lambda$ is the magnitude of the momentum transfer on scattering) was 21.0 Å^{-1}.

5.2.3 Result

The PDFs of $M(eba)_3[MCl_4]$ networks provide insight into the structure of the disordered glassy states (Figure 5.10). At short interatomic distances (0 Å to 5 Å), the glass-phase PDFs are very similar to those of the crystalline phase, with sharp features that can be assigned to C−C, C−N, and C−O bonds within the eba ligands and to M−O and M′−Cl bonds, suggesting minimal changes to local coordination environments (Figure 5.11). This is consistent with ambient temperature x-ray absorption fine structure (EXAFS) data for glassy $Mn(eba)_3[MnCl_4]$, which can be well modeled with half of the Mn centers coordinated to 4 Cl atoms-consistent with the $[MnCl_4]^{2-}$ anion being preserved in the glassy state-and half of the Mn centers coordinated to 4.4(1.2) O atoms of the eba ligand. The average metal-ligand coordination number of 4.4(1.2) is comparable to that of the molten phase of $Co(bba)_3[CoCl]_4$ (N_{Co-O} = 4.8(7)) and is well above the bond percolation threshold of 2.0-2.4 that is required for a disordered network. This is consistent with the presence

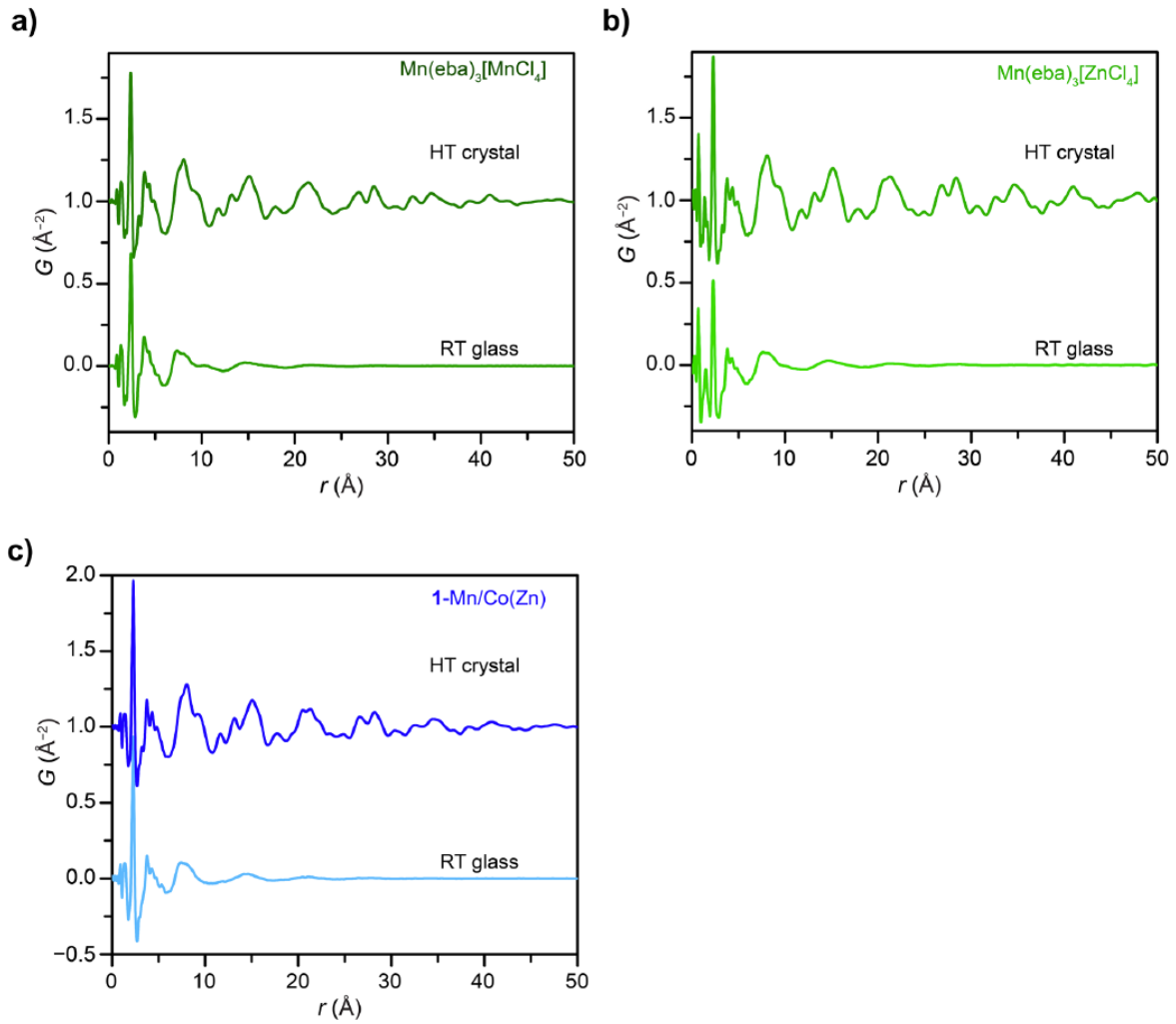

Figure 5.9: PDF of the room-temperature (RT) glassy state and high-temperature (HT) crystalline state for a) $Mn(eba)_3[MnCl_4]$; b) $Mn(eba)_3[ZnCl_4]$; and c) 1-Mn/Co(Zn).

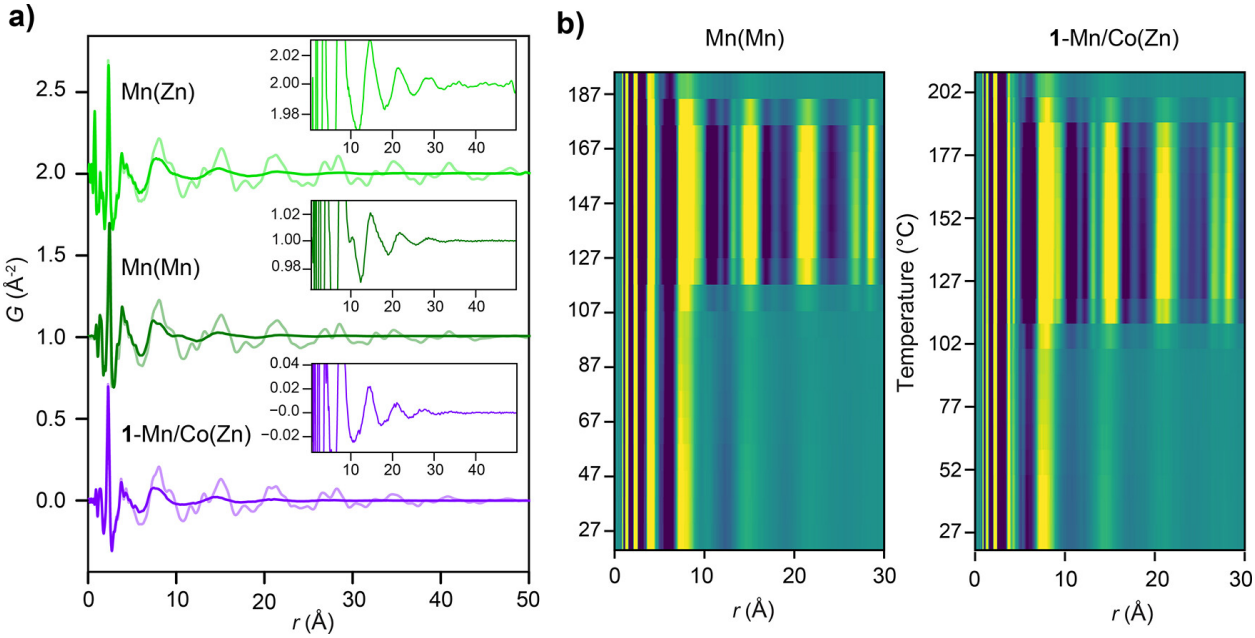

Figure 5.10: Glass transition of $Mn(eba)_3[ZnCl_4]$, $Mn(eba)_3[MnCl_4]$, and 1-Mn/Co(Zn). (a) Pair distribution function (PDF) of the ambient-temperature glass phase (dark traces) and high-temperature crystalline phase (light traces) of $Mn(eba)_3[ZnCl_4]$ (green), $Mn(eba)_3[MnCl_4]$ (olive), and 1-Mn/Co(Zn) (purple). An oscillatory signal indicative of extended-range ordering for each glass is shown in the insets. (b) Variable-temperature PDFs of $Mn(eba)_3[MnCl_4]$ (left) and 1-Mn/Co(Zn) (right) as the temperature is increased through a glass-crystal and then crystal-liquid transition.

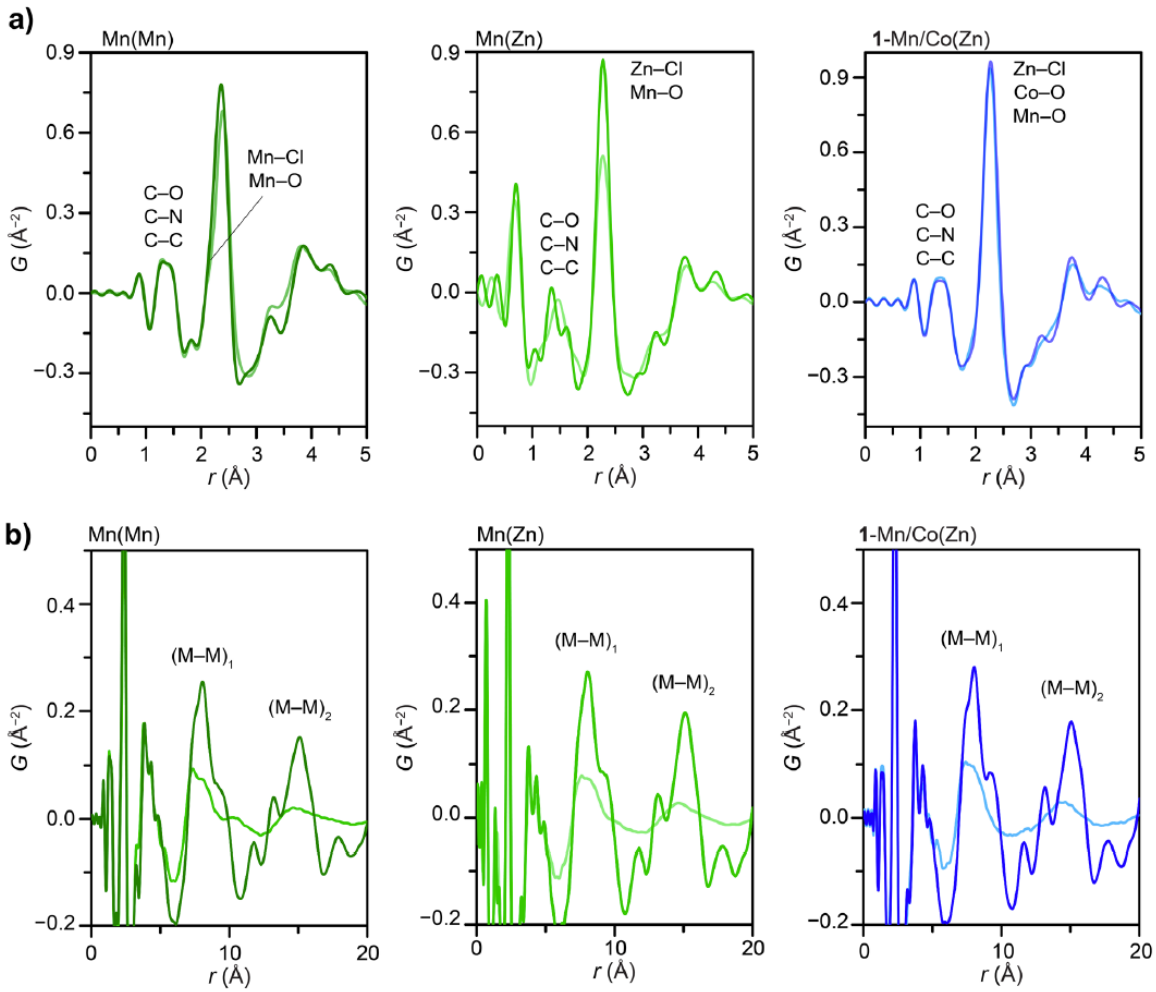

Figure 5.11: PDF comparisons of the high-temperature solid (dark solid line) and room-temperature glass (light solid line) phases of $Mn(eba)_3[MnCl_4]$, $Mn(eba)_3[ZnCl_4]$, and 1-Mn/Co(Zn) in 0 Å to 5 Å with important peak features assigned in a). In the range of 0 Å to 20 Å, correlations that are consistent with nearest neighboring ($(M\text{-}M)_1$) and second nearest neighboring ($(M\text{-}M)_2$) metal-metal distances in the crystal structure are indicated in b).

of an extended network of metal-ligand coordination interactions rather than discrete molecular units-that spans the entire glass.

The intermediate-r and high-r regions of the PDFs of $M(eba)_3[MCl_4]$ glasses further reveal structural ordering reminiscent of the parent crystalline phases. For instance, calculations of PDF patterns based on the crystalline phase show that peaks at 8.1 Å and 15.0 Å arise mostly from first- and second-nearest-neighbor correlations between framework and counteranion metal centers (M-M'), while peaks at 9.5 Å and 13.0 Å mainly arise from M-M and M-M' correlations. Though decreased in intensity in the glassy phases, broad peak features centered at 7.8 Å and 14.5 Å suggest structural correlations reminiscent of first- and second-nearest-neighbor metal-metal correlations in the crystalline state, albeit with a much wider distribution of metal-metal distances (Figure 5.12). In addition, a close examination of PDF patterns beyond 20 Å reveals an oscillatory signal that extends to 40 Å for all three $M(eba)_3[MCl_4]$ glasses (Figure 5.10(a) inset). This oscillatory signal can be attributed to density modulations that persist in the glassy state and produce a relatively sharp feature at low- Q in the diffraction signal known as the first sharp diffraction peak (FSDP) [186, 187]. The FSDP is a common feature of network-forming liquids and amorphous solids, and its position, Q_1, is correlated to the wavelength of the oscillatory signal, λ, as described by Eq. 5.1.

$$\lambda = 2\pi/Q_1 \tag{5.1}$$

The FSDP for glassy $M(eba)_3[MCl_4]$ is at 0.9 $Å^{-1}$ to 1.0 $Å^{-1}$, which corresponds to a density modulation wavelength of 6.3 Å to 7.0 Å that is consistent with density modulation characteristic of the crystalline network. This suggests that a network structure reminiscent of the parent crystalline phase is maintained within the glass. Interestingly, a larger amplitude of the oscillatory signal that extends to higher r is observed for $Mn(eba)_3[ZnCl_4]$ relative to $Mn(eba)_3[MnCl_4]$ and 1-Mn/Co(Zn) (Figure 5.10(a) inset; Figure 5.13). This implies that a higher degree of extended structural ordering is present in $Mn(eba)_3[ZnCl_4]$, which could contribute to its faster crystallization kinetics.

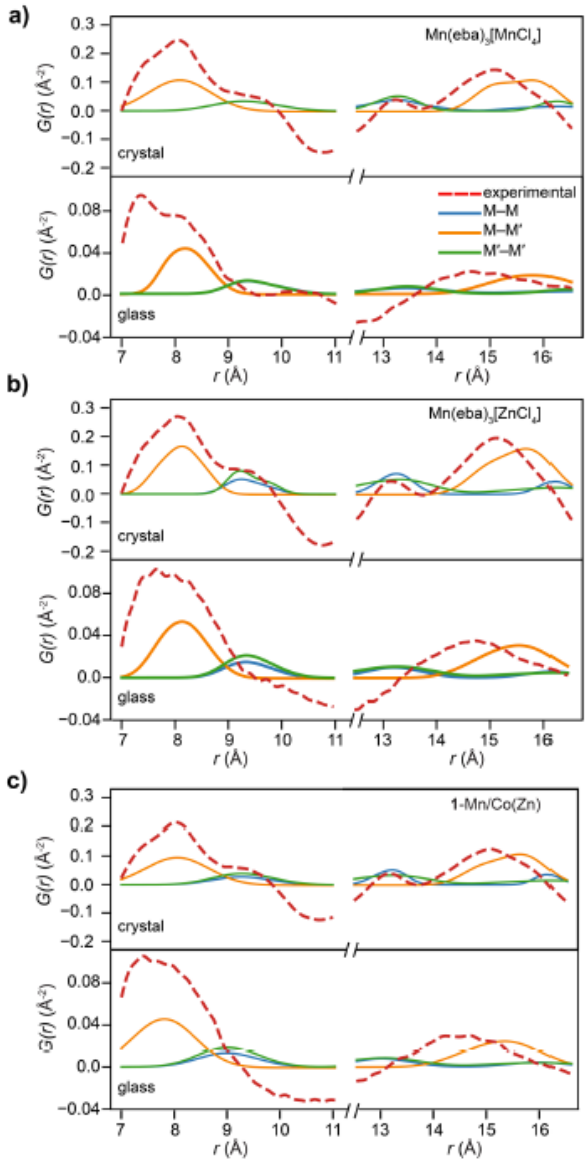

Figure 5.12: Partial PDF analyses for crystalline (top) and glassy (bottom) $Mn(eba)_3[MnCl_4]$ in (a), $Mn(eba)_3[ZnCl_4]$ in (b), and 1-Mn/Co(Zn) in (c) at 7 Å to 11 Å (left) and 12.5 Å and 16.5 Å (right). Red dotted lines represent experimentally and calculated M-M′, M-M, M′- M′ correlations and are shown as orange, blue, and solid green lines, respectively. Metal-metal correlations significantly contribute to the intermediate-range PDF features in both the crystalline and glassy states.

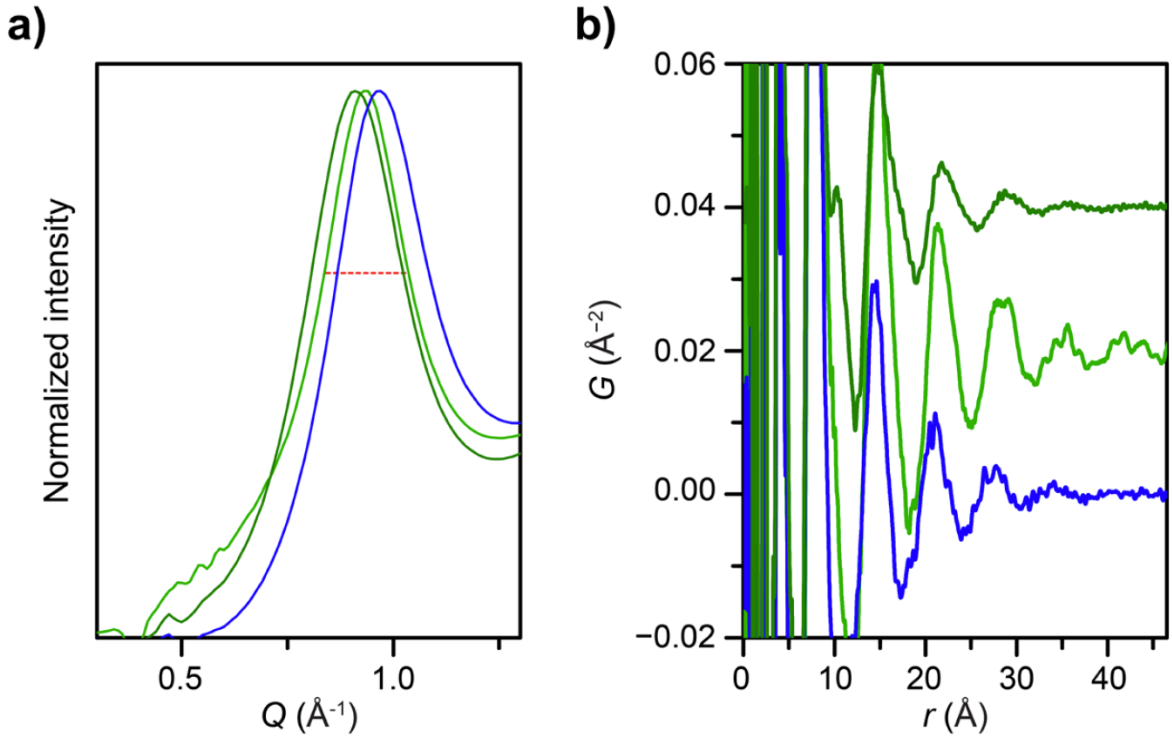

Figure 5.13: Comparison between $I(Q)$ and $G(r)$ of $Mn(eba)_3[MnCl_4]$, $Mn(eba)_3[ZnCl_4]$, 1-Mn/Co(Zn). and (a) Normalized $I(Q)$ (background subtracted) of room-temperature glasses in the range of 0.2 Å to 1.3 Å highlighting the first sharp diffraction peak (FSDP). (b) Expanded view of the PDF of room-temperature glasses in the range of $-0.02\,\text{Å}^{-2}$ to $0.06\,\text{Å}^{-2}$, highlighting the oscillatory signal indicative of extended-range ordering. Note that the PDFs of $Mn(eba)_3[ZnCl_4]$ and $Mn(eba)_3[MnCl_4]$ are offset by $0.02\,\text{Å}^{-2}$ and $0.04\,\text{Å}^{-2}$ from the PDF of 1-Mn/Co(Zn), respectively. In each plot, olive, light green, and blue solid lines corresponds to $Mn(eba)_3[MnCl_4]$, $Mn(eba)_3[ZnCl_4]$, 1-Mn/Co(Zn), respectively. $Mn(eba)_3[ZnCl_4]$ has the sharpest FSDP (as highlighted in the red dotted line), as well as the longest correlation length and oscillation amplitude in the extended range.

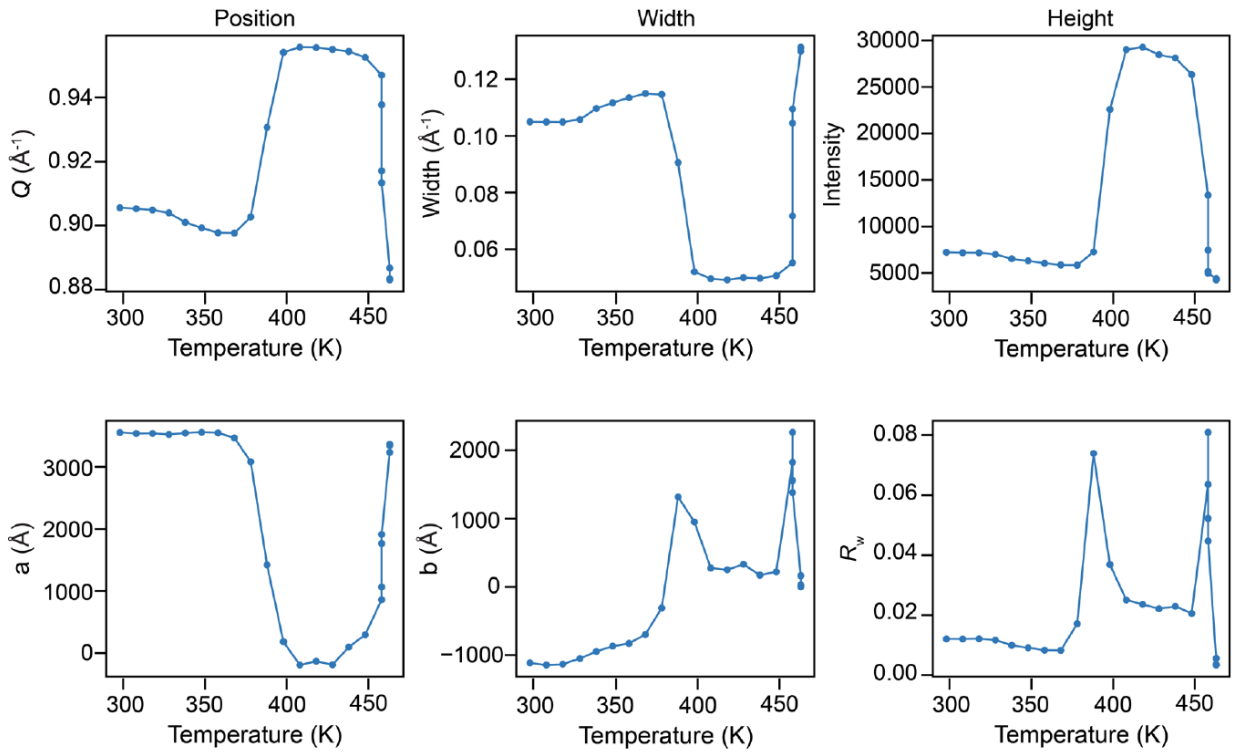

Figure 5.14: Variable-temperature FSDP fitting results of $Mn(eba)_3[MnCl_4]$ including its position, width, height, constants (a, b) for the linear baseline, and the goodness of fit (R_w). Glass-crystal and melting transitions occur upon heating, and the FSDP width decreases while the height increases drastically upon crystallization. Poor fits (high Rw value) are observed during the transition due to the coexistence of two phases.

While peaks at short interatomic distances remain largely unchanged upon heating each glass, changes to intermediate and long-range PDF features provide insight into structural evolution across the glass-crystal transitions. Arising from metal-metal correlations in the intermediate range, broad peaks centered at 7.8 Å and 14.5 Å significantly sharpen and increase in intensity as metal-metal distances unify during crystallization (Figure 5.10(b)). To quantitatively analyze how extended-range density modulations evolve upon heating, the position and width of the FSDP were modeled as a function of temperature for $Mn(eba)_3[MnCl_4]$ and 1-Mn/Co(Zn) (Figure 5.14 and Figure 5.15). As crystallization occurs in both compounds, the FSDP decreases in width and increases in intensity, consistent with increased structural order.

The position of the FSDP is 0.91 $Å^{-1}$ in the glass state of $Mn(eba)_3[MnCl_4]$, while the first

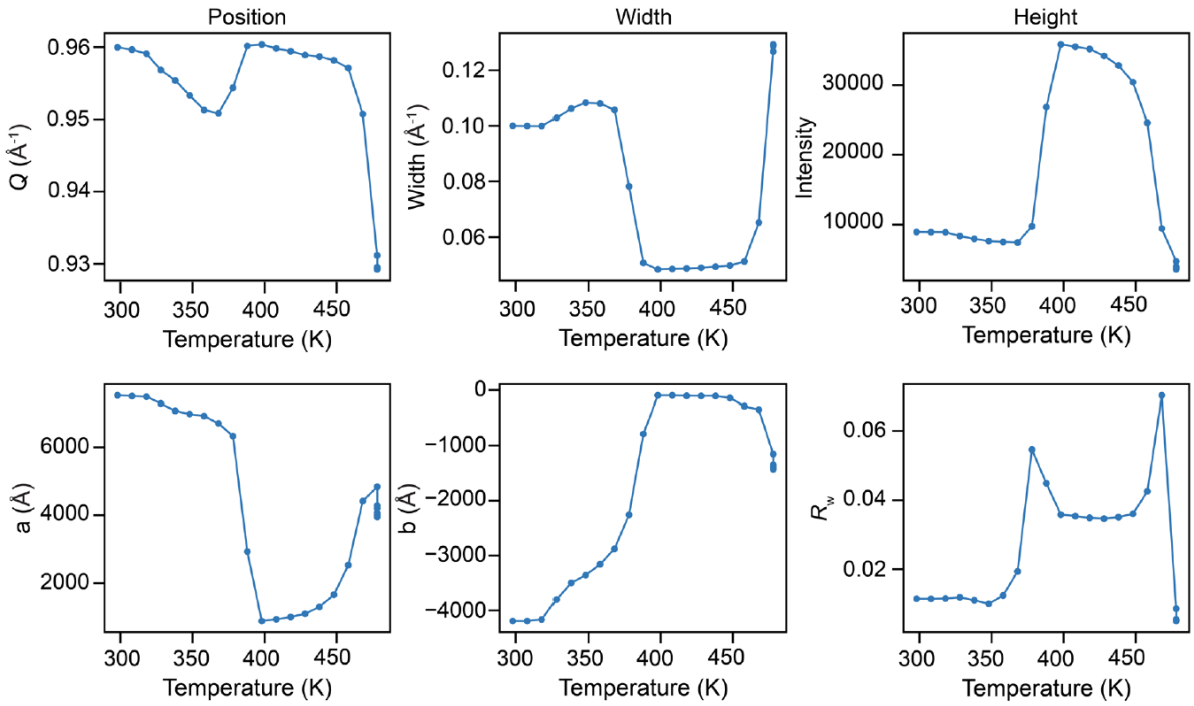

Figure 5.15: Variable-temperature FSDP fitting results of 1-Mn/Co(Zn) including its position, width, height, constants (a, b) for the linear baseline, and the goodness of fit (R_w). Glass-crystal and melting transitions occur upon heating, and the FSDP width decreases while the height increases drastically upon crystallization. Poor fits (high R_w value) are observed during the transition due to the coexistence of two phases.

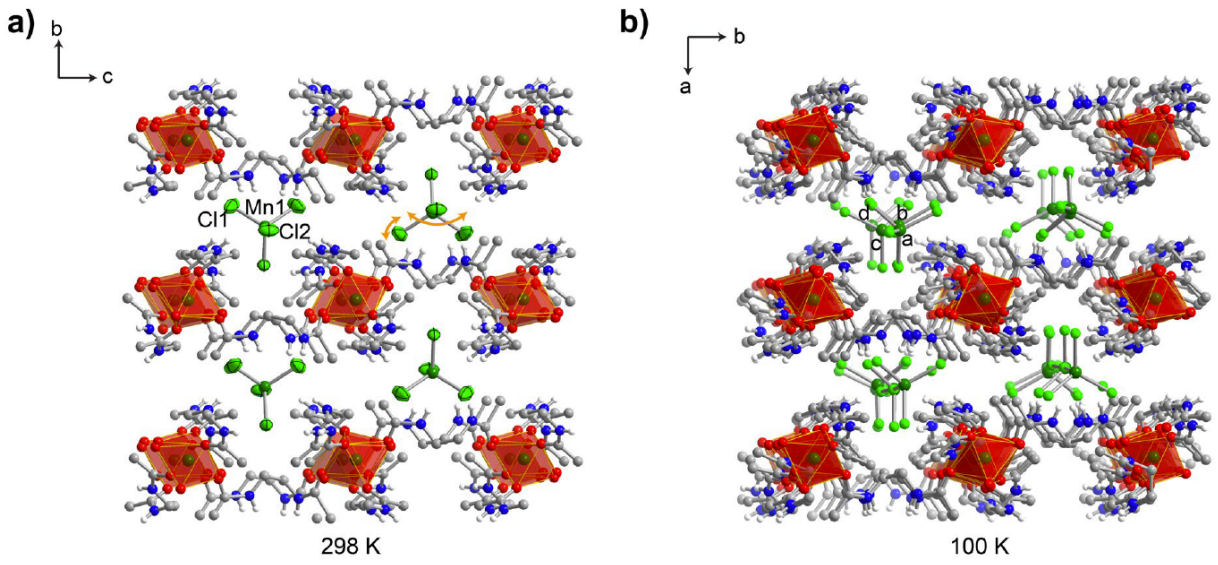

Figure 5.16: Crystal structure of $Mn(eba)_3[MnCl_4]$ at a) 298 K and b) 100 K with their respective lattice directions indicated. Olive, green, red, blue, grey, and white spheres represent Mn, Cl, O, N, C, and H atoms, respectively, and only N-H protons are shown for clarity. Mn1, Cl1, and Cl2 and corresponding Mn1 a-d, Cl1 a-d, and Cl2 a-d for the atomic position analysis are labeled in the 298 K and 100 K structures correspondingly.

intense Bragg peak appears at a higher Q of 0.95 $Å^{-1}$ in the crystalline state, which suggests a contraction in real-space density modulations during crystallization. Surprisingly, He pycnometry shows that the density of the $Mn(eba)_3[MnCl_4]$ glass is actually 3.0 % higher than that of the crystal. We hypothesize that the slight increase in the glassy state density is mainly driven by a reduction in tiny void spaces between ordered layers in the glass relative to the crystalline state, which is not captured in the FSDP since it only reports on weakly ordered density modulations. This is consistent with the dynamic disorder observed for $[MCl_4]^{2-}$ anions (Figure 5.16), which could reflect voids in between the coordination network layers that are eliminated in the glassy state and regained upon the glass-crystal transition. Although not commonly observed for conventional glasses, we note that there are several examples of metal-organic frameworks that form glasses that are denser than the parent crystalline phase due to reduced residual void space. [188]

5.2.4 Conclusion

The foregoing results demonstrate a strategy to increase the glass-transition temperatures of metal-bis(acetamide) previously reported metal-bis(acetamide) networks can be attributed to a reduced entropy of fusion and increased molten-phase viscosity that results from the reduced conformational flexibility of ethylenebis(acetamide) in comparison to longer bridging ligands. Moreover, most $M(eba)_3[MCl_4]$ compounds undergo reversible glass-crystal transitions, and the glass stability can be enhanced by modifying the nature of the metal center in the counteranion site or by liquid-phase blending of two $M(eba)_3[MCl_4]$ networks. The highly reversible interconversion between glassy and crystalline phases, well as the capacity for forming homogeneous binary glasses upon liquid-phase mixing, were leveraged to design a new optical phase-change material with a high reflectivity contrast ratio of 4.8. Owing to their high tunability, metal bis(acetamide) networks offer a promising platform for expanding the structural and chemical diversity of metal-organic glasses with predictable thermophysical properties unobserved in conventional glassy materials.

5.3 Rapid desolvation-triggered domino lattice rearrangement in a metal-organic framework

The text, figures, and tables in this section are adapted from the thesis author's article [189]. Copyright 2019 Nature Portfolio

5.3.1 Introduction

Topological transitions between considerably different phases typically require harsh conditions to collectively break chemical bonds and overcome the stress caused to the original structure by altering its correlated bond environment. [190, 191, 192] This section presents a case system that can achieve rapid rearrangement of the whole lattice of a metal-organic framework through a domino alteration of the bond connectivity under mild conditions (Figure 5.17). The system transforms from a disordered metal-organic framework with low porosity to a highly porous and

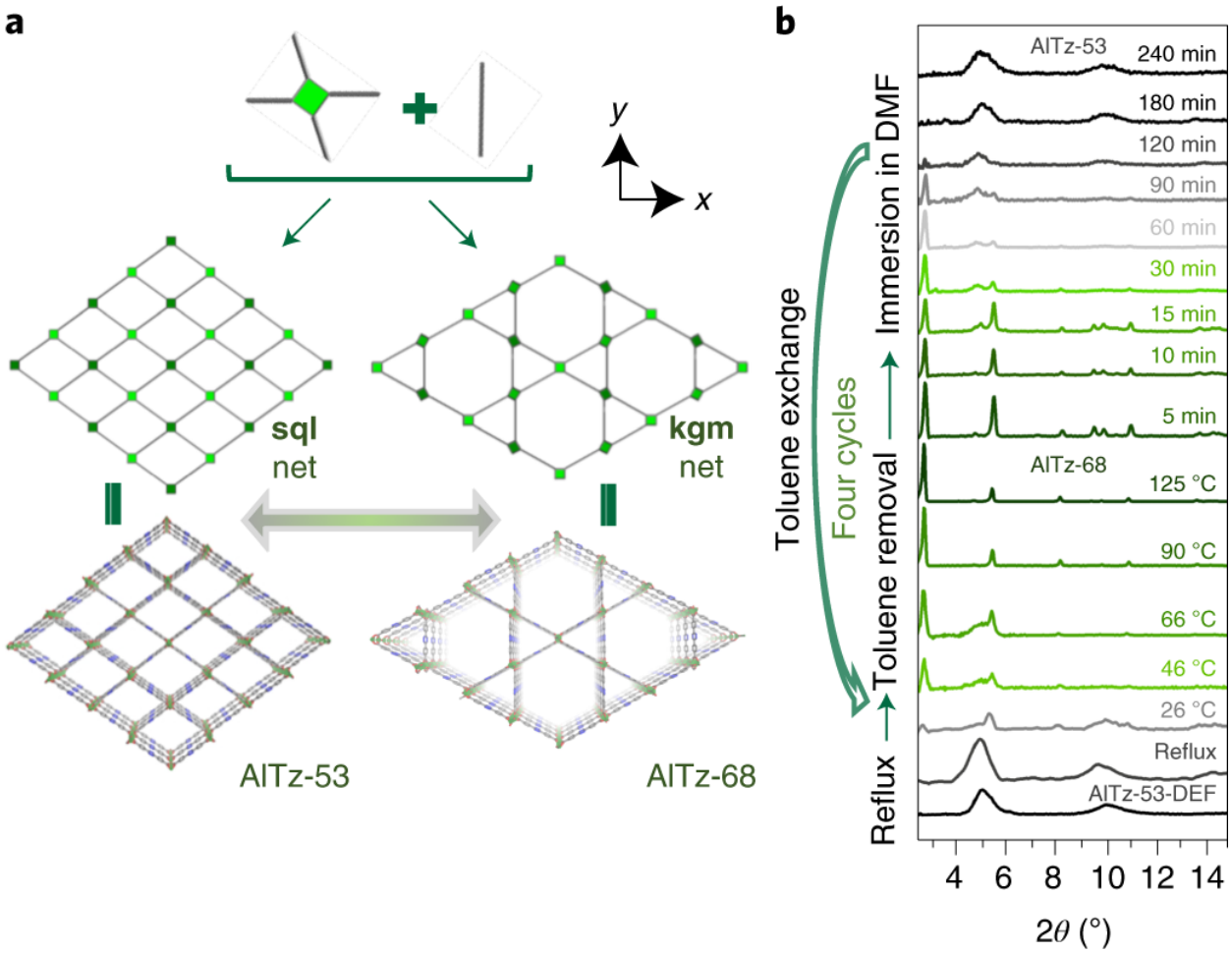

Figure 5.17: Lattice rearrangement in an Al-MOF. **a**, From a topological view, the three-dimensional net of sra ($SrAl_2$) topology in AlTz-53 can be interpreted as comprising interconnected sql nets, whereas the three-periodic AlTz-68 can be viewed as comprising interconnected kgm nets. **b**, The reversible continuous lattice rearrangement as indicated by PXRD patterns (λ = 1.5418 Å). From bottom to top: AlTz-53-DEF after being immersed in toluene, refluxed, and then dried at various temperatures while under vacuum; AlTz-68 after immersion in DMF (75 °C) for various periods of time.

crystalline isomer within 40 s following activation (solvent exchange and desolvation), resulting in a substantial increase in surface area from 725 to 2,749 m^2/g^{-1}. Spectroscopic measurements show that this counter-intuitive lattice rearrangement involves a metastable intermediate that results from solvent removal on coordinatively unsaturated metal sites. This disordered-crystalline switch between two topological distinct metal-organic frameworks is shown to be reversible over four cycles through activation and reimmersion in polar solvents.

5.3.2 Method

To further investigate the local structures, pair distribution function (PDF) analyses based on total x-ray scattering were performed on AlTz-53-DEF, AlTz-53-DMF, and AlTz-68. Total scattering data for PDF analysis were collected at beamline 28-ID-2 (XPD) at the National Synchrotron Light Source II (NSLS-II) at Brookhaven National Laboratory (BNL) using the rapid acquisition PDF method (RAPDF). High energy x-rays (66.12 keV, λ = 0.1875 Å) were used in combination with a Perkin-Elmer amorphous silicon-based area detector. The samples were loaded into Kapton capillaries for PDF measurements under ambient conditions. Background was subtracted during data processing by using PYFAI [180]. The PDFs were extracted from total scattering data using PDFGETX3 [114] and XPDFSUITE to Q_{max} = 23.5 $Å^{-1}$. For comparison with the experimental data, PDFs based on crystal structure was simulated using PDFGUI [98] For comparison with the experimental data, PDFs based on the crystal structure were simulated using PDFGUI [98]. The simulation was based on all the nonhydrogen atoms (except solvents) in the AlTz-53-DEF structure and all possible pairs were taken into account during the simulation. Q_{max} = 23.5 $Å^{-1}$ was used for the simulation. Unit cell parameters and atom positions were based on the powder diffraction data via Rietveld refinement using the AlTz-53-DEF crystal structural models reported in this article. Pseudo-Voigt profile and lattice parameters were refined using the Rietveld refinement.

5.3.3 Result

The PDF analysis reveals the local structures and indicates the disorders in network. The PDF profiles of AlTz-53-DEF and AlTz-53-DMF (Figure 5.18) are very similar, while they are somehow different from that of AlTz-68. The peaks corresponding to 1-2, 1-3, and 1-4 Al$\cdots$Al pairs can be clearly observed, at 3.3 Å, 6.5 Å and 10.5 Å, respectively. These indicate that the Al chains are preserved during the transformation. An increase of the distances for peaks corresponding to the 1-3 Al$\cdots$Al pairs (Figure 5.19) is observed, from 6.2 Å for AlTz-68 to 6.5 Å for AlTz-53-DEF. This is attributed to the missing ligands in the AlTz-53-DEF framework, as indicated by IR and NMR. A structural model of AlTz-53-DEF with missing ligands (Figure 5.20) was built, showing the flexibility of Al chains.

5.3.4 Conclusion

Desolvation can overcome the traditional challenges that come from having perfect structures that are not a natural energy minimum during one-pot syntheses, thereby providing an alternative method for producing perfect structures and achieving phase transitions that typically need extreme conditions. The desolvation-triggered domino rearrangement of AlTz-53-DEF also points to different routes for the design and preparation of novel copolymers, high-crystalline covalent organic frameworks, and metal alloys from volatile precursors, wherein monomers, functional groups or other components could potentially enable such desolvation-triggered domino rearrangements.

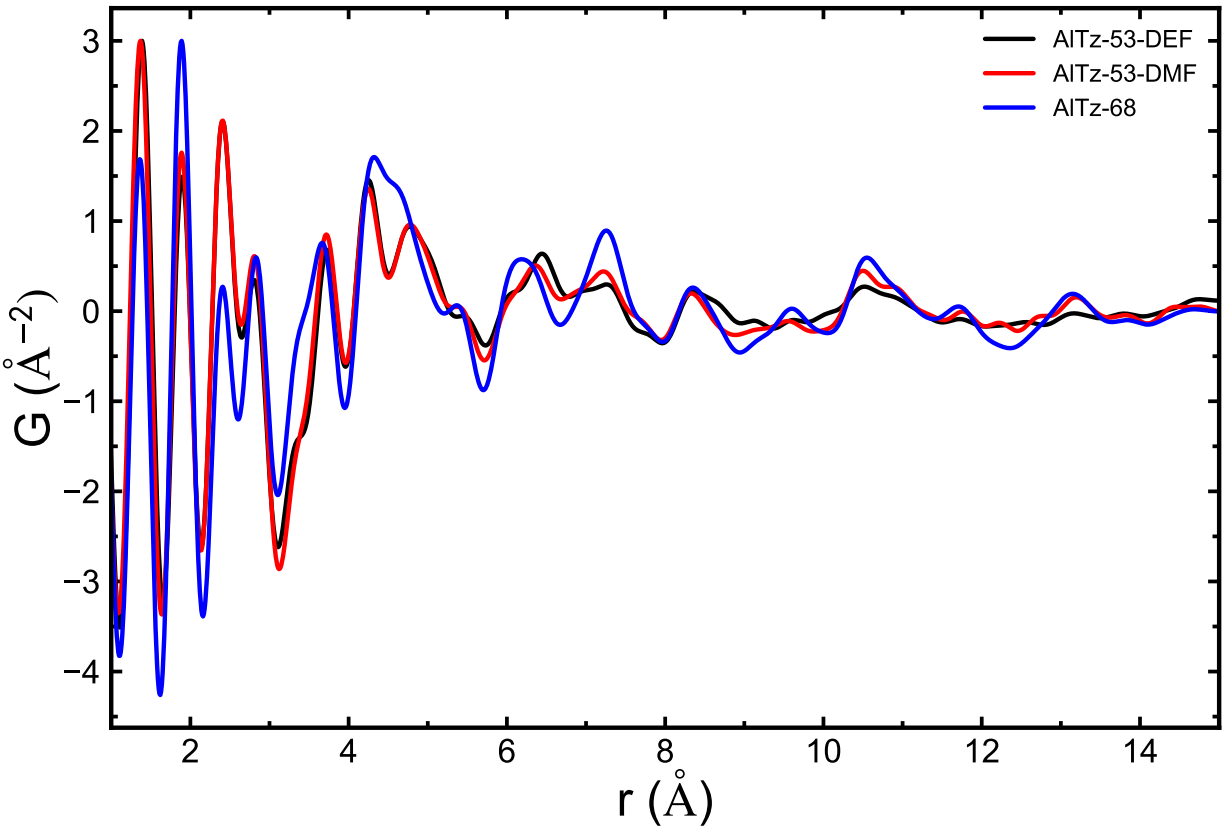

Figure 5.18: PDFs for AlTz-53-DMF, AlTz-53-DEF, and AlTz-68. The PDF profiles of AlTz-53-DEF and AlTz-53-DMF are very similar, while they are somehow different from that of AlTz-68. Comparing the PDFs for AlTz-53-DMF, AlTz-53-DEF, and AlTz-68, AlTz53 has a shorter correlation length than AlTz-68, which agrees with the idea that the structure is more disordered. In addition, all of them show a shoulder peak at 3.3 Å. As AlTz-68 has Al-chain structure, the shoulder peaks at 3.3 Å indicate presence of 1 - 2 Al$\cdots$Al pairs. The PDFs show broadened and overlapped peaks at a high r range due to low crystallinity. However, considering the stronger scattering of Al atoms, the similarity of strong peaks at high r range in different PDFs somehow indicates a similar long-range Al local environment.

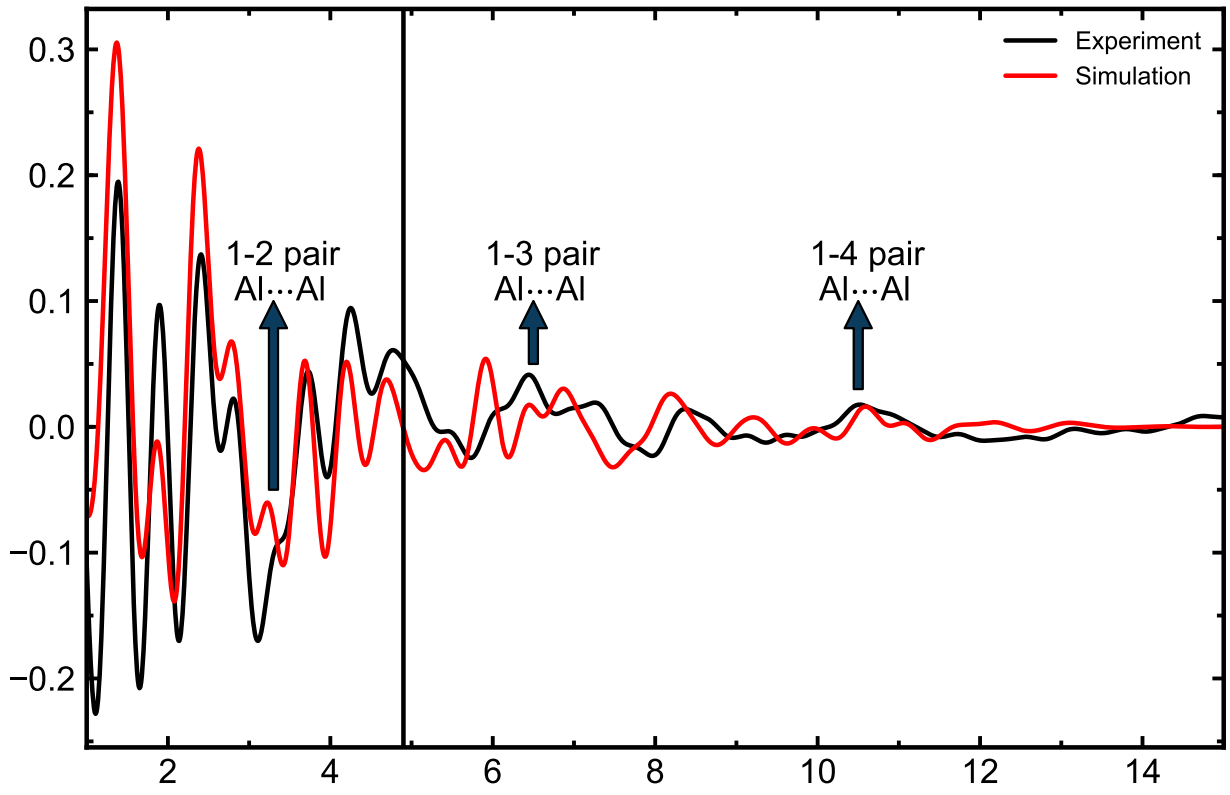

Figure 5.19: Comparison of experimental PDF for AlTz-53-DEF with that simulated using an average AlTz-53 crystal model in which the atomic displacement parameters are set to different values for low-r and high-r region. The peak at 1.4 Å is assigned to the C-C and C-N bonds in the TzDB ligand, the peak at 1.8 Å to Al-O bonds (Al-carboxylate, Al-oxo, Al-hydroxo, and Al-water), the peaks at 2.4 Å and 2.8 Å to C···C, C···N and N···N distances within the same TzDB molecule. Comparison of experimental PDF for AlTz-53-DEF with that simulated using an average AlTz-53 model shows a good agreement at a low r range. The slightly long 1-2 Al-Al distances of AlTz-53-DEF compared to simulation are attributed to the flexibility of Al chains (Figure 5.20).

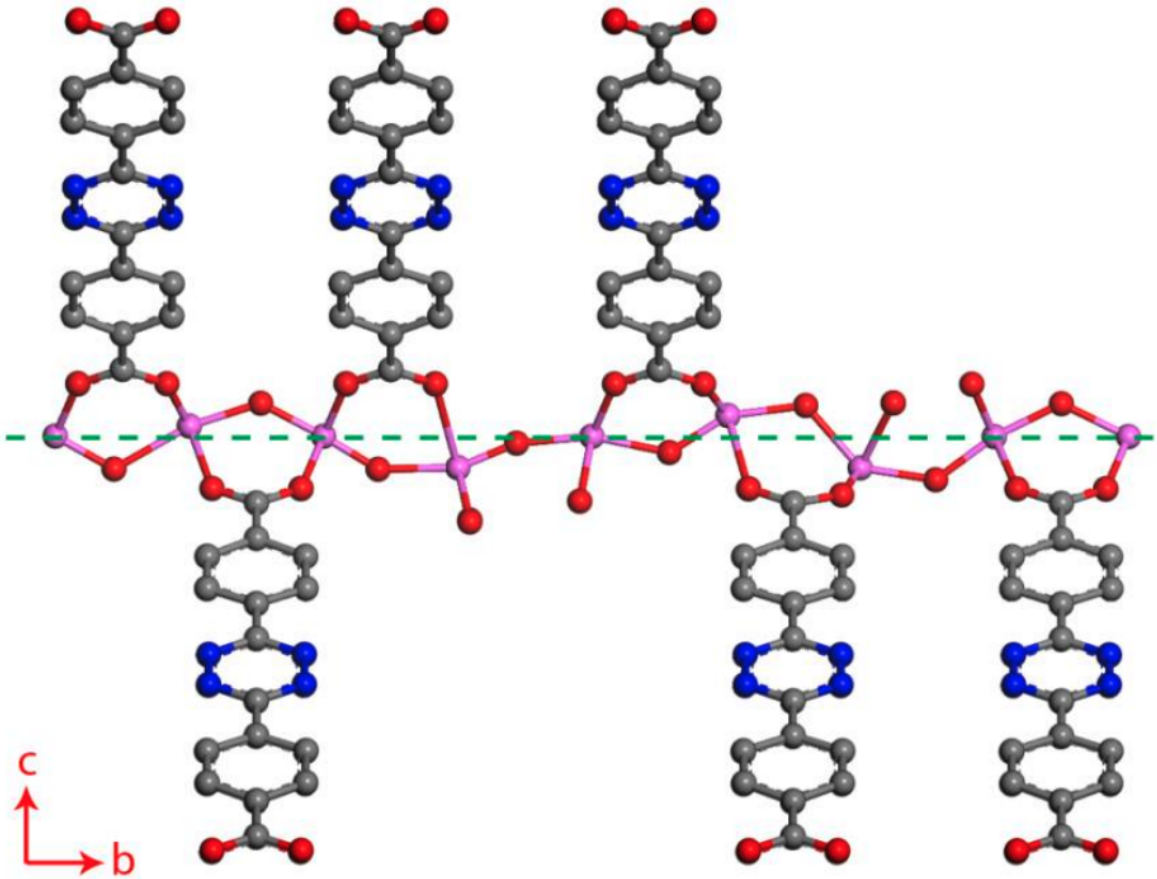

Figure 5.20: Proposed structural model of AlTz-53-DEF, showing displacements of AlO_4 tetrahedra in the chains caused by missing ligands. In an ideal structure of AlTz-53, all the Al atoms are located on the green dashed line. The ligand missing causes displacements of AlO_4 tetrahedra and longer Al$\cdots$Al distances.

Chapter 6: High-throughput *in situ* studies of the highly structurally heterogeneous samples

6.1 Introduction

Many components in real devices are highly heterogeneous and can consist of large single crystals coexisting with multi-crystal, polycrystalline, and amorphous regions in intimate contact with each other. It is, therefore, essential to have tools that can map out and characterize the characteristics of the materials as a function of position in a spatially resolved way. It is also interesting to do this mapping at high rates to watch devices in *in situ* and operando experiments. Diffraction yields quantitative information about the structure and local structure. There are multiple efforts to carry out diffraction, and local structure measurements in a spatially resolved way, including pair distribution function, computed tomography (ctPDF) [82], scanning nanostructure x-ray microscopy (SNXM) [83], scanning nanostructure electron microscopy (SNEM) [84], diffraction contrast tomography (DCT) [85], and three-dimensional x-ray scattering microscopy (3DXRD) [86, 87, 88]. In all these cases, a significant challenge is a rapidly automated reduction of the high dimensional data to a scientifically relevant form and the rapid interpretation and extraction of scientific information from the structural maps on the timescale of the experiment.

I invented a simple, rapid, and robust method named crystal mapping to generate 2D crystal maps, 1D rocking curves, and other kinds of mapping. Its computational cost is cheap and does not require a high-resolution detector. Thus, it is applicable for the quasi-real-time on-site data analysis, where users can get the results soon after the experiment and tune the experiment plan accordingly. One possible use case is to monitor grain growth in *in-situ* synthesis. I recently demonstrated the results from this method on the product of an optical floating zone furnace (OFZF) growth [69].

Here, I report on an open-source software package using an improved algorithm for the case of rapid mapping of crystal locations and orientations. I demonstrate its use to map the crystal morphology, crystallinity, and crystal quality in boules that are the product of an optical floating zone furnace (OFZF) growth. I recently demonstrated the results from this method in an *ex situ* experiment on the product of an optical floating zone furnace (OFZF) growth [69]. Here, I report on an open-source software package using an improved algorithm for the case of rapid mapping of crystal locations and orientations. I demonstrate its use to map the crystal morphology, crystallinity, and crystal quality in boules that are the product of an optical floating zone furnace (OFZF) growth. The software is available at `https://github.com/st3107/crystalmapping`.

6.2 Method and Design

6.2.1 Algorithm

There are three primary phases in the algorithm, as listed below.

- **Feature Detection** Find where QOIs are on the images.
- **Mapping** Map the time-tagged QOIs to the position coordinates.
- **Visualization** Visualize the QOIs in curve plots or color meshes.

The most complex part is the feature detection phase. The feature detection phase consists of three steps.

- (1) Calculation of the pixel-wise maximum ("maximum image" in Figure 6.1(a)), the pixel-wise minimum ("minimum image" in Figure 6.1(b)) and their subtraction ("subtracted image" in Figure 6.1(c)).
- (2) Auto-detection of the diffraction spot positions on the dark subtracted light image and the automatic selection of regions of interest.
- (3) Calculation of the average intensities in regions of interest (ROIs) and the generation of

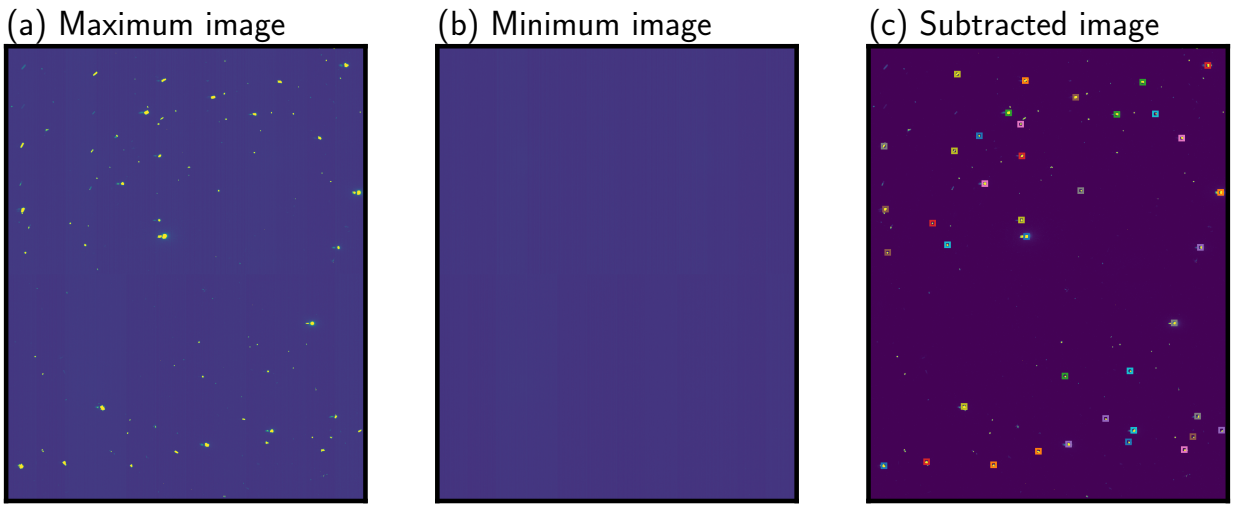

Figure 6.1: The visualization of the immediate results in the algorithm: (a) the pixel-wise maximum (abbreviated as "maximum image"); (b) the pixel-wise minimum (abbreviated as "minimum image"); (c) The difference between maximum image and minimum image (abbreviated as "subtracted image").

the "crystal maps".

In step (1), the maximum image shows peaks captured in one scan, and the minimum image records the baseline, mostly the air scattering. The difference between the two images is a "family photograph" of Bragg peaks without the air scattering, as shown in Figure 6.1(c).

In step (2), I use a particle tracking algorithm [193] to find the centers of all the Bragg peaks on the "family photograph". Once I allocate the spot centers, I select a square region around each peak center, as shown in Figure 6.1. These regions are ROIs. Users can handle the RoI size, so they are large enough to include the center Bragg peak but not too big to involve the other Bragg peaks.

In step (3), I calculate the average scattering intensity in the ROIs and tag it with the image index. I obtain a 2D tensor whose element $I(i, j)$ is the average scattering intensity in i-th ROI in j-th image. Then in the mapping phase, I map the image index to the sample positions based on the metadata, so I finally produce crystal maps. For example, if I scan the sample in a 2D grid, the crystal maps will be a 3D tensor, whose element $I(i, x_j, x_j)$ is the average scattering intensity in

i-th ROI on the image collected at (x_j, y_j) position on the sample.

The algorithm is fast because only step (2) needs time-consuming image processing, but it is only for one image, and steps (1) and (3) are simple matrix operations. It can be as fast as three shots from a dexela detector per second using only one core on the workstation at the beamline 28-ID at NSLS-II, whose time is limited by the I/O time for the image. Since the processing for one image doesn't depend on the result from the other, steps (1) and (3) can be parallelized for the batch data, which further increases the speed.

The algorithm is also robust under several tests. Even when the beam is weak, the frame rate is as quick as 0.1 sec/frame, and the noise together with dark current on the detector is relatively high, it can still produce accurate results, like those shown in Figure 6.3 and Figure 6.4. I plot the RoI on the axes. These axes can be the horizontal or vertical positions, rotation angles, or other spatial quantities. For the example experiment, I plot them in Figure 6.3 and Figure 6.4. There is one crystal map per RoI.

Although I only demonstrate the crystal maps and rocking curves, the software can process diffraction images in a scan of any axes as long as it can read the number of data points and the extent of the axes in the metadata.

6.2.2 Python Package

I implemented the algorithm in a python package. The package includes three essential functionalities.

- **Automated Experiment** Run automated x-ray microscopy experiments at National Synchrotron Light Source II (NSLS-II).
- **Streaming Processing** Start a server to automatically produce half-processed data at the beamline.
- **Batch Analysis and Visualization** Rapidly analyzes the data in batch mode after the exper-

iment, with user inputs and visualization.

I will demonstrate its usage in an example of crystal grown in an OFZF.

6.3 Example: Study Optical Float Zone Furnace Crystal Growth

Here I describe an application of the approach to study the distribution of crystal grains in a rod that has undergone growth in an optical float zone furnace. Details of the sample prep, initial experiments, and prior analysis of the grain distributions are described in [89]. I show how novel insights are obtained about the crystal quality as will as the positional distribution of the grains studied before. In particular, in the previous study, intensity variations from point to point within the grains are evident. Here I used CRYSTALMAPPING to show that these originated from a strongly spatially dependent crystal texture and were an artifact of the original measurement.

6.3.1 Spatially Resolved Experiment

The experiments were carried out at beamline 28-ID-D at NSLS-II on the same samples as used in [89]. The x-ray energy was 67.3 keV (λ = 0.184 Å) with a square beam of size 0.25 mm × 0.25 mm. The rod was mounted vertically and perpendicular to the beam. It was aligned so it could be translated horizontally and vertically in the plane perpendicular to the beam. The high energy x-rays are penetrating enough to go through the sample, and a large area Dexela 2923 detector with square pixels of size 0.075 mm × 0.075 mm was placed 565 mm behind the sample in transmission mode. Diffraction images are taken with a 1 sec exposure at a series of (x, y) positions in a grid pattern. It was also possible to rotate the rod about the rod axis, allowing data to be collected at fixed but variable angles, or with the rod rotating during the exposure. A schematic of the setup is shown in Figure 6.2. The horizontal length of the grid is around 6 mm, the vertical height is approximately 30 mm, and the step size is about 0.25 mm. CRYSTALMAPPING stores metadata automatically during the experiment, capturing the sample x, y and ϕ (Where ϕ is an angular displacement of the sample about the y-axis) positions for each image as well as the start, end, and number of points in each grid-scan

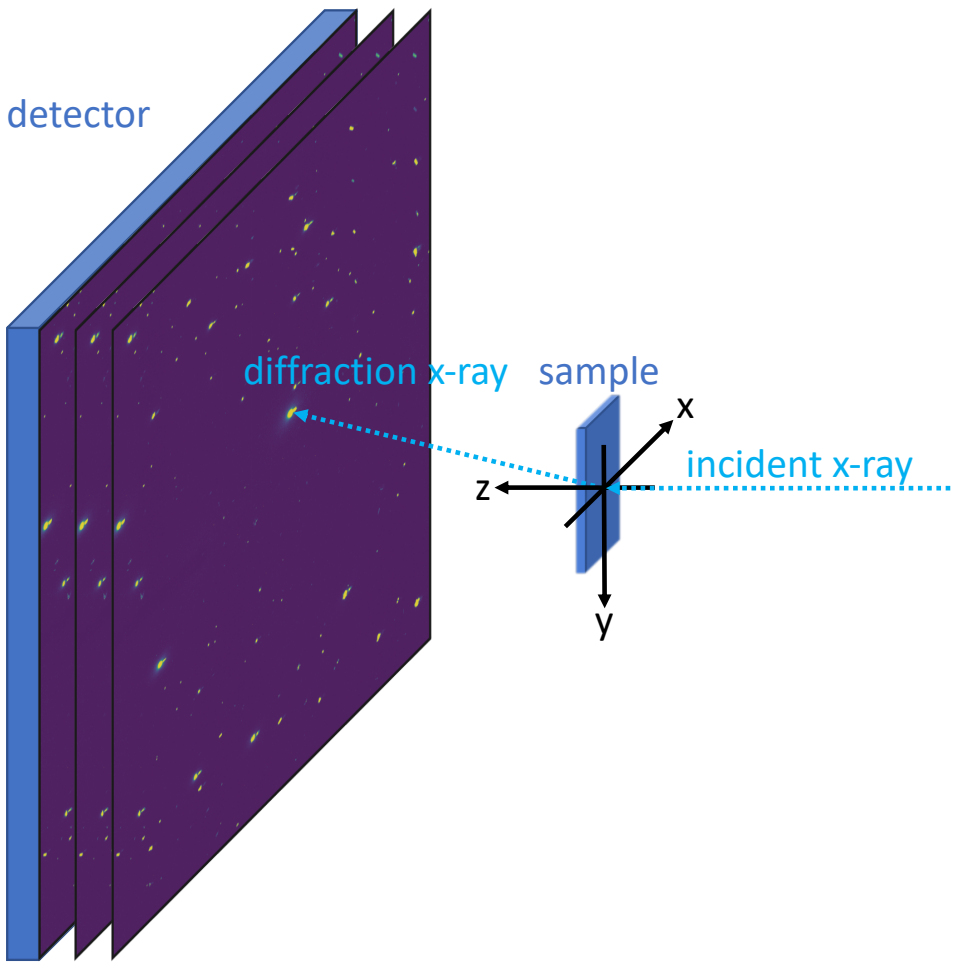

Figure 6.2: Schematic of the experimental setup. The sample is moved in x and y directions. It can also be rotated along the axis of the rod (the laboratory y-axis). The stacked diffraction images represent a time series of measurements at different (x, y) positions and/or rotation angles.

In general, the diffraction images can contain diffraction spots from a single grain, multiple grains, a smooth ring coming from a powder pattern, or just air scattering because the beam missed the sample. The algorithm has to handle this diversity of images automatically and rapidly. An example diffraction pattern is shown in Figure 6.2 where, in this case, it has the signal from multiple crystals. At NSLS-II, the instrument control software saves metadata in a MongoDB database. The metadata can be accessed using the DATABROKER software package. CRYSTALMAPPING is able to pull the images from the database and feed them to the data pipeline along with relevant metadata to automate the analysis process. In practice, many users prefer to save their data as files on the filesystem with the images in the form of TIFF or EDF files and a text based output (for example in YAML format) for the metadata. For example, this is a standard output of the XPDACQ software running at the 28-ID-1 and 28-ID-2 beamlines at NSLS-II. Directly pulling information from the database is more efficient, but CRYSTALMAPPING is also able to take data from external files on the user's filesystem also.

A code snippet showing how the CRYSTALMAPPING links to the database is shown in Snippet 6.1.

```
from crystalmapping.crystalmapper import CrystalMapper, MapperConfig
config = MapperConfig(image_data_key='dexela_image')
cm = CrystalMapper(config)
cm.load_bluesky_v2(crystal_mapping_data)
cm.auto_process()
cm.save_dataset('crystal-maps.nc')
```

Snippet 6.1: Example python code to create crystsal maps

The `CrystalMapper` class handles the functionality of doing the mapping. It will take a stream of detector images and metadata associated with them that come in the form of Bluesky event documents [194]. The documents are in the form of sets of key-value pairs (e.g., Python dictionaries), and the mapper needs to be configured so that it knows the interesting fields for it to do its work. In this case, the detector used was a Dexela 2923 detector, and its images are labeled with the key

'dexela_image' in the database. By default, it also reads the x and y positions on the sample. The cm.load_bluesky_v2 method will load a given dataset from the database and pass it as an attribute to the cm CrystalMapper object. The data is then processed using the auto_process() method, which follows the algorithm described in Section 6.2.1. A status bar will show up to indicate the progress. The results are also saved as attributes of the cm object. They can be written to a file on the filesystem with the cm.save_dataset method.

6.3.2 Discovery: Missing Parts of the Grains

Although there are multiple packages for data visualization, users may want an easy and direct way to look at the crystal maps. It is realized by the visualize method (Snippet 6.2).

```
cm.visualize()
```

Snippet 6.2: Example python code to create crystsal maps

Without needing additional settings, the CrystalMapper examines the data and metadata and determines that the data is crystal maps due to its dimensions. It will reshape the data into an array of crystal map images and show them in color meshes, which are the visualized crystal maps. The result from the experiment described in Section 6.3.1 is shown in Figure 6.3. Users can also choose what to plot by specifying the data names. For example, in the Snippet 6.3, users used the x='y', y='x' to switch the x and y axes.

```
cm.visualize(x='y', y='x')
```

Snippet 6.3: Example python code to measure a rocking curve

A detailed interpretation of similar images from float-zone grown boules can be found in [89]. In the OFZF growth process, multiple small crystals nucleate at the initiation of the growth. As the boule is drawn through the hot zone, the nucleated crystals grow, with some growing at the expense of other crystals allowing the successful crystals to grow in size until only one crystal is left, which is the desired single-crystal. Moving up in the image, I then expect to see small crystals at the bottom, growing in size as I move up the boule, as is evident in Figure 6.3. Exactly how

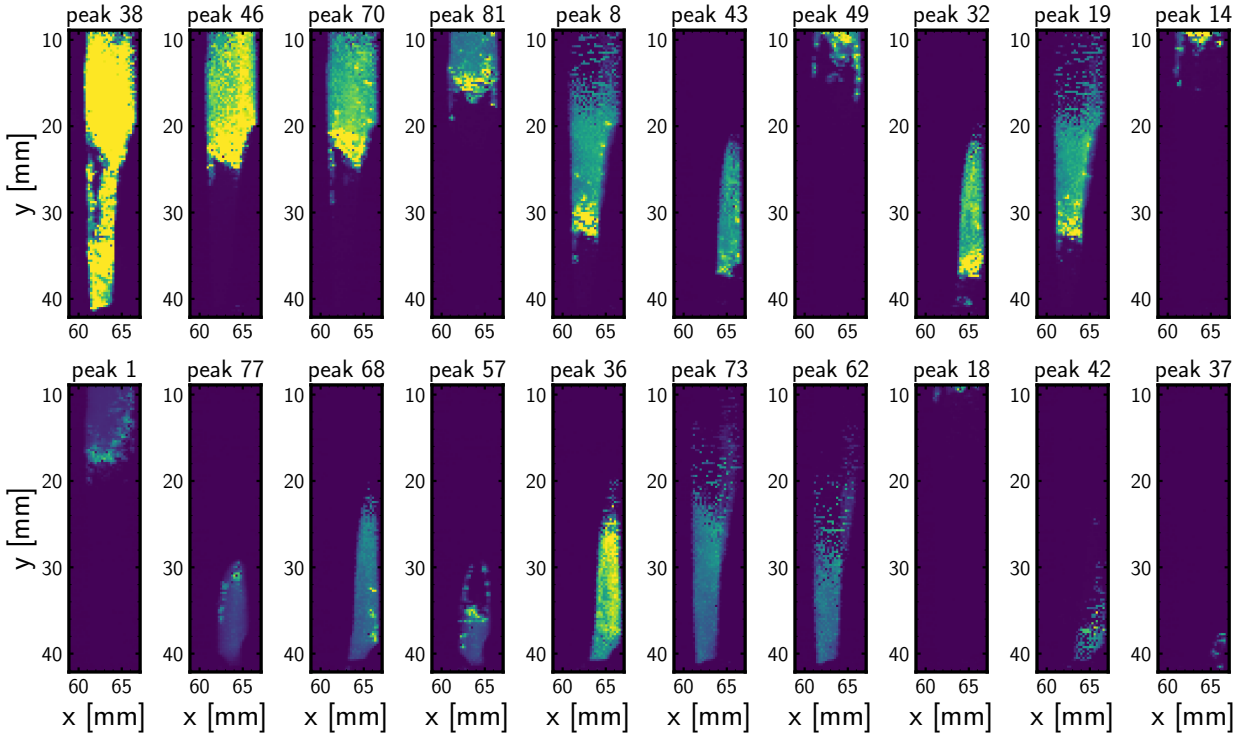

Figure 6.3: The crystal maps of the TiO_2 rod generated by the CRYSTALMAPPING package. Each panel is the visualization of the distribution of the intensity of a Bragg peak from a region in the sample on the XY plane in Figure 6.2. The yellowish color means higher intensity. These maps show how different grains distribute in the rod on the XY plane.

this happens depends on details of the growth conditions, and so in principle, such studies make it possible to understand experimental factors that affect different grain structures in the product.

The approach clearly shows the positions within the boule of each crystal. However, as reported in [89] and observed here in Figure 6.3, I find strong intensity variations with position within a single crystal grain. In [89] it was hypothesized that crystal mosaicity could explain this observation. To test this hypothesis, I would like to adapt the experiment design to carry out a rocking curve measurement for each Bragg peak at each point on the map. Here I describe how this new situation could be straightforwardly accommodated within CRYSTALMAPPING. In this measurement, I want to measure the intensity of a Bragg reflection while rotating the sample to different rotation angles, ϕ, along its axis. The rotation steps I took were 0.001 degrees through an angular range of $-1.0 \leq \Delta\phi \leq 1.0\,^{\circ}$.

As I hypothesized, the non-uniform crystal mosaicity in the rod causes a strong variation in the intensity of crystal maps. This can be seen by looking at rocking curve plots (intensity of a particular Bragg peak vs. ϕ). Because there are many Bragg peaks and many crystal positions, I would like a way to automate this process, so I incorporated this functionality into CRYSTALMAPPING. First, I collect the data in `rocking_curve` mode. In this mode, I fixed the (x, y) position of the rod and rotated ϕ according to a fixed angle with constant step size, as described above. At each angle, I collect a diffraction image. For completeness, I include the code snippet in Snippet 6.4.

```
from crystalmapping.plans import grid_scan_nd

rocking_curve = grid_scan_nd(
[pe1c],
mPhi,
-1, 1, 0.001
time_per_point=0.1,
time_per_frame=0.1,
shutter=fast_shutter,
shutter_open='Open',
```

```
shutter_close='Closed'
)
RE(rocking_curve)
```

Snippet 6.4: Example python code to measure a rocking curve

The `grid_scan_nd` is a predefined plan in CRYSTALMAPPING to conduct a scan in multiple dimensions. The required arguments are the detector list, the motor that will be scanned, and the beginning, end, and step size of the scan (in the default units of that motor). Here I were using a Perkin-Elmer detector whose software object is called `pe1c`. I also set up `rocking_curve` to make 0.1 second frame exposures for a total exposure time per point of 0.1 s. Other optional arguments tell the Bluesky run engine which shutter to open and close and some information about its state. The user then simply runs the `cm.visualize()` command and CRYSTALMAPPING detects that the data are in `rocking_curve` mode by reading the value of the `'shape'` key in the metadata. Because the loaded bluesky object always has exactly one scan, this method to determine dimensions works. It contains information on the dimension of the scan. The `CrystalMapper` will read that attribute and plot the rocking curves.

I show an example of the output of `cm.visulaize` for a set of rocking curves taken on all the Bragg peaks it identified at the position (62 mm, 15 mm) on the large grain shown in peak 38 in the Figure 6.3. An example is shown in Figure 6.4. If users would like to specify the data range or the style of the plots, they can use different options for the method to customize the visualization. For example, they will use `cm.visualize(peaks=3)` to only plot the first three peaks or use `cm.visualize(col_wrap=2)` to show only two panels in a row. They can also get the returned `matplotlib` figure object and set more detailed parameters using its methods.

As is evident in the plots in Figure 6.4, there are significant variations in intensity with ϕ. This shows not only that the crystal grains do have significant mosaicity, but also that the highly parallel synchrotron beam samples this with a high resolution. I adapted the software to accommodate rocking curve scans as the input in Snippet 6.5.

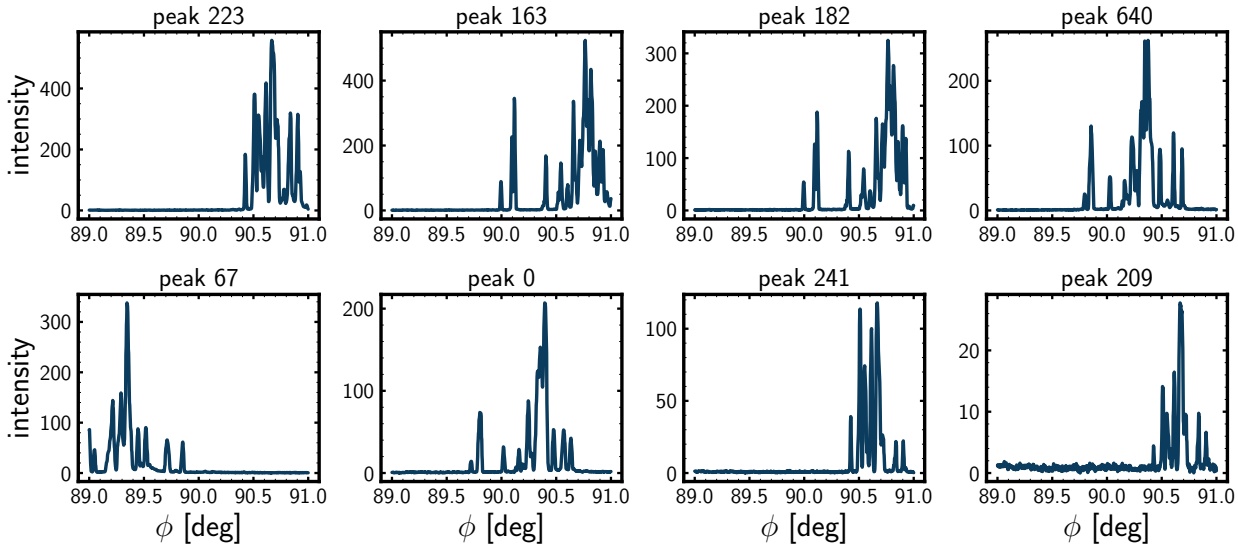

Figure 6.4: Rocking curves from a point (62 mm, 15 mm) on the large grain shown in peak 38 in Figure 6.3, automatically generated by the `rocking_curve` mode of the `cm.visualize()` method in the CRYSTALMAPPING package. Each panel depicts the intensity of a Bragg peak as a function of the rotation angle, ϕ, about the z-axis (shown schematically in Figure 6.2).

```
from crystalmapping.crystalmapper import CrystalMapper, MapperConfig
config = MapperConfig(image_data_key='dexela_image')
cm = CrystalMapper(config)
cm.load_bluesky_v2(rocking_curve_data)
cm.auto_process()
cm.save_dataset('rocking-curves.nc')
```

Snippet 6.5: Example python code to create rocking curves

The methods are the same as what I used to produce the crystal maps. It is because I designed the `CrystalMapper` so that it could understand the dimension of the data using the information in the metadata and used it in the reshaping. It can process the scan on any number of axes using the same methods for greater fine-tuning.

When the code is being run on data read from the filesystem rather than the database the code, the users should enter the path to the folder of tiff files and a yaml file. In the tiff files, the file names should be indexed in the order of the measurement. In the yaml file, it should contain the keys `'shape'`, `'extent'`, and `'snake'` like the ones in the database header. Usually, users

don't need to enter theses metadata because they are automatically recorded at NSLS-II. However, if they are using other sources, they need to the write this yaml file and enter the values according to their knowledge of the experiments.

The figure shows many peaks in a small range of rotation. The grain I measured has a high mosaicity. I can compare the "rocking curve" to assess the quality of the samples. The summed crystal map is best for showing the physical location of grains, and I may use the individual maps ("rocking curves") to get an idea about crystal mosaicity. I noted that I could obtain summed crystal maps in a standard one-image-per-location mode if I dynamically rocked the sample during the exposure at each physical location during data acquisition.

6.4 Conclusion

I implement a fast and robust algorithm in a python package CRYSTALMAPPING. It obtains the oriental and spatial distribution of single crystal grains in the samples rapidly and robustly in simple x-ray powder diffraction. I released the package on Conda (`https://anaconda.org/conda-forge/crystalmapping`), published the source code for the public on GitHub (`https://github.com/st3107/crystalmapping`), and built a documentation website (`https://st3107.github.io/crystalmapping`) for reference.

Conclusion

In this work, I presented advanced tools for analyzing the structures of nanocrystalline, nanoporous, and heterogeneous functional materials. These materials have unique physical and chemical properties at the nanoscale that make them useful in a range of applications, but their complex internal structures make them difficult to study using traditional methods.

I developed an automated platform for x-ray scattering experiments and a streaming data pipeline to produce pair distribution functions, and used these tools to study the disorders in a variety of nanoporous materials, including metal oxide nanoparticles, metal-organic frameworks, and zirconium phosphates. Our results showed that these tools are accurate and reliable, and have contributed to important scientific discoveries in probing, analyzing, and controlling the disorders in these materials.

In addition, I developed a systematic workflow for analyzing the phases and morphologies of metal oxide nanoparticles and proposed a simple but effective algorithm for studying the grain distribution and mosaicity in heterogeneous crystalline materials. Our work has demonstrated the potential to tune the disorder in nanoporous zirconium phosphates using phosphoric acid concentration, revealed evidence of polar solvent-induced lattice arrangement in an aluminum metal organic framework, and supported the reminiscent correlation of metal sites in binary metal organic framework glasses.

Overall, this work has contributed to the understanding of the structures of nanocrystalline, nanoporous, and heterogeneous functional materials and has established a foundation for future

research in this area and the potential application in photocatalysis, optical or gas sensing, radioactive waste storage, and the metallurgical industry.

References

[1] M. Eckert, "Max von Laue and the discovery of X-ray diffraction in 1912," *Annalen der Physik*, vol. 524, no. 5, A83–A85, May 2012.

[2] P. J. Withers, "Synchrotron X-ray Diffraction," in *Practical Residual Stress Measurement Methods*, John Wiley & Sons, Ltd, 2013, pp. 163–194, ISBN: 978-1-118-40283-2.

[3] S. J. L. Billinge and I. Levin, "The Problem with Determining Atomic Structure at the Nanoscale," *Science*, vol. 316, no. 5824, pp. 561–565, Apr. 2007.

[4] J. Miao, T. Ishikawa, I. K. Robinson, and M. M. Murnane, "Beyond crystallography: Diffractive imaging using coherent x-ray light sources," *s*, vol. 348, no. 6234, pp. 530–535, May 2015.

[5] J. Hill *et al.*, "Future trends in synchrotron science at NSLS-II," *Journal of Physics: Condensed Matter*, vol. 32, no. 37, p. 374 008, Sep. 2020.

[6] E. Stach *et al.*, "Autonomous experimentation systems for materials development: A community perspective," *Matter*, vol. 4, no. 9, pp. 2702–2726, Sep. 2021.

[7] Y. Rakita *et al.*, "Active Reaction Control of Cu Redox State Based on Real-Time Feedback from In Situ Synchrotron Measurements," *Journal of the American Chemical Society*, vol. 142, no. 44, pp. 18 758–18 762, Nov. 2020.

[8] Z. Chen *et al.*, "Machine learning on neutron and x-ray scattering and spectroscopies," *Chemical Physics Reviews*, vol. 2, no. 3, p. 031 301, Sep. 2021.

[9] K. Mader, F. Marone, C. Hintermüller, G. Mikuljan, A. Isenegger, and M. Stampanoni, "High-throughput full-automatic synchrotron-based tomographic microscopy," *Journal of Synchrotron Radiation*, vol. 18, no. 2, pp. 117–124, Mar. 2011.

[10] J. M. Gregoire, D. G. Van Campen, C. E. Miller, R. J. R. Jones, S. K. Suram, and A. Mehta, "High-throughput synchrotron X-ray diffraction for combinatorial phase mapping," *Journal of Synchrotron Radiation*, vol. 21, no. 6, pp. 1262–1268, Nov. 2014.

[11] C. Wang, U. Steiner, and A. Sepe, "Synchrotron Big Data Science," *Small*, vol. 14, no. 46, p. 1 802 291, Nov. 2018.

[12] A. Arkilic, D. B. Allan, T. Caswell, L. Li, K. Lauer, and S. Abeykoon, "Towards Integrated Facility-Wide Data Acquisition and Analysis at NSLS-II," *Synchrotron Radiation News*, vol. 30, no. 2, pp. 44–45, Mar. 2017.

[13] M. F. Sanner and others, "Python: A programming language for software integration and development," *Journal of molecular graphics & modelling*, vol. 17, no. 1, pp. 57–61, 1999.

[14] M. S. Chavali and M. P. Nikolova, "Metal oxide nanoparticles and their applications in nanotechnology," *SN Applied Sciences*, vol. 1, no. 6, p. 607, May 2019.

[15] M. E. Franke, T. J. Koplin, and U. Simon, "Metal and Metal Oxide Nanoparticles in Chemiresistors: Does the Nanoscale Matter?" *Small*, vol. 2, no. 1, pp. 36–50, 2006.

[16] I. E. Wachs, "Recent conceptual advances in the catalysis science of mixed metal oxide catalytic materials," *Catalysis Today*, 100th Anniversary Issue, vol. 100, no. 1, pp. 79–94, Feb. 2005.

[17] N. Yamazoe, G. Sakai, and K. Shimanoe, "Oxide Semiconductor Gas Sensors," *Catalysis Surveys from Asia*, vol. 7, no. 1, pp. 63–75, Apr. 2003.

[18] S. Samson and C. G. Fonstad, "Defect structure and electronic donor levels in stannic oxide crystals," *Journal of Applied Physics*, vol. 44, no. 10, pp. 4618–4621, Oct. 1973.

[19] P. B. Weisz, "Effects of Electronic Charge Transfer between Adsorbate and Solid on Chemisorption and Catalysis," *The Journal of Chemical Physics*, vol. 21, no. 9, pp. 1531–1538, Sep. 1953.

[20] H. Ogawa, M. Nishikawa, and A. Abe, "Hall measurement studies and an electrical conduction model of tin oxide ultrafine particle films," *Journal of Applied Physics*, vol. 53, no. 6, pp. 4448–4455, Jun. 1982.

[21] A. I. West and S. of Photo-optical Instrumentation Engineers, Eds., *Catheter-based sensing and imaging technology: 17-18 January 1989, Los Angeles, California* (Proceedings / SPIE–the International Society for Optical Engineering 1068). Bellingham, Wash., USA: SPIE, 1989, ISBN: 978-0-8194-0103-8.

[22] W. Göpel and K. D. Schierbaum, "SnO2 sensors: Current status and future prospects," *Sensors and Actuators B: Chemical*, vol. 26, no. 1, pp. 1–12, Jan. 1995.

[23] K. D. Schierbaum, U. Weimar, W. Göpel, and R. Kowalkowski, "Conductance, work function and catalytic activity of SnO2-based gas sensors," *Sensors and Actuators B: Chemical*, vol. 3, no. 3, pp. 205–214, Mar. 1991.

[24] C. Xu, J. Tamaki, N. Miura, and N. Yamazoe, "Correlation between Gas Sensitivity and Crystallite Size in Porous SnO2-Based Sensors," *Chemistry Letters*, vol. 19, no. 3, pp. 441–444, Mar. 1990.

[25] C. Xu, J. Tamaki, N. Miura, and N. Yamazoe, "Grain size effects on gas sensitivity of porous SnO2-based elements," *Sensors and Actuators B: Chemical*, vol. 3, no. 2, pp. 147–155, 1991.

[26] J Tamaki *et al.*, "Grain-size effects in tungsten oxide-based sensor for nitrogen oxides," *Journal of the Electrochemical Society*, vol. 141, no. 8, p. 2207, 1994.

[27] T. Proffen and S. J. L. Billinge, "PDFFIT, a program for full profile structural refinement of the atomic pair distribution function," *Journal of Applied Crystallography*, vol. 32, no. 3, pp. 572–575, Jun. 1999.

[28] J. Lee, O. K. Farha, J. Roberts, K. A. Scheidt, S. T. Nguyen, and J. T. Hupp, "Metal-organic framework materials as catalysts," *Chemical Society Reviews*, vol. 38, no. 5, pp. 1450–1459, 2009.

[29] L. E. Kreno, K. Leong, O. K. Farha, M. Allendorf, R. P. Van Duyne, and J. T. Hupp, "Metal-Organic Framework Materials as Chemical Sensors," *Chemical Reviews*, vol. 112, no. 2, pp. 1105–1125, Feb. 2012.

[30] K. J. Gagnon, H. P. Perry, and A. Clearfield, "Conventional and Unconventional Metal-Organic Frameworks Based on Phosphonate Ligands: MOFs and UMOFs," *Chemical Reviews*, vol. 112, no. 2, pp. 1034–1054, Feb. 2012.

[31] D. J. Tranchemontagne, J. L. Mendoza-Cortés, M. O'Keeffe, and O. M. Yaghi, "Secondary building units, nets and bonding in the chemistry of metal-organic frameworks," *Chemical Society Reviews*, vol. 38, no. 5, pp. 1257–1283, 2009.

[32] Z. Wang and S. M. Cohen, "Postsynthetic modification of metal-organic frameworks," *Chemical Society Reviews*, vol. 38, no. 5, pp. 1315–1329, 2009.

[33] O. K. Farha *et al.*, "De novo synthesis of a metal-organic framework material featuring ultrahigh surface area and gas storage capacities," *Nature chemistry*, vol. 2, no. 11, pp. 944–948, 2010.

[34] P. Ryan, O. K. Farha, L. J. Broadbelt, and R. Q. Snurr, "Computational screening of metal-organic frameworks for xenon/krypton separation," *AIChE Journal*, vol. 57, no. 7, pp. 1759–1766, 2011.

[35] J.-R. Li, R. J. Kuppler, and H.-C. Zhou, "Selective gas adsorption and separation in metal-organic frameworks," *Chemical Society Reviews*, vol. 38, no. 5, pp. 1477–1504, 2009.

[36] D. J. Collins and H.-C. Zhou, "Hydrogen storage in metal-organic frameworks," *Journal of materials chemistry*, vol. 17, no. 30, pp. 3154–3160, 2007.

[37] J.-R. Li *et al.*, "Carbon dioxide capture-related gas adsorption and separation in metal-organic frameworks," *Coordination Chemistry Reviews*, vol. 255, no. 15-16, pp. 1791–1823, 2011.

[38] A. Clearfield, "Unconventional metal organic frameworks: Porous cross-linked phosphonates," *Dalton Transactions*, no. 44, pp. 6089–6102, 2008.

[39] M. Dines, R. Cooksey, P. Griffith, and R. H. Lane, "Mixed-component layered tetravalent metal phosphonates/phosphates as precursors for microporous materials," *Inorganic Chemistry*, vol. 22, no. 6, pp. 1003–1004, 1983.

[40] N. Ma and S. Horike, "Metal-Organic Network-Forming Glasses," *Chemical Reviews*, vol. 122, no. 3, pp. 4163–4203, Feb. 2022.

[41] T. D. Bennett and S. Horike, "Liquid, glass and amorphous solid states of coordination polymers and metal-organic frameworks," *Nature Reviews Materials*, vol. 3, no. 11, pp. 431–440, Nov. 2018.

[42] S. Kitagawa, "Future Porous Materials," *Accounts of Chemical Research*, vol. 50, no. 3, pp. 514–516, Mar. 2017.

[43] D. Umeyama, S. Horike, M. Inukai, T. Itakura, and S. Kitagawa, "Reversible Solid-to-Liquid Phase Transition of Coordination Polymer Crystals," *Journal of the American Chemical Society*, vol. 137, no. 2, pp. 864–870, Jan. 2015.

[44] T. D. Bennett *et al.*, "Hybrid glasses from strong and fragile metal-organic framework liquids," *Nature Communications*, vol. 6, no. 1, p. 8079, Nov. 2015.

[45] K. Tanaka *et al.*, "High Li-Ion Conductivity in $Li\{N(SO_2F)_2\}(NCCH_2CH_2CN)_2$ Molecular Crystal," *Nano Letters*, vol. 20, no. 11, pp. 8200–8204, Nov. 2020.

[46] T. Ogawa *et al.*, "Coordination polymer glass from a protic ionic liquid: Proton conductivity and mechanical properties as an electrolyte," *Chemical Science*, vol. 11, no. 20, pp. 5175–5181, 2020.

[47] N. Ma, S. Kosasang, A. Yoshida, and S. Horike, "Proton-conductive coordination polymer glass for solid-state anhydrous proton batteries," *Chemical Science*, vol. 12, no. 16, pp. 5818–5824, 2021.

[48] Y. Hirai *et al.*, "Luminescent Coordination Glass: Remarkable Morphological Strategy for Assembled Eu(III) Complexes," *Inorganic Chemistry*, vol. 54, no. 9, pp. 4364–4370, May 2015.

[49] S. Vaidya *et al.*, "Transparent and luminescent glasses of gold thiolate coordination polymers," *Chemical Science*, vol. 11, no. 26, pp. 6815–6823, 2020.

[50] M. A. Ali, X. Liu, Y. Li, J. Ren, and J. Qiu, "Nonlinear-Optical Response in Zeolitic Imidazolate Framework Glass," *Inorganic Chemistry*, vol. 59, no. 12, pp. 8380–8386, Jun. 2020.

[51] L. Longley *et al.*, "Publisher Correction: Liquid phase blending of metal-organic frameworks," *Nature Communications*, vol. 9, no. 1, p. 4402, Dec. 2018.

[52] C. W. Ashling *et al.*, "Synthesis and Properties of a Compositional Series of MIL-53(Al) Metal-Organic Framework Crystal-Glass Composites," *Journal of the American Chemical Society*, vol. 141, no. 39, pp. 15 641–15 648, Oct. 2019.

[53] J. Hou *et al.*, "Metal-organic framework crystal-glass composites," *Nature Communications*, vol. 10, no. 1, p. 2580, Dec. 2019.

[54] C. J. Roberts and P. G. Debenedetti, "Polyamorphism and density anomalies in network-forming fluids: Zeroth- and first-order approximations," *The Journal of Chemical Physics*, vol. 105, no. 2, pp. 658–672, Jul. 1996.

[55] P. S. Salmon, R. A. Martin, P. E. Mason, and G. J. Cuello, "Topological versus chemical ordering in network glasses at intermediate and extended length scales," *Nature*, vol. 435, no. 7038, pp. 75–78, May 2005.

[56] M. Liu *et al.*, "Network-Forming Liquids from Metal-Bis(acetamide) Frameworks with Low Melting Temperatures," *Journal of the American Chemical Society*, Feb. 2021.

[57] S. Polarz and B. Smarsly, "Nanoporous Materials," *Journal of Nanoscience and Nanotechnology*, vol. 2, no. 6, pp. 581–612, Dec. 2002.

[58] E. P. George, D. Raabe, and R. O. Ritchie, "High-entropy alloys," *Nature Reviews Materials*, vol. 4, no. 8, pp. 515–534, Aug. 2019.

[59] J. P. Hirth, "The influence of grain boundaries on mechanical properties," *Metallurgical Transactions*, vol. 3, no. 12, pp. 3047–3067, Dec. 1972.

[60] R. G. Burkovsky *et al.*, "Structural Heterogeneity and Diffuse Scattering in Morphotropic Lead Zirconate-Titanate Single Crystals," *Physical Review Letters*, vol. 109, no. 9, p. 097 603, Aug. 2012.

[61] W. Xia, X. Zhao, L. Yue, and Z. Zhang, "A review of composition evolution in Ni-based single crystal superalloys," *Journal of Materials Science & Technology*, vol. 44, pp. 76–95, May 2020.

[62] I. H. Levin, “Synthesis of Precious Stones.,” *Journal of Industrial & Engineering Chemistry*, vol. 5, no. 6, pp. 495–500, Jun. 1913.

[63] J. Wang, G. Zhang, H. Yu, Y. Wang, and C. Chen, “5 - Czochralski and Flux Growth of Crystals for Lasers and Nonlinear Optics,” in *Handbook of Crystal Growth (Second Edition)*, ser. Handbook of Crystal Growth, P. Rudolph, Ed., Boston: Elsevier, Jan. 2015, pp. 169–208, ISBN: 978-0-444-63303-3.

[64] Y. Janssen *et al.*, “Reciprocal Salt Flux Growth of LiFePO $_4$\$ Single Crystals with Controlled Defect Concentrations,” *Chemistry of Materials*, vol. 25, no. 22, pp. 4574–4584, Nov. 2013.

[65] P. W. Bridgman, “Certain Physical Properties of Single Crystals of Tungsten, Antimony, Bismuth, Tellurium, Cadmium, Zinc, and Tin,” *Proceedings of the American Academy of Arts and Sciences*, vol. 60, no. 6, p. 305, 1925.

[66] A. Muiznieks, J. Virbulis, A. Lüdge, H. Riemann, and N. Werner, “7 - Floating Zone Growth of Silicon,” in *Handbook of Crystal Growth (Second Edition)*, ser. Handbook of Crystal Growth, P. Rudolph, Ed., Boston: Elsevier, Jan. 2015, pp. 241–279, ISBN: 978-0-444-63303-3.

[67] P. H. Keck and M. J. E. Golay, “Crystallization of Silicon from a Floating Liquid Zone,” *Physical Review*, vol. 89, no. 6, pp. 1297–1297, Mar. 1953.

[68] H. C. Theuerer, “Method of processing semiconductive materials,” pat. US3060123A, Oct. 1962.

[69] C. J. Wright, “Towards Real Time Characterization of Grain Growth from the Melt,” Ph.D. Columbia University, United States – New York, 2021.

[70] T. Akashi, K. Matumi, T. Okada, and T. Mizutani, “Preparation of ferrite single crystals by new floating zone technique,” *IEEE Transactions on Magnetics*, vol. 5, no. 3, pp. 285–289, Sep. 1969.

[71] H. Dabkowska, A. Dabkowski, R. Hermann, J. Priede, and G. Gerbeth, “8 - Floating Zone Growth of Oxides and Metallic Alloys,” in *Handbook of Crystal Growth*, Boston: Elsevier, 2015, pp. 281–329.

[72] T. Tanaka, E. Bannai, S. Kawai, and T. Yamane, “Growth of high purity LaB6 single crystals by multi-float zone passage,” *Journal of Crystal Growth*, vol. 30, no. 2, pp. 193–197, Sep. 1975.

[73] H Takeya, E Habuta, H Kawano-Furukawa, T Ooba, and K Hirata, “Magnetization isotherms on ErNi2B2C, Er0.8Tb0.2Ni2B2C and Er0.8Lu0.2Ni2B2C single crystals,” *Journal of*

Magnetism and Magnetic Materials, Proceedings of the International Conference on Magnetism (ICM 2000), vol. 226-230, pp. 269–271, May 2001.

[74] G Behr *et al.*, "Growth of RENi2B2C single crystals by RF-zone melting," *Journal of Crystal Growth*, vol. 198-199, pp. 642–648, Mar. 1999.

[75] A. Revcolevschi and J. Jegoudez, "Growth of large high-Tc single crystals by the floating zone method: A review," *Progress in Materials Science*, vol. 42, no. 1, pp. 321–339, Jan. 1997.

[76] S. M. Koohpayeh *et al.*, "Optical floating zone crystal growth and magnetic properties of MgCr2O4," *Journal of Crystal Growth*, vol. 384, pp. 39–43, Dec. 2013.

[77] V. K. Anand, A. T. M. N. Islam, A. Samartzis, J. Xu, N. Casati, and B. Lake, "Optimization of single crystal growth of candidate quantum spin-ice Pr2Hf2O7 by optical floating-zone method," *Journal of Crystal Growth*, vol. 498, pp. 124–129, Sep. 2018.

[78] L. Frazer, K. B. Chang, K. R. Poeppelmeier, and J. B. Ketterson, "Cupric oxide inclusions in cuprous oxide crystals grown by the floating zone method," *Science and Technology of Advanced Materials*, vol. 16, no. 3, May 2015.

[79] K. B. Chang, L. Frazer, J. J. Schwartz, J. B. Ketterson, and K. R. Poeppelmeier, "Removal of Copper Vacancies in Cuprous Oxide Single Crystals Grown by the Floating Zone Method," *Crystal Growth & Design*, vol. 13, no. 11, pp. 4914–4922, Nov. 2013.

[80] G. Behr, W. Löser, N. Wizent, P. Ribeiro, M.-O. Apostu, and D. Souptel, "Influence of heat distribution and zone shape in the floating zone growth of selected oxide compounds," *Journal of Materials Science*, vol. 45, no. 8, pp. 2223–2227, Apr. 2010.

[81] A. S. Tremsin *et al.*, "In-Situ Observation of Phase Separation During Growth of Cs2LiLaBr6:Ce Crystals Using Energy-Resolved Neutron Imaging," *Crystal Growth & Design*, vol. 17, no. 12, pp. 6372–6381, Dec. 2017.

[82] S. D. M. Jacques *et al.*, "Pair distribution function computed tomography," *Nature Communications*, vol. 4, no. 1, p. 2536, Sep. 2013.

[83] A. Kovyakh *et al.*, "Towards scanning nanostructure x-ray microscopy," *arXiv:2110.01656 [cond-mat]*, Oct. 2021.

[84] Y. Rakita *et al.*, "Mapping Structural Heterogeneity at the Nanoscale with Scanning Nanostructure Electron Microscopy (SNEM)," *arXiv:2110.03589 [cond-mat]*, Oct. 2021.

[85] A. King, P. Reischig, J. Adrien, and W. Ludwig, "First laboratory X-ray diffraction contrast tomography for grain mapping of polycrystals," *Journal of Applied Crystallography*, vol. 46, no. 6, pp. 1734–1740, Dec. 2013.

[86] H. F. Poulsen *et al.*, "Three-dimensional maps of grain boundaries and the stress state of individual grains in polycrystals and powders," *Journal of Applied Crystallography*, vol. 34, no. 6, pp. 751–756, Dec. 2001.

[87] A. Lyckegaard *et al.*, "3D Grain Reconstruction from Boxscan Data," NAVAL RESEARCH LAB WASHINGTON DC, Tech. Rep., Jan. 2010.

[88] H. F. Poulsen, "An introduction to three-dimensional X-ray diffraction microscopy," *Journal of Applied Crystallography*, vol. 45, no. 6, pp. 1084–1097, Dec. 2012.

[89] C. J. C. Wright, E. Dooryhée, L. A. Pressley, W. A. Phelan, P. G. Khalifah, and S. J. L. Billinge, "Toward In Situ Synchrotron Mapping of Crystal Selection Processes during Crystal Growth," *Chemistry of Materials*, Apr. 2021.

[90] S. Banerjee, "Improved Modeling of Nanocrystals from Atomic Pair Distribution Function Data," Ph.D. Columbia University, United States – New York.

[91] P. Debye, "Zerstreuung von Röntgenstrahlen," *Annalen der Physik*, vol. 351, no. 6, pp. 809–823, Jan. 1915.

[92] C. Kittel, *Solid state physics*. Shell Development Company, 1955, vol. 3.

[93] S. J. L. Billinge, "The rise of the X-ray atomic pair distribution function method: A series of fortunate events," *Philosophical Transactions of the Royal Society A: Mathematical, Physical and Engineering Sciences*, vol. 377, no. 2147, p. 20 180 413, Jun. 2019.

[94] H. Zhu *et al.*, "Bridging Structural Inhomogeneity to Functionality: Pair Distribution Function Methods for Functional Materials Development," *Advanced Science*, vol. 8, no. 6, p. 2 003 534, Mar. 2021.

[95] D. A. Keen, "Total scattering and the pair distribution function in crystallography," *Crystallography Reviews*, vol. 26, no. 3, pp. 143–201, Jul. 2020.

[96] M. W. Terban and S. J. L. Billinge, "Structural Analysis of Molecular Materials Using the Pair Distribution Function," *Chemical Reviews*, vol. 122, no. 1, pp. 1208–1272, Jan. 2022.

[97] A. Kern and A. Coelho, "TOPAS version 2.1: General profile and structure analysis software for powder diffraction data," *Bruker AXS Karlsruhe*, vol. 79, 1998.

[98] C. L. Farrow *et al.*, "PDFfit2 and PDFgui: Computer programs for studying nanostructure in crystals," *Journal of Physics: Condensed Matter*, vol. 19, no. 33, p. 335 219, Jul. 2007.

[99] M. G. Tucker, D. A. Keen, M. T. Dove, A. L. Goodwin, and Q. Hui, "RMCProfile: Reverse Monte Carlo for polycrystalline materials," *Journal of Physics: Condensed Matter*, vol. 19, no. 33, p. 335 218, 2007.

[100] P. Juhás, C. L. Farrow, X. Yang, K. R. Knox, and S. J. L. Billinge, "Complex modeling: A strategy and software program for combining multiple information sources to solve ill posed structure and nanostructure inverse problems," *Acta Crystallographica Section A Foundations and Advances*, vol. 71, no. 6, pp. 562–568, Nov. 2015.

[101] T. Bicer *et al.*, "Real-Time Data Analysis and Autonomous Steering of Synchrotron Light Source Experiments," in *2017 IEEE 13th International Conference on e-Science (e-Science)*, Oct. 2017, pp. 59–68.

[102] Y. Ren, Z. Liu, F. Pourpoint, A. R. Armstrong, C. P. Grey, and P. G. Bruce, "Nanoparticulate TiO2(B): An Anode for Lithium-Ion Batteries," *Angewandte Chemie*, vol. 124, no. 9, pp. 2206–2209, 2012.

[103] T. Feist and P. Davies, "The soft chemical synthesis of tio2 (b) from layered titanates," *Journal of Solid State Chemistry*, vol. 101, pp. 275–295, 1992.

[104] M. Aykol, S. S. Dwaraknath, W. Sun, and K. A. Persson, "Thermodynamic limit for synthesis of metastable inorganic materials," *Science advances*, vol. 4, no. 4, eaaq0148, 2018.

[105] E. P. Meagher, "Polyhedral thermal expansion in the tio2 polymorphs: Refinement of the crystal structures of rutile and brookite at high temperatures sample at 625 degrees c," *The Canadian Mineralogist*, vol. 17, pp. 77–85, 1979.

[106] S. J. L. Billinge, *Nanometre-scale structure from powder diffraction: Total scattering and atomic pair distribution function analysis*, text, 2019.

[107] C. L. Farrow and S. J. L. Billinge, "Relationship between the atomic pair distribution function and small-angle scattering: Implications for modeling of nanoparticles," *Acta Crystallographica Section A: Foundations of Crystallography*, vol. 65, no. 3, pp. 232–239, May 2009.

[108] A. S. Barnard and L. A. Curtiss, "Prediction of TiO2 Nanoparticle Phase and Shape Transitions Controlled by Surface Chemistry," *Nano Letters*, vol. 5, no. 7, pp. 1261–1266, Jul. 2005.

[109] M. Kong *et al.*, "Tuning the Relative Concentration Ratio of Bulk Defects to Surface Defects in TiO_2 Nanocrystals Leads to High Photocatalytic Efficiency," *Journal of the American Chemical Society*, vol. 133, no. 41, pp. 16 414–16 417, Oct. 2011.

[110] J. Billet, W. Dujardin, K. De Keukeleere, K. De Buysser, J. De Roo, and I. Van Driessche, "Size Tunable Synthesis and Surface Chemistry of Metastable TiO2-Bronze Nanocrystals," *Chemistry of Materials*, vol. 30, no. 13, pp. 4298–4306, Jul. 2018.

[111] P. J. Chupas, X. Qiu, J. C. Hanson, P. L. Lee, C. P. Grey, and S. J. L. Billinge, "Rapid-acquisition pair distribution function (RA-PDF) analysis," *Journal of Applied Crystallography*, vol. 36, no. 6, pp. 1342–1347, Dec. 2003.

[112] T. Egami and S. J. L. Billinge, *Underneath the Bragg Peaks: Structural Analysis of Complex Materials*. Newnes, Dec. 2012, ISBN: 978-0-08-097141-4.

[113] J. Kieffer and D. Karkoulis, "PyFAI, a versatile library for azimuthal regrouping," *Journal of Physics: Conference Series*, vol. 425, no. 20, p. 202 012, Mar. 2013.

[114] P. Juhás, T. Davis, C. L. Farrow, and S. J. L. Billinge, "PDFgetX3: A rapid and highly automatable program for processing powder diffraction data into total scattering pair distribution functions," *J. Appl. Crystallogr.*, vol. 46, pp. 560–566, 2013.

[115] X. Yang, P. Juhas, C. L. Farrow, and S. J. L. Billinge, *xPDFsuite: An end-to-end software solution for high throughput pair distribution function transformation, visualization and analysis*, Feb. 2015.

[116] L. Yang *et al.*, "A cloud platform for atomic pair distribution function analysis: PDFitc," *Acta Crystallographica Section A: Foundations and Advances*, vol. 77, no. 1, pp. 2–6, Jan. 2021.

[117] L. Yang, P. Juhás, M. W. Terban, M. G. Tucker, and S. J. L. Billinge, "Structure-mining: Screening structure models by automated fitting to the atomic pair distribution function over large numbers of models," *Acta Crystallographica Section A: Foundations and Advances*, vol. 76, no. 3, pp. 395–409, May 2020.

[118] S. Gražulis *et al.*, "Crystallography Open Database - an open-access collection of crystal structures," *Journal of Applied Crystallography*, vol. 42, no. 4, pp. 726–729, Aug. 2009.

[119] S. P. Ong *et al.*, "Python Materials Genomics (pymatgen): A robust, open-source python library for materials analysis," *Computational Materials Science*, vol. 68, pp. 314–319, Feb. 2013.

[120] S. Ouhenia, "Structure of beta - ti o2," *Private Communication*, vol. 1, pp. 1–1, 2006.

[121] M. Rezaee, "The role of brookite in mechanical activation of anatase-to-rutile transformation of nanocrystalline tio2: An xrd and raman spectroscopy investigation," *CrystEngComm*, vol. 13, pp. 5055–, 2011.

[122] T. Weirich, "Rietveld analysis of electron powder diffraction data from nanocrystalline anatase, ti o2," *Ultramicroscopy*, vol. 81, pp. 263–270, 2000.

[123] S. Rühl, "The Inorganic Crystal Structure Database (ICSD): A Tool for Materials Sciences," in *Materials Informatics*, John Wiley & Sons, Ltd, 2019, pp. 41–54, ISBN: 978-3-527-80226-5.

[124] M. Horn, "Refinement of the structure of anatase at several temperatures sample: T = 25 c locality: Legenbach quarry, binnatal, switzerland," *Zeitschrift fur Kristallographie*, vol. 136, pp. 273–281, 1972.

[125] C. J. Howard, "Structural and thermal parameters for rutile and anatase," *Acta Crystallographica, Section B*, vol. 47, pp. 462–468, 1991.

[126] R. W. G. Wyckoff, "Second edition. interscience publishers, new york, new york," *Crystal Structures*, vol. 1, pp. 239–444, 1963.

[127] F. Schossberger, "Ueber die umwandlung des titandioxyds," *Zeitschrift fuer Kristallographie, Kristallgeometrie, Kristallphysik, Kristallchemie (-144,1977)*, vol. 104, pp. 358–374, 1942.

[128] R. L. Parker, "Zur kristallstruktur von anastas und rutil. (ii. teil. die anastasstruktur).," *Zeitschrift fuer Kristallographie, Kristallgeometrie, Kristallphysik, Kristallchemie (-144,1977)*, vol. 59, pp. 1–54, 1924.

[129] G. Bergerhoff, R. Hundt, R. Sievers, and I. Brown, "The inorganic crystal structure data base," *Journal of Chemical Information and Computer Sciences*, vol. 23, no. 2, pp. 66–69, 1983.

[130] V. Khitrova, "An electron-diffraction investigation of titanium dioxide in thin films," *Kristallografiya*, vol. 22, pp. 1253–1258, 1977.

[131] L. Pauling and J. Sturdivant, "The crystal structure of brookite," *Zeitschrift fuer Kristallographie, Kristallgeometrie, Kristallphysik, Kristallchemie (-144,1977)*, vol. 68, pp. 239–256, 1928.

[132] E. P. Meagher, "Polyhedral thermal expansion in the tio2 polymorphs: Refinement of the crystal structures of rutile and brookite at high temperature sample at 25 degrees c," *The Canadian Mineralogist*, vol. 17, pp. 77–85, 1979.

[133] M. Okrusch, "Intergrown niobian rutile phases with sc- and w-rich ferrocolumbite: An electron-microprobe and rietveld study," *American Mineralogist*, vol. 88, pp. 986–995, 2003.

[134] C. Igathinathane, L. O. Pordesimo, E. P. Columbus, W. D. Batchelor, and S. R. Methuku, "Shape identification and particles size distribution from basic shape parameters using ImageJ," *Computers and Electronics in Agriculture*, vol. 63, no. 2, pp. 168–182, Oct. 2008.

[135] M. W. Terban, C. Shi, R. Silbernagel, A. Clearfield, and S. J. L. Billinge, "Local Environment of Terbium(III) Ions in Layered Nanocrystalline Zirconium(IV) Phosphonate-Phosphate Ion Exchange Materials," *Inorganic Chemistry*, vol. 56, no. 15, pp. 8837–8846, Aug. 2017.

[136] S. Banerjee *et al.*, "Cluster-mining: An approach for determining core structures of metallic nanoparticles from atomic pair distribution function data," *Acta Crystallographica Section A: Foundations and Advances*, vol. 76, no. 1, pp. 24–31, Jan. 2020.

[137] K. Tomita, V. Petrykin, M. Kobayashi, M. Shiro, M. Yoshimura, and M. Kakihana, "A Water-Soluble Titanium Complex for the Selective Synthesis of Nanocrystalline Brookite, Rutile, and Anatase by a Hydrothermal Method," *Angewandte Chemie International Edition*, vol. 45, no. 15, pp. 2378–2381, 2006.

[138] B. M. McMurtry, K. Qian, J. K. Teglasi, A. K. Swarnakar, J. De Roo, and J. S. Owen, "Continuous Nucleation and Size Dependent Growth Kinetics of Indium Phosphide Nanocrystals," *Chemistry of Materials*, vol. 32, no. 10, pp. 4358–4368, May 2020.

[139] T. Tong *et al.*, "Effects of Material Morphology on the Phototoxicity of Nano-TiO2 to Bacteria," *Environmental Science & Technology*, vol. 47, no. 21, pp. 12 486–12 495, Nov. 2013.

[140] Z.-S. Wang, H. Kawauchi, T. Kashima, and H. Arakawa, "Significant influence of TiO2 photoelectrode morphology on the energy conversion efficiency of N719 dye-sensitized solar cell," *Coordination Chemistry Reviews*, Michael Graetzel Festschrift, a tribute for his 60th Birthday, Dye Sensitized Solar Cells, vol. 248, no. 13, pp. 1381–1389, Jul. 2004.

[141] X. Jiang and T. Wang, "Influence of Preparation Method on Morphology and Photocatalysis Activity of Nanostructured TiO2," *Environmental Science & Technology*, vol. 41, no. 12, pp. 4441–4446, Jun. 2007.

[142] C. Foo *et al.*, "Characterisation of oxygen defects and nitrogen impurities in TiO2 photocatalysts using variable-temperature X-ray powder diffraction," *Nature Communications*, vol. 12, no. 1, p. 661, Jan. 2021.

[143] Y. Zhang, Z. Ding, C. W. Foster, C. E. Banks, X. Qiu, and X. Ji, "Oxygen Vacancies Evoked Blue TiO2(B) Nanobelts with Efficiency Enhancement in Sodium Storage Behaviors," *Advanced Functional Materials*, vol. 27, no. 27, p. 1 700 856, 2017.

[144] G. Guisbiers, "Schottky Defects in Nanoparticles," *The Journal of Physical Chemistry C*, vol. 115, no. 6, pp. 2616–2621, Feb. 2011.

[145] M. Müller and K. Albe, "Concentration of thermal vacancies in metallic nanoparticles," *Acta Materialia*, vol. 55, no. 9, pp. 3237–3244, May 2007.

[146] B. Choudhury, P. Chetri, and A. Choudhury, "Annealing temperature and oxygen-vacancy-dependent variation of lattice strain, band gap and luminescence properties of CeO2 nanoparticles," *Journal of Experimental Nanoscience*, vol. 10, no. 2, pp. 103–114, Jan. 2015.

[147] L. Soriano *et al.*, "Thermal annealing of defects in highly defective NiO nanoparticles studied by X-ray and electron spectroscopies," *Chemical Physics Letters*, vol. 266, no. 1, pp. 184–188, Feb. 1997.

[148] A. Contreras-Ramirez, S. Tao, G. S. Day, V. I. Bakhmutov, S. J. L. Billinge, and H.-C. Zhou, "Zirconium Phosphate: The Pathway from Turbostratic Disorder to Crystallinity," *Inorg. Chem.*, p. 15, 2019.

[149] D. Avdibegović, W. Zhang, J. Xu, M. Regadío, R. Koivula, and K. Binnemans, "Selective ion-exchange separation of scandium(III) over iron(III) by crystalline α-zirconium phosphate platelets under acidic conditions," *Separation and Purification Technology*, vol. 215, pp. 81–90, May 2019.

[150] D. Golubenko, Y. Karavanova, S. Melnikov, A. Achoh, G. Pourcelly, and A. Yaroslavtsev, "An approach to increase the permselectivity and mono-valent ion selectivity of cation-exchange membranes by introduction of amorphous zirconium phosphate nanoparticles," *Journal of Membrane Science*, vol. 563, pp. 777–784, Oct. 2018.

[151] C. Zhu, X. Dong, Z. Chen, and R. Naidu, "Adsorption of aqueous Pb(II), Cu(II), Zn(II) ions by amorphous tin(VI) hydrogen phosphate: An excellent inorganic adsorbent," *International Journal of Environmental Science and Technology*, vol. 13, no. 5, pp. 1257–1268, May 2016.

[152] K. A. Kraus and H. O. Phillips, "ADSORPTION ON INORGANIC MATERIALS. I. CATION EXCHANGE PROPERTIES OF ZIRCONIUM PHOSPHATE," *Journal of the American Chemical Society*, vol. 78, no. 3, pp. 694–694, Feb. 1956.

[153] C. Amphlett, L. McDonald, and M. Redman, "Synthetic inorganic ion-exchange materials—I zirconium phosphate," *Journal of Inorganic and Nuclear Chemistry*, vol. 6, no. 3, pp. 220–235, Jun. 1958.

[154] G. Alberti, U. Costantino, S. Allulli, and N. Tomassini, "Crystalline Zr(R-PO3)2 and Zr(R-OPO3)2 compounds (R = organic radical)," *Journal of Inorganic and Nuclear Chemistry*, vol. 40, no. 6, pp. 1113–1117, Jan. 1978.

[155] Y. Cheng, H. Zhang, J. A. Jaenicke, E. C. P. Tan, and G.-K. Chuah, "Minimalistic Synthesis of α-Zirconium Diammonium Phosphate and Zirconia for Applications in Ion Exchange and Catalysis," *ACS Sustainable Chemistry & Engineering*, vol. 7, no. 1, pp. 895–904, Jan. 2019.

[156] M. Pica, A. Donnadio, R. D'Amato, D. Capitani, M. Taddei, and M. Casciola, "Layered Metal(IV) Phosphonates with Rigid Pendant Groups: New Synthetic Approaches to Nanosized Zirconium Phosphate Phenylphosphonates," *Inorganic Chemistry*, vol. 53, no. 4, pp. 2222–2229, Feb. 2014.

[157] M. Pica, A. Donnadio, D. Capitani, R. Vivani, E. Troni, and M. Casciola, "Advances in the Chemistry of Nanosized Zirconium Phosphates: A New Mild and Quick Route to the Synthesis of Nanocrystals," *Inorganic Chemistry*, vol. 50, no. 22, pp. 11 623–11 630, Nov. 2011.

[158] H.-J. Sue, K. T. Gam, N. Bestaoui, N. Spurr, and A. Clearfield, "Epoxy Nanocomposites Based on the Synthetic α-Zirconium Phosphate Layer Structure," *Chemistry of Materials*, vol. 16, no. 2, pp. 242–249, Jan. 2004.

[159] T. Takei, Q. Dong, Y. Yonesaki, N. Kumada, and N. Kinomura, "Preparation of Hybrid Film of Polyaniline and Organically Pillared Zirconium Phosphate Nanosheet by Electrodeposition," *Langmuir*, vol. 27, no. 1, pp. 126–131, Jan. 2011.

[160] L. Sun, W. J. Boo, R. L. Browning, H.-J. Sue, and A. Clearfield, "Effect of Crystallinity on the Intercalation of Monoamine in α-Zirconium Phosphate Layer Structure," *Chemistry of Materials*, vol. 17, no. 23, pp. 5606–5609, Nov. 2005.

[161] H. Hu, J. C. Martin, M. Xiao, C. S. Southworth, Y. Meng, and L. Sun, "Immobilization of Ionic Liquids in Layered Compounds via Mechanochemical Intercalation," *The Journal of Physical Chemistry C*, vol. 115, no. 13, pp. 5509–5514, Apr. 2011.

[162] M. Pica, A. Donnadio, E. Troni, D. Capitani, and M. Casciola, "Looking for New Hybrid Polymer Fillers: Synthesis of Nanosized α-Type Zr(IV) Organophosphonates through an Unconventional Topotactic Anion Exchange Reaction," *Inorganic Chemistry*, vol. 52, no. 13, pp. 7680–7687, Jul. 2013.

[163] E. Boccalon, M. Nocchetti, M. Pica, A. Romani, and M. Casciola, "Layered double hydroxide and zirconium phosphate as ion exchangers for the removal of 'black crusts' from the surface of ancient monuments," *Dalton Transactions*, vol. 47, no. 9, pp. 2976–2985, 2018.

[164] Y. Zhou *et al.*, "Solid Acid Catalyst Based on Single-Layer α-Zirconium Phosphate Nanosheets for Biodiesel Production via Esterification," *Catalysts*, vol. 8, no. 1, p. 17, Jan. 2018.

[165] Y. Zhou *et al.*, "Sulfonic Acid-Functionalized α-Zirconium Phosphate Single-Layer Nanosheets as a Strong Solid Acid for Heterogeneous Catalysis Applications," *ACS Applied Materials & Interfaces*, vol. 6, no. 10, pp. 7417–7425, May 2014.

[166] L. Xu, C. Lei, R. Xu, X. Zhang, and J. Xu, "Intumescent flame retardant of polypropylene system with enhanced thermal properties and flame retardancy based on α-zirconium phosphate composite particles," *Polymer Bulletin*, vol. 75, no. 6, pp. 2707–2727, Jun. 2018.

[167] M. Casciola, D. Capitani, A. Donnadio, G. Munari, and M. Pica, "Organically Modified Zirconium Phosphate by Reaction with 1,2-Epoxydodecane as Host Material for Polymer Intercalation: Synthesis and Physicochemical Characterization," *Inorganic Chemistry*, vol. 49, no. 7, pp. 3329–3336, Apr. 2010.

[168] B. M. Mosby, A. Díaz, V. Bakhmutov, and A. Clearfield, "Surface Functionalization of Zirconium Phosphate Nanoplatelets for the Design of Polymer Fillers," *ACS Applied Materials & Interfaces*, vol. 6, no. 1, pp. 585–592, Jan. 2014.

[169] J. González-Villegas *et al.*, "Poly(ethylene glycol)-modified zirconium phosphate nanoplatelets for improved doxorubicin delivery," *Inorganica Chimica Acta*, vol. 468, pp. 270–279, Nov. 2017.

[170] J. D. Burns, A. Clearfield, M. Borkowski, and D. T. Reed, "Pillared metal(IV) phosphate-phosphonate extraction of actinides," *Radiochimica Acta*, vol. 100, no. 6, pp. 381–387, Jun. 2012.

[171] M. Zamin, T. Shaheen, and A. Dyer, "Use of amorphous zirconium phosphate for the treatment of radioactive waste: III. Column experiments for Cs and Sr removal," *Journal of Radioanalytical and Nuclear Chemistry Articles*, vol. 182, no. 2, pp. 345–348, Aug. 1994.

[172] Y. Zhang, X. Zeng, X. Lai, and H. Li, "Preparation of functionalized zirconium phosphate and its effect on the flame retardancy of silicone rubber," *RSC Advances*, vol. 8, no. 1, pp. 111–121, 2018.

[173] Y. Chen, X. Wang, A. Clearfield, and H. Liang, "Anti-Galling Effects of α-Zirconium Phosphate Nanoparticles as Grease Additives," *Journal of Tribology*, vol. 141, no. 3, p. 031 801, Mar. 2019.

[174] X. Zhang, H. Xu, and J. Dong, "Synthesis and Tribological Performance of Different Particle-Sized Nickel-Ion-Exchanged α-Zirconium Phosphates," *Journal of Materials Engineering and Performance*, vol. 27, no. 4, pp. 1927–1935, Apr. 2018.

[175] Y. Aoki *et al.*, "Thickness-Induced Proton-Conductivity Transition in Amorphous Zirconium Phosphate Thin Films," *Chemistry of Materials*, vol. 22, no. 19, pp. 5528–5536, Oct. 2010.

[176] A. Donnadio *et al.*, "A Layered Mixed Zirconium Phosphate/Phosphonate with Exposed Carboxylic and Phosphonic Groups: X-ray Powder Structure and Proton Conductivity Properties," *Inorganic Chemistry*, vol. 53, no. 24, pp. 13 220–13 226, Dec. 2014.

[177] D. Truffier-Boutry, A. De Geyer, L. Guetaz, O. Diat, and G. Gebel, "Structural Study of Zirconium Phosphate-Nafion Hybrid Membranes for High-Temperature Proton Exchange Membrane Fuel Cell Applications," *Macromolecules*, vol. 40, no. 23, pp. 8259–8264, Nov. 2007.

[178] H. Xiao and S. Liu, "Zirconium phosphate (ZrP)-based functional materials: Synthesis, properties and applications," *Materials & Design*, vol. 155, pp. 19–35, Oct. 2018.

[179] M. Pica, A. Donnadio, and M. Casciola, "From microcrystalline to nanosized α-zirconium phosphate: Synthetic approaches and applications of an old material with a bright future," *Coordination Chemistry Reviews*, vol. 374, pp. 218–235, Nov. 2018.

[180] G. Ashiotis *et al.*, "The fast azimuthal integration Python library: pyFAI," *Journal of Applied Crystallography*, vol. 48, no. 2, pp. 510–519, Apr. 2015.

[181] J. M. Troup and A. Clearfield, "Mechanism of ion exchange in zirconium phosphates. 20. Refinement of the crystal structure of .alpha.-zirconium phosphate," *Inorganic Chemistry*, vol. 16, no. 12, pp. 3311–3314, Dec. 1977.

[182] M. Liu *et al.*, "Designing Glass and Crystalline Phases of Metal-Bis(acetamide) Networks to Promote High Optical Contrast," *Journal of the American Chemical Society*, Nov. 2022.

[183] O. M. Yaghi, M. O'Keeffe, N. W. Ockwig, H. K. Chae, M. Eddaoudi, and J. Kim, "Reticular synthesis and the design of new materials," *n*, vol. 423, pp. 705–714, 2003.

[184] S. Kitagawa, R. Kitaura, and S.-i. Noro, "Functional Porous Coordination Polymers," *Angewandte Chemie International Edition*, vol. 43, no. 18, pp. 2334–2375, Apr. 2004.

[185] O. M. Yaghi, "Reticular Chemistry: Molecular Precision in Infinite 2D and 3D," *Molecular Frontiers Journal*, vol. 03, no. 01, pp. 66–83, Jun. 2019.

[186] "Real space manifestation of the first sharp diffraction peak in the structure factor of liquid and glassy materials," *Proceedings of the Royal Society of London. Series A: Mathematical and Physical Sciences*, vol. 445, no. 1924, pp. 351–365, May 1994.

[187] V. V. T. Doan-Nguyen *et al.*, "Bulk Metallic Glass-like Scattering Signal in Small Metallic Nanoparticles," *ACS Nano*, vol. 8, no. 6, pp. 6163–6170, Jun. 2014.

[188] T. D. Bennett *et al.*, "Melt-Quenched Glasses of Metal-Organic Frameworks," *Journal of the American Chemical Society*, vol. 138, no. 10, pp. 3484–3492, Mar. 2016.

[189] S.-H. Lo *et al.*, "Rapid desolvation-triggered domino lattice rearrangement in a metal-organic framework," *Nature Chemistry*, vol. 12, no. 1, pp. 90–97, Jan. 2020.

[190] C. M. Dobson, “Protein folding and misfolding,” *Nature*, vol. 426, no. 6968, pp. 884–890, 2003.

[191] A. R. Fersht and V. Daggett, “Protein folding and unfolding at atomic resolution,” *Cell*, vol. 108, no. 4, pp. 573–582, 2002.

[192] M. Auton and D. W. Bolen, “Predicting the energetics of osmolyte-induced protein folding/unfolding,” *Proceedings of the National Academy of Sciences*, vol. 102, no. 42, pp. 15 065–15 068, 2005.

[193] D. Allan, *Trackpy*, Jan. 2022.

[194] A Arkilic, D. B. Allan, D Chabot, L. R. Dalesio, and W. K. Lewis, “Databroker: An Interface for NSLS-II Data Management System,” *Data Management*, p. 3, 2015.